UNDERSTANDING AN EVOLVING DIFFUSE PLATE BOUNDARY WITH GEODESY AND GEOCHRONOLOGY

A Dissertation
Presented to
The Academic Faculty

by

Zachery Meyer Lifton

In Partial Fulfillment
of the Requirements for the Degree
Doctor of Philosophy in the
School of Earth and Atmospheric Sciences

Georgia Institute of Technology
December 2013

UNDERSTANDING AN EVOLVING DIFFUSE PLATE BOUNDARY WITH GEODESY AND GEOCHRONOLOGY

Approved by:

Dr. Andrew V. Newman, Advisor
School of Earth and Atmospheric Sciences
Georgia Institute of Technology

Dr. Jeffrey Lee
Department of Geological Sciences
Central Washington University

Dr. Zhigang Peng
School of Earth and Atmospheric Sciences
Georgia Institute of Technology

Dr. Timothy H. Dixon
Department of Geology
University of South Florida

Dr. Josef Dufek
School of Earth and Atmospheric Sciences
Georgia Institute of Technology

Date Approved: Sept. 16, 2013

ACKNOWLEDGEMENTS

I received help and encouragement from many people during the course of this work. I would like to thank Kurt Frankel for believing in me and being an outstanding role model. He set a high standard and I sincerely hope he would have been proud of this work. Andrew Newman graciously stepped up to the role of advisor, and I thank him for his support and guidance, which I sometimes resisted. I thank Jeff Lee for not only opening many doors for me, but also for generously offering his expert advice on the Walker Lane and geology in general. He, Wendy Bohrson, and the rest of the Department of Geological Sciences at Central Washington University provided a warm and welcoming second home for me. I thank Timothy Dixon for providing his insight and expertise as both a co-author and committee member. I also thank Zhigang Peng and Josef Dufek for generously giving their time to serve on my comprehensive exam and dissertation defense committees.

I thank Chris Johnson for being a very capable field assistant during three field seasons in the Walker Lane. He helped survey GPS monuments, dig soil pits, chisel boulders, and manage field logistics, for which I'm very grateful. I also thank Andy Foy for his assistance with GPS surveying. I thank Tina Marstellar for teaching me how to prepare TCN samples, and Susan Zimmerman for assistance with AMS sample analysis. I thank Matthew Heizler and Jeff Lee for sharing their $^{40}Ar/^{39}Ar$ data with me, and Craig de Polo for providing copies of the low sun angle aerial photographs along the White Mountains fault zone. I thank Bill Hammond and Geoff Blewitt for loan of MAGNET monument adapters, and for permission to occupy their regional network. The staff of the White Mountains Research Station, including Denise Waterbury, John Smiley, Elizabeth

Sally, Lisa Bedient, and Shadow Ayala, provided outstanding logistical support for my fieldwork. My classmates at Georgia Tech taught me a great deal. I thank Lujia Feng for teaching me how to process GPS data, Jaime Convers for teaching me shell scripting and GMT, and Peng Zhao and Mary Benage for helping me grasp Matlab.

Most importantly, I thank my family and friends for their unwavering love and support. They give meaning to all this work. My parents, Susan and Alan, have loved me unconditionally and supported me in everything I've attempted, which has made the pursuit of my passions not only possible, but also enjoyable. My brother, Josh, has always blazed the trail for what is possible in life and I thank him for his guidance. My nephew, Moses, was born as I sat in my advisor's office taking my comprehensive exam; his very existence gave me a different perspective and helped me see a bigger picture. I thank numerous friends, who have been by my side or a phone call away, for keeping me sane. In particular, I owe a lot to Benny, Dorje, Sean, James, Howard, Darius, I-shan, Seaver, Zoe, and Rachel.

This study was funded by National Science Foundation grants EAR-0207365 awarded to J. Lee and EAR-0948570 awarded to K. Frankel, a University of California White Mountains Research Station minigrant, a GSA research grant, a Sigma Xi grant-in-aid of research, and an NCALM seed grant. This material is based in part on equipment provided by UNAVCO with support from NSF and NASA under NSF EAR-0735156, and on data provided by the EarthScope Plate Boundary Observatory supported by NSF EAR-0350028 and EAR-0732947.

The material in chapters 2, 3, and 4 was published, or is being prepared for publication, in the following peer-reviewed articles.

Chapter 2:

Lifton, Z.M., A.V. Newman, K.L. Frankel, C.W. Johnson, and T.H. Dixon, 2013, Insights into distributed plate rates across the Walker Lane from GPS geodesy, Geophysical Research Letters, 40(17), 4620-4624, doi:10.1002/grl.50804.

Chapter 3:

Lifton, Z.M., Lee, J., Frankel, K.L., Newman, A.V., Schroeder, J.M., Heizler, M.T., *in preparation*, Quaternary slip rates on the White Mountains Fault Zone, Eastern California: Implications for comparing geologic to geodetic slip rates across the Walker Lane: Geological Society of America Bulletin.

Chapter 4:

Lifton, Z.M., Newman, A.V., Frankel, K.L., *in preparation*, Latest Pleistocene and Holocene slip rates on the Lone Mountain fault: evidence for accelerating extension in the Silver Peak-Lone Mountain extensional complex: Lithosphere.

TABLE OF CONTENTS

LIST OF TABLES

LIST OF FIGURES

SUMMARY

Understanding spatial and temporal variations in strain accumulation and release along plate boundaries is a fundamental problem in tectonics. Short-term and long-term slip rates are expected to be equal if the regional stress field remains unchanged over time, yet discrepancies between modern geodetic (decadal time scale) slip rates and long-term geologic (10^3-10^6 years) slip rates have been observed on parts of the Pacific-North American plate boundary system. Contemporary geodetic slip rates are observed to be ~2 times greater than late Pleistocene geologic slip rates across the southern Walker Lane. I use a combination of GPS geodesy, detailed field geologic mapping, high-resolution LiDAR geodetic imaging, and terrestrial cosmogenic nuclide geochronology to investigate the observed discrepancy between long- and short-term slip rates. I find that the present day slip rate derived from GPS geodesy across the Walker Lane at ~37.5°N is 10.6 ± 0.5 mm/yr. GPS data suggest that much of the observed discrepancy occurs west of the White Mountains fault zone. New dextral slip rates on the White Mountains fault zone of 1.1 ± 0.1 mm/yr since 755 ka, 1.9 +0.5/-0.4 mm/yr since 75-115 ka, 1.9 +0.5/-0.4 mm/yr since 38.4 ± 9.0 ka, and 1.8 +2.8/-0.7 mm/yr since 6.2 ± 3.8 ka are significantly faster than previous estimates and suggest that slip rates there have remained constant since the middle Pleistocene. On the Lone Mountain fault I calculate slip rates of 0.8 ± 0.1 mm/yr since 14.6 ± 1.0 ka and 0.7 ± 0.1 mm/yr since 8.0 ± 0.5 ka, which suggest that extension in the Silver Peak-Lone Mountain extensional complex has increased dramatically since the late Pleistocene.

CHAPTER 1

INTRODUCTION

Understanding spatial and temporal variations in strain accumulation and release along plate boundaries is a fundamental problem in tectonics. Short-term and long-term slip rates are expected to be equal if the regional stress field remains unchanged over time, yet discrepancies between modern geodetic (decadal time scale) slip rates and long-term geologic (10^3-10^6 ka) slip rates have been observed on several major fault systems, including parts of the Pacific-North America plate boundary system (e.g. Bennett et al., 2003; Dolan et al., 2007; Frankel et al., 2007a, 2011; Oskin et al., 2008). Slip rate discrepancies have important implications for the evolution of faults and plate boundaries. Discrepancies may imply that strain is transient and varies in time. For example, clarifying long- and short-term slip rates may lead to a better understanding of characteristic vs. clustered earthquake rupture behavior (e.g. Gold and Cowgill, 2011; Wallace, 1987; Schwartz and Coppersmith, 1984). Or, discrepancies may imply that strain is distributed non-uniformly within a region of uniform far field stress (e.g. Thatcher, 2009). However, it is not clear whether observed discrepancies are real or simply a manifestation of insufficient data. While some discrepancies have been resolved by careful reanalysis of data (e.g. Cowgill et al., 2009), the slip rate discrepancy in the southern Walker Lane at ~37.5°N remains unresolved (e.g. Kirby et al., 2006; Frankel et al., 2007; Nagorsen-Rinke et al., 2013).

The Pacific-North American plate boundary is expressed in the western U.S. as a broad region of deformation that accommodates ~51 mm/yr of right-lateral motion between the two plates (DeMets et al., 2010). While ~35 mm/yr of motion is accommodated in a discrete region along the San Andreas fault zone, the remaining right-lateral motion occurs further east where it is distributed broadly across a complex array of faults in the Walker Lane and Basin and Range. The Walker Lane, which lies east of the Sierra Nevada on the western edge of the Basin and Range province, is a ~100-200-km-wide right-lateral shear zone composed of north-northwest striking dextral faults connected by northeast striking normal fault step overs.

In this dissertation I use a variety of techniques to examine slip rates in the southern Walker Lane over multiple time scales, spanning the middle Pleistocene, late Pleistocene, Holocene, and present. The goal of this research is to understand the causes and implications of the observed discrepancy between long- and short-term slip rates in the southern Walker Lane. Chapter 2 focuses on the collection, processing, and modeling of GPS data. Chapter 3 focuses on the tectonic geomorphology of the White Mountains fault zone, in particular it focuses on new fault slip rates based on geomorphologic mapping, LiDAR data, $^{40}Ar/^{39}Ar$ ages, and cosmogenic nuclide exposure ages. Chapter 4 focuses on new extension rates on the Lone Mountain fault based on geologic mapping, fault scarp surveying, and cosmogenic nuclide exposure ages. Chapter 5 summarizes and synthesizes the research I have done. Finally, Chapter 6 outlines the direction of future work that I propose.

CHAPTER 2

INSIGHTS INTO DISTRIBUTED PLATE RATES ACROSS THE WALKER LANE FROM GPS GEODESY

2.1 ABSTRACT

Contemporary geodetic slip rates are observed to be ~2 times greater than late Pleistocene geologic slip rates across the southern Walker Lane. Using a dense GPS network we compare the present-day crustal velocities to observed geologic slip rates in the region. We find that the Walker Lane is characterized by a smooth transition from westward extension in the Basin and Range to northwestward motion of the Sierra Nevada block. The GPS velocity field indicates that: 1) plate parallel (N37°W) velocities define a velocity differential of 10.6 ± 0.5 mm/yr between the western Basin and Range and the Sierra Nevada block, 2) there is ~2 mm/yr of contemporary extension perpendicular to the normal faults of the Silver Peak-Lone Mountain extensional complex, and 3) most of the observed discrepancy in long- and short-term slip rates occurs across Owens Valley. We believe the discrepancy is due to distributed strain and underestimated geologic slip rates.

2.2 INTRODUCTION

The southern Walker Lane is a diffuse right-lateral shear zone comprising strike-slip faults and extensional step-overs that extends from the Garlock Fault north to the Mina Deflection, and is thought to accommodate ~20% of the relative motion between

the North American and Pacific plates (Dokka and Travis, 1990; Bennett et al., 2003; Wesnousky, 2005a; Hammond and Thatcher, 2007). However, within parts of the southern Walker Lane the contemporary geodetic deformation rate is ~2 times higher than the geologic fault slip rate over the late Pleistocene. We use GPS data from a dense network of sites to determine specifically where the observed discrepancy occurs between geologic and geodetic slip rates. In particular, we are testing the hypotheses that 1) some of the "missing" slip is taken up in the Silver Peak-Lone Mountain extensional complex (SPLM) and 2) much of the discrepancy between geodetic and geologic slip rates occurs in Owens Valley, particularly on the White Mountain Fault (WMF).

The two main structures in the southern Walker Lane are the Northern Death Valley-Fish Lake Valley Fault (DV-FLVF) and the WMF (Figure 2.1a), which accommodate 2.5-3.5 and 0.3-0.4 mm/yr of slip, respectively, over geologic time scales. (Frankel et al., 2011; Kirby et al., 2006). Shear zone-parallel extension on normal faults within the SPLM accommodate 0.3-2.0 mm/yr (Reheis and Sawyer, 1997; Hoeft and Frankel, 2010; Foy et al., 2012). Some dextral shear may also be accommodated on normal faults west of the WMF, such as the Fish Slough Fault, the normal faults of the Volcanic Tableland, and the Round Valley Fault. However, these are almost all normal faults accommodating extension perpendicular to the strike of the shear zone (Sheehan, 2007). The Round Valley Fault shows evidence of right-lateral slip, but there is currently no age constraint on the offset landform (Phillips and Majkowski, 2011). Thus, the total late Pleistocene right-lateral slip rate summed across the southern Walker Lane at ~37.5°N is ~3.0-5.9 mm/yr, while the geodetic rate measured with GPS across the same region was observed to be ~9-10 mm/yr (Dixon et al., 2000; Bennett et al., 2003).

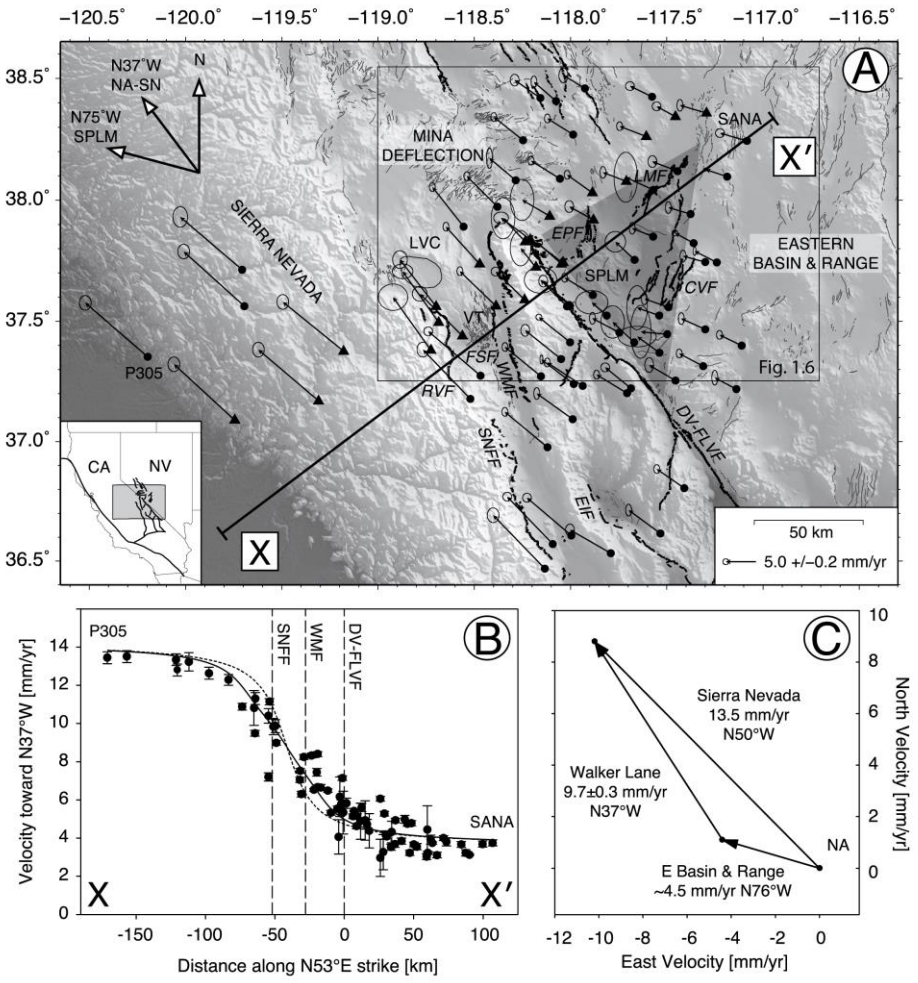

Figure 2.1. A) GPS velocity field across the southern Walker Lane. All velocities are relative to stable North America (ITRF-NA2005; [*DeMets et al.*, 2010]). Error ellipses represent 2σ uncertainties. Solid grey lines are Quaternary or younger faults. Triangles are sites used in Fig. 2. Local plate motion is N37°W; direction of fault-perpendicular extension in the Silver Peak-Lone Mountain extensional complex is N75°W. CVF – Clayton Valley Fault; DV-FLVF – Death Valley-Fish Lake Valley Fault; EIF – Eastern Inyo Fault; EPF – Emigrant Peak Fault; FSF – Fish Slough Fault; LMF – Lone Mountain Fault; LVC – Long Valley Caldera; RVF – Round Valley Fault; SNFF – Sierra Nevada Frontal Fault; SPLM – Silver Peak-Lone Mountain extensional complex (grey shaded region); VT – Volcanic Tableland; WMF – White Mountains Fault. B) Profile of plate-parallel (toward N37°W) GPS velocities for all sites projected onto a plate-normal transect across the southern Walker Lane. Positions of major faults crossed by the transect are shown with dashed lines. Solid curve is the preferred dislocation model for the three faults shown [locking depth = 15 km, far field velocity = 10.6 ± 0.5 mm/yr]. Dashed curve is the dislocation model for a single fault with the same far field velocity and locking depth. Error bars represent 2σ uncertainties. C) Velocity vector diagram for Walker Lane. Sierra Nevada block velocity was estimated by averaging the velocity relative to North America of six PBO continuous sites in the Sierra Nevada. The azimuth of Walker Lane motion is assumed to be parallel to local plate motion of N37°W; magnitude of Walker Lane motion is the difference between the furthest northeastern and furthest southwestern GPS sites along the plate normal transect [1b].

Previous studies have estimated the geodetic deformation rate across the evolving, diffuse Pacific-North American plate boundary east of the San Andreas Fault system. Hearn and Humphreys (1998) modeled VLBI and sparse GPS data to estimate a velocity differential of 10.8 ± 1.5+ mm/yr (no uncertainty reported; we estimated uncertainty from original data) across the southern Walker Lane between the Owens Valley Radio Observatory and the Garlock Fault. Gan et al. (2000) used a transect of GPS stations at approximately 36.5°N to estimate a velocity differential across the Walker Lane of 10.3 ± 4 mm/yr (our estimate of uncertainty from original data). In estimating the rigidity and motion of the Sierra Nevada block, Dixon et al. (2000) used several campaign sites at ~37.5°N, which we have subsequently resurveyed, to estimate a velocity differential across the Walker Lane of 11 ± 1 mm/yr. Bennett et al. (2003) combined the GPS data of Gan et al. (2000) and Dixon et al. (2000) with GPS data from numerous sites in central and northern Nevada to estimate a Walker Lane velocity of 9.3 ± 0.2 mm/yr. McCaffrey (2005) estimated 11.3 ± 0.3 mm/yr of relative motion across the eastern California shear zone at 36°N. Hammond and Thatcher (2007) used campaign GPS data along a transect at ~38.5°N to estimate ~10 mm/yr (no uncertainty reported) of deformation across the Walker Lane. Further north, at ~39°N, Wesnousky et al. (2012) estimate right lateral shear of 5-6 mm/yr along a 120-km-long transect across the Walker Lane.

2.3 DATA

We surveyed 48 campaign monuments across the southern Walker Lane in 2010, 2011, and 2012 using Trimble R7 receivers and precision fixed-height spike-mounts (0.500 m) (Table 2.1). Campaign monuments included 26 Mobile Array of GPS for

Nevada Transtension (MAGNET) monuments, 12 existing monuments that were surveyed as early as 1994, and 10 new monuments installed for this study. Resurveying existing campaign monuments extends station time series, which improves velocity estimates. Monuments were observed for a minimum of 72 hours in each campaign. We combined these new campaign data with newly processed data from 28 Plate Boundary Observatory (PBO) continuous GPS stations to create a dense GPS network of 76 sites with an average spacing of ~10 km (Figure 2.1a). GPS data were processed using GIPSY/OASIS II software with precise point positioning (Zumberge et al., 1997). All velocities are calculated in ITRF2005 relative to stable North America, with an Euler pole of -6.8°, -84.8° rotating 0.189° My^{-1} (NA-ITRF2005, DeMets et al., 2010). The location, velocity, and uncertainty for all GPS sites are presented in Table 2.1.

Table 2.1. GPS station positions and velocities.

Station ID	Longitude [° W]	Latitude [° N]	Elevation [m]	Velocity[a] East [mm/yr]	Velocity[a] North [mm/yr]	Uncertainty[b] East [mm/yr]	Uncertainty[b] North [mm/yr]	Years Occupied
CHIA	-118.2069696	37.83817050	1982.8452	-4.9	3.6	0.5	0.4	2005, 2007, 2009, 2011
CLDL	-117.8855495	38.03091445	1389.9126	-4.2	3.0	0.2	0.3	2002, 2010, 2011
COL2	-118.0539701	38.08877954	1468.2873	-4.8	3.0	0.2	0.3	2005, 2007, 2008, 2009, 2010, 2011
COLU	-117.2383991	37.74347047	1687.8772	-3.7	1.9	0.1	0.3	2002, 2010, 2011
DEEP	-118.0471973	37.34255335	1640.6484	-6.0	4.8	0.3	0.4	2005, 2007, 2009, 2011
DUNF	-117.3088504	37.31361674	1961.3906	-4.0	2.1	0.2	0.3	2005, 2007, 2009, 2011
DYER	-118.0393350	37.74280420	1511.9377	-4.5	3.4	0.1	0.1	1999 – 2010 inclusive
EPAS	-117.8807044	37.91966955	1817.0489	-4.0	2.2	0.3	0.4	2005, 2007, 2008, 2009, 2011
FISH	-118.0462849	37.73698880	1442.6225	-3.9	3.5	0.3	0.2	1998, 2001, 2010, 2011
FSH2	-118.0064933	37.56705062	1620.9603	-4.3	4.0	0.3	0.4	2005, 2007, 2009, 2011
FURN	-118.0173757	37.56177425	1698.2984	-4.4	4.4	1.1	0.9	2010, 2011, 2012
GABB	-117.4545416	38.34440095	1519.9937	-3.1	1.7	0.3	0.3	1998, 2001, 2003, 2011
GEMF	-117.2984995	37.74503285	1857.4646	-3.7	1.0	0.2	0.4	2005, 2007, 2009, 2011
GOLD	-117.3589724	37.82279605	1525.6699	-3.1	1.7	0.2	0.2	1998, 2001, 2010, 2011, 2012
HOLT	-117.9236800	38.45881028	1976.9901	-3.6	2.2	0.3	0.5	2006, 2007, 2008, 2009, 2010
ICOR	-117.2982893	37.46633251	1555.3395	-4.0	1.8	0.2	0.4	2005, 2007, 2009, 2011
LATE	-118.2830751	38.08197168	1738.9940	-4.4	3.7	0.2	0.7	2001, 2003, 2010, 2012
LEDY	-118.1803636	37.72282657	2038.0235	-2.5	3.2	0.7	1.2	2010, 2011, 2012
LIDA	-117.4962857	37.44630447	1936.8269	-4.4	0.4	0.7	1.8	2010, 2011, 2012
LIME	-117.9815300	37.23887429	1821.5378	-5.4	4.1	0.1	0.3	1998, 2001, 2003, 2010
LNMT	-117.5678855	38.04302221	1531.1835	-4.6	2.1	0.8	1.7	2010, 2011, 2012
LWSH	-117.5373659	37.52385460	2010.6035	-3.7	1.3	0.7	1.5	2010, 2011, 2012
MILR	-117.4418638	38.11989194	1487.1938	-4.2	1.6	0.3	0.4	2006, 2007, 2008, 2009, 2011
MINA	-118.0737541	38.40741196	1471.4340	-3.7	3.2	0.2	0.4	2001, 2003, 2011

MNA2	-118.1551354	38.41961546	1497.8931	-4.3	3.0	0.3	0.4	2005, 2007, 2008, 2009, 2010, 2011
MOHO	-118.2451385	38.24620487	1965.3126	-4.9	3.9	0.2	0.3	2005, 2007, 2008, 2009, 2010, 2011
MONT	-117.7084390	38.07777007	1639.2584	-3.9	1.5	0.2	0.4	2005, 2007, 2008, 2009, 2011
MUSB	-119.3093510	37.16994098	2042.5165	-10.0	8.5	0.4	0.5	2009, 2010, 2011, 2012
ORIE	-117.4526793	37.25308319	1388.8689	-4.4	2.6	0.3	0.5	2005, 2007, 2009, 2011
P091	-117.5315412	36.61432438	1966.8507	-5.3	3.9	0.2	0.4	2007, 2008, 2009, 2010, 2011
P092	-117.4068013	36.80419467	2156.8854	-4.6	3.2	0.2	0.3	2006, 2007, 2008, 2009, 2010, 2011
P093	-117.9941444	36.60602516	1339.0654	-7.4	6.3	0.3	0.3	2007, 2008, 2009, 2010, 2011
P094	-117.7041939	37.20083606	1729.2112	-5.1	3.1	0.2	0.3	2006, 2007, 2008, 2009, 2010, 2011
P245	-119.7061218	37.71311614	1579.8350	-10.3	8.8	0.5	0.7	2009, 2010, 2011, 2012
P305	-120.1967591	37.35221410	96.0578	-10.4	9.0	0.4	0.5	2009, 2010, 2011, 2012
P311	-118.5198015	37.17756286	3698.6404	-7.9	8.2	0.4	0.5	2009, 2010, 2011, 2012
P465	-118.1324330	36.46683388	2901.5420	-8.6	8.9	0.4	0.5	2007, 2008, 2009, 2010, 2011
P466	-117.7894608	36.53124937	2754.5877	-6.8	3.9	0.3	0.4	2007, 2008, 2009, 2010, 2011
P467	-118.0906227	36.57020200	1380.1173	-7.6	7.9	0.3	0.3	2006, 2007, 2008, 2009, 2010, 2011
P468	-118.1183626	36.97568225	2853.3103	-7.1	5.9	0.2	0.3	2006, 2007, 2008, 2009, 2010, 2011
P469	-117.9358096	37.23142509	1794.8141	-5.9	3.9	0.2	0.3	2007, 2008, 2009, 2010, 2011
P512	-119.6944472	37.56263504	1344.7116	-10.1	9.1	0.4	0.5	2009, 2010, 2011, 2012
P627	-118.3785244	37.97310119	2342.1401	-5.1	5.1	0.2	0.3	2006, 2007, 2008, 2009, 2010, 2011
P629	-119.1793726	37.37586648	2725.6622	-10.1	8.2	0.4	0.5	2009, 2010, 2011, 2012
P643	-118.6981621	37.56155280	2121.9835	-6.0	7.8	0.5	0.6	2009, 2010, 2011, 2012
P644	-118.6844028	37.49539211	3458.6137	-6.0	8.5	0.7	0.5	2009, 2010, 2011, 2012
P650	-118.5549002	37.89127658	2298.1762	-5.2	6.6	0.2	0.3	2006, 2007, 2008, 2009, 2010, 2011
P651	-118.3869824	37.56310953	1316.7145	-6.0	5.8	0.2	0.3	2006, 2007, 2008, 2009, 2010, 2011
P652	-118.2384513	37.58915803	3865.2454	-4.8	4.7	0.3	0.3	2007, 2008, 2009, 2010, 2011
P653	-118.4716598	37.73749979	1826.2904	-5.6	6.2	0.2	0.3	2006, 2007, 2008, 2009, 2010, 2011

P723	-118.7247766	37.38042606	3197.7895	-6.3	8.8	1.0	0.9	2009, 2010, 2011
P724	-118.5610691	37.43947702	1371.6190	-7.1	7.0	0.5	0.5	2009, 2010, 2011, 2012
P725	-119.7456063	37.08889501	330.9408	-10.1	9.3	0.4	0.5	2009, 2010, 2011, 2012
P727	-118.4667725	37.27357873	2677.2088	-8.7	7.4	0.3	0.3	2007, 2008, 2009, 2010, 2011
PETT	-118.2341137	37.82928917	2381.2168	-3.7	3.9	0.8	1.4	2010, 2011, 2012
PIGN	-117.6673424	37.41230419	1963.5022	-3.6	3.4	0.8	1.1	2010, 2011, 2012
PILO	-117.9851309	38.26966099	1706.3637	-4.3	2.7	0.2	0.3	2005 – 2011 inclusive
RHIL	-117.5745378	38.42463194	1799.0081	-3.7	1.8	0.3	0.3	2006, 2007, 2008, 2010, 2011
ROYS	-117.6065914	38.26264241	1613.7066	-4.4	1.7	0.2	0.3	2006, 2007, 2008, 2010, 2011
SANA	-117.0815710	38.24445310	1775.9236	-4.5	1.3	0.3	0.3	2006, 2007, 2008, 2010, 2011
SCTY	-117.1365330	37.21820323	1217.7813	-3.6	1.9	0.2	0.5	1998, 2001, 2010
SULF	-117.6842181	37.22117602	1655.1706	-4.3	3.5	0.3	0.3	2005, 2007, 2009, 2011
SYLV	-117.7444661	37.45252051	1887.3640	-4.5	2.4	0.2	0.4	2005, 2007, 2009, 2011
THOM	-117.3749797	37.94290443	1659.3359	-3.7	1.1	0.2	0.4	2005, 2007, 2009, 2011
TONI	-117.2926155	38.35817152	1823.0331	-4.4	1.3	0.2	0.4	2006, 2007, 2008, 2010, 2011
TONO	-117.1840393	38.09719462	2066.0149	-3.6	1.2	0.1	0.1	1999 – 2011 inclusive
TULC	-117.5367022	37.36918001	1848.2879	-3.7	2.7	1.3	0.7	2010, 2011, 2012
UFOS	-117.1090488	37.39880631	1409.2528	-3.7	1.8	0.2	0.3	2005, 2007, 2009, 2011
VBPK	-117.6659345	37.75447794	1649.1486	-3.2	3.0	0.7	0.7	2010, 2011, 2012
VLCH	-118.1071638	37.93474715	1643.9515	-4.6	2.7	0.8	1.4	2010, 2011, 2012
WAUC	-117.9872059	37.09243019	1996.8158	-6.0	4.3	0.2	0.4	1998, 2001, 2003, 2010
WEEP	-117.5689321	37.85003281	1409.9169	-3.5	1.4	0.2	0.4	2005, 2007, 2009, 2011
WOLF	-117.8828754	37.60827119	1915.7570	-4.7	2.9	0.2	0.3	2005, 2007, 2009, 2011
WSTG	-118.1520166	37.27072612	2200.4265	-6.0	4.9	0.2	0.3	1997, 1998, 2001, 2003, 2010
WYMN	-118.0011103	37.41245014	1757.3729	-5.2	4.2	0.2	0.2	1998, 2001, 2003, 2010
ZUMA	-117.4902193	37.55816612	1924.5106	-4.0	1.4	0.2	0.4	2005, 2007, 2009, 2011

All velocities are relative to stable North America; Euler pole: -6.8°W, -84.8°N, rotating 0.189°/Myr.

Uncertainties are 1σ.

We evaluated the horizontal component of the GPS velocities relative to the strike of plate motion between the Sierra Nevada block and the western Basin and Range (323°), which coincides with the strike of the DV-FLVF (Bennett et al., 2003). In addition, we evaluated the SPLM velocity field relative to the direction of extension on SPLM normal faults striking ~15º.

2.4 RESULTS

The projected velocity fields (Figure 2.1a) show characteristic patterns of distributed shear zone deformation. From east to west across the southern Walker Lane, velocities increase in magnitude and rotate from west-northwest to northwest, reflecting a large diffuse fault zone demarking the transition from Basin and Range to Sierra Nevada block. The northwestward velocity reaches a maximum for sites located on the rigid Sierra Nevada block that are moving nearly uniformly to the northwest (Dixon et al., 2000). When GPS velocities are reprojected to the local plate motion, 323°, the fault parallel velocities across the southern Walker Lane steadily increase along a plate perpendicular transect from northeast to southwest as the sites are located progressively further onto the Pacific plate side of the diffuse boundary (Figure 2.1b). Although the transect crosses the DV-FLVF, the WMF, and the SNFF, the velocity profile is broad and smooth and contributions of individual faults are obscured by close spacing between faults, as we discuss below.

Dislocation modeling of slip on individual faults in the Walker Lane requires a solution that combines interseismic contributions from several faults. With current station

spacing, the velocity gradient across the Walker Lane appears too smooth to identify deformation signals from multiple adjacent faults. We used a modified form of the Savage and Burford (1973) vertical strike-slip dislocation model that includes the contribution of individual offset faults (e.g. Dixon et al., 1995), to account for locking across each the SNFF, WMF, and DV-FLVF. Because of the proximity of faults, useful solutions for locking depths were not possible, and hence we fixed the value to be 15 km for all faults – the depth above which 99% of all observed seismicity in the region has been observed (ANSS Worldwide Earthquake Catalog, accessed April 22, 2013). For comparison we also model the best-fit solution for a single fault, also with a 15 km locking depth. A slight positive apparent shift of the models relative to the southwestern limb is the result of increased data density near the center and northeastern limb. While the solutions for both models are equivalent away from the faults, finding a far field velocity of 10.6 ± 0.5 mm/yr, the distributed faults model more closely matches the approximately linear trend in the near field GPS data (Figure 2.1b). The modeled far field velocity (10.6 ± 0.5 mm/yr) is slightly higher than the observed maximum GPS offset (9.7 ± 0.3 mm/yr, see below) because the model predicts modest interseismic strain accumulation outside the most distal data points we measured. We did not use the measured far field velocity to constrain our model because it would require an unreasonably shallow locking depth. When the San Andreas Fault is included in the dislocation model, its interseismic strain accumulation does not affect our sites in the Walker Lane (Figure 2.2).

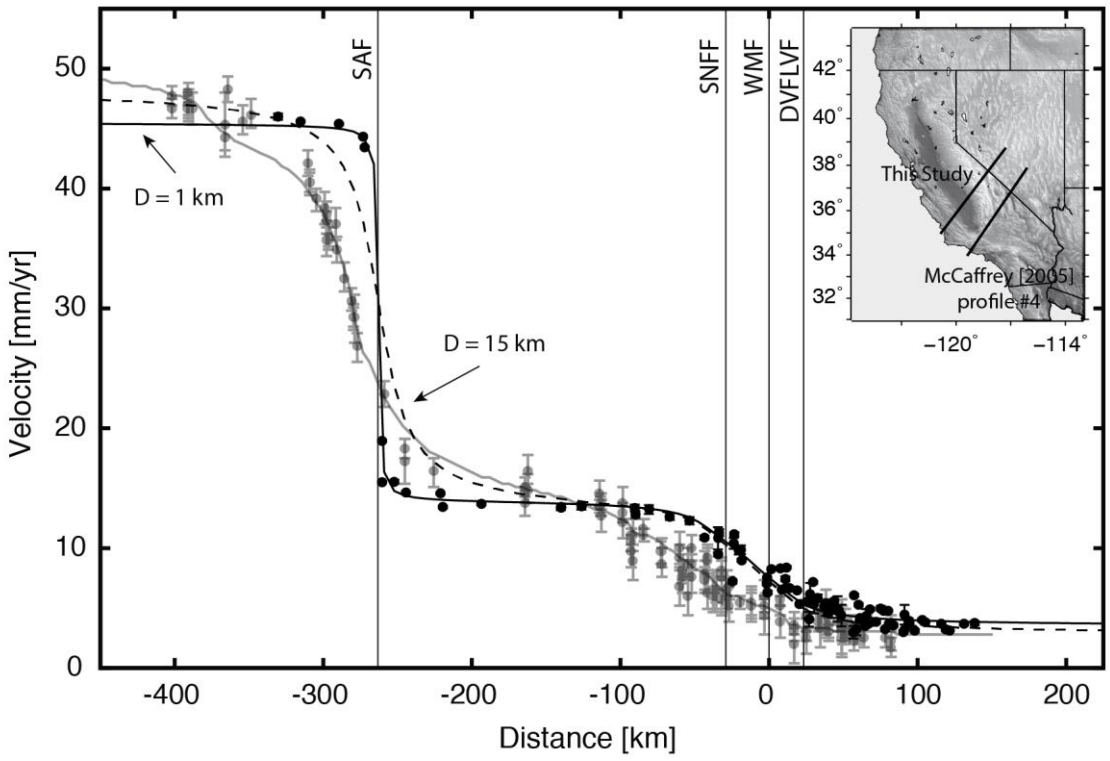

Figure 2.2. Plate parallel velocity profile dislocation models across most of the Pacific-North America plate boundary. Black filled circles and black error bars are data from this study. The profile crosses the San Andreas Fault (SAF), the Sierra Nevada Frontal Fault (SNFF), the White Mountains Fault (WMF), and the Death Valley-Fish Lake Valley Fault (DVFLVF). The dislocation model is similar to those described in the main text, but here includes the SAF. The solid black line is the best-fit model, with 1 km locking depth of the SAF and 15 km locking depth on the SNFF, WMF, and DVFLVF; the dashed black line is the solution for 15 km locking depth on all faults. The sharp gradient across the SAF is due to the proximity to the creeping Parkfield section, which contributes coseismic slip to our measurements of interseismic strain. The dislocation model requires an unreasonably shallow apparent locking depth to account for the coseismic contributions. Our GPS velocities are relative to North America using the Euler pole from the MORVEL reference frame [DeMets et al., 2010]. The absolute amplitude of the displacement field will be shifted ~0.5 mm/yr to the southeast if we use the GEODVEL reference frame [Argus et al., 2010]. For comparison, we also show profile #4 from McCaffrey [2005] (gray filled circles, gray error bars, and gray curve). McCaffrey's [2005] profile crosses the plate boundary further south, at ~36°N, and shows deformation spread over a wider region and a less distinct plateau of velocities across the Sierra Nevada block.

The average velocity of six continuous GPS sites (P245, P305, P512, P629, P725, and MUSB) located on the interior of the Sierra Nevada block is 13.5 ± 0.5 mm/yr toward N50ºW relative to North America, which we use to define the rigid Sierra Nevada block. This velocity encompasses the complete available translation rate expected across the Walker Lane and Basin and Range. The total velocity gradient across the southern Walker Lane at ~37.5ºN, calculated from the difference in plate parallel velocity between P305 and SANA (Figures 2.1a and 2.1b), the two most distal sites perpendicular to plate motion, is 9.7 ± 0.3 mm/yr toward 323°. Removing the Walker Lane vector from the Sierra Nevada vector yields the remaining velocity between the central Basin and Range (site SANA) and North America, ~4.5 mm/yr toward N76°W (Figure 2.1c).

Subsets of the velocity field, which sample narrower swaths, define details of plate-parallel and -normal velocity profiles perpendicularly across the southern Walker Lane (e.g Figure 2.3). The velocity profile in Figure 2.3a is the longest profile across the southern Walker Lane and includes sites on the interior of the Sierra Nevada block. The velocity gradient has nearly constant velocity at either end of the profile, smooth transitions at ~-60 km and ~10 km, and a steep velocity gradient across the middle of the profile. Additional subset velocity profiles can be found in Figures 2.4 and 2.5. A notable feature of almost all the subset profiles is the nearly linear velocity gradient across the shear zone.

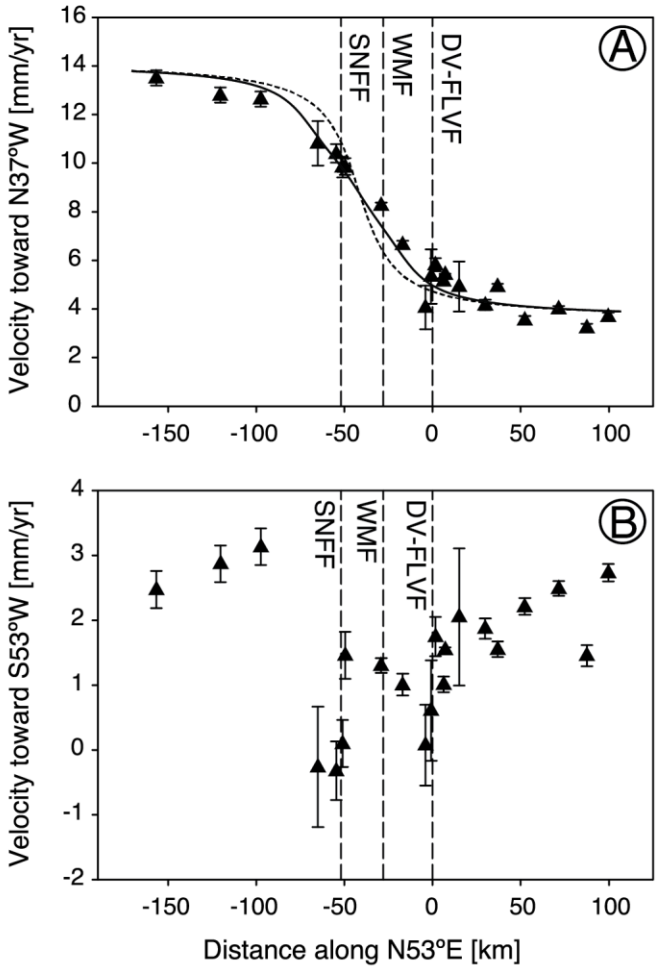

Figure 2.3. Plate-parallel (a) and plate normal (b) velocity profiles across the Walker Lane along transects perpendicular to plate motion, from a subset of the total data set. Dashed vertical lines represent the location of major faults across the transect. Solid curve and dashed curve are the same solutions as shown in Fig. 2.1. SNFF – Sierra Nevada Frontal Fault; WMF – White Mountains Fault; DV-FLVF – Death Valley-Fish Lake Valley Fault.

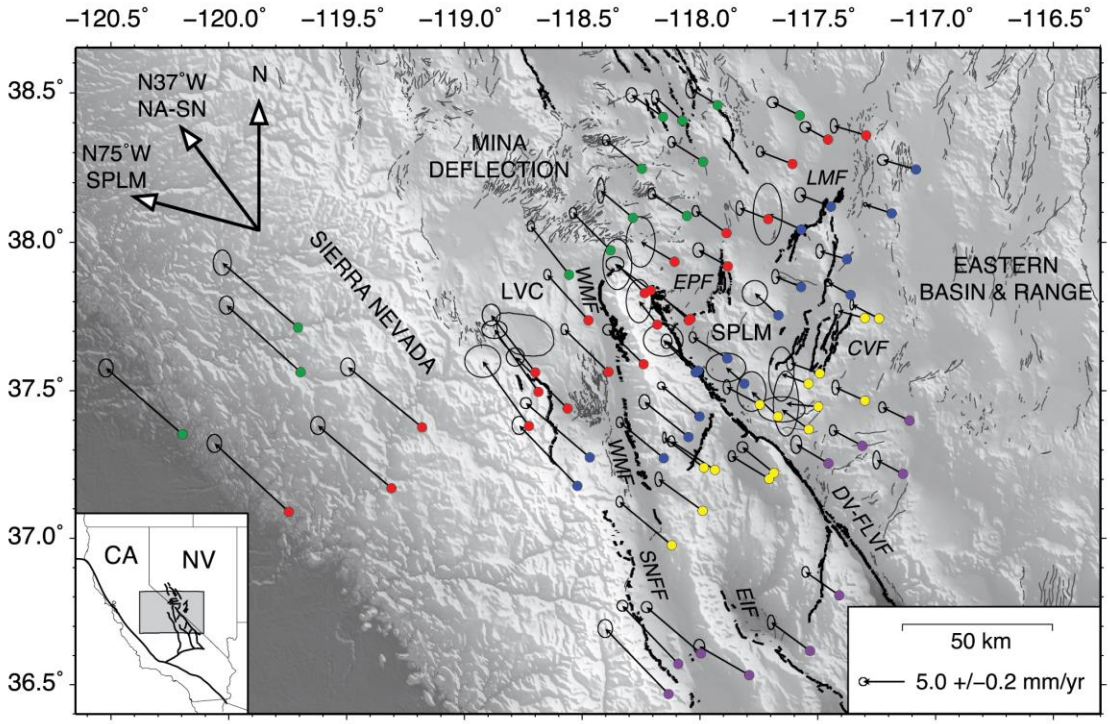

Figure 2.4. Walker Lane GPS velocity field with sited colored by transect. Colors correspond to profiles in Figure 2.5. CVF – Clayton Valley Fault; DV-FLVF – Death Valley-Fish Lake Valley Fault; EIF – Eastern Inyo Fault; EPF – Emigrant Peak Fault; LMF – Lone Mountain Fault; LVC – Long Valley Caldera; SNFF – Sierra Nevada Frontal Fault; SPLM – Silver Peak-Lone Mountain extensional complex; WMF – White Mountains Fault.

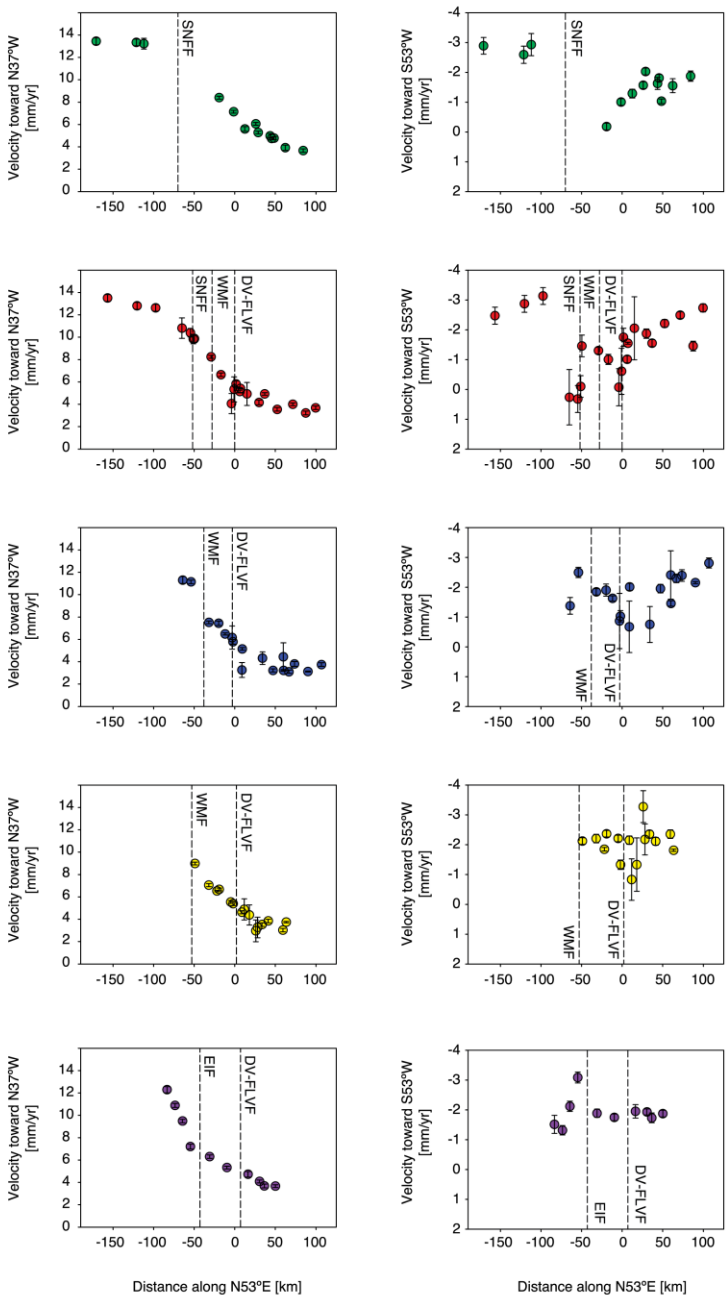

Figure. 2.5. Additional plate-parallel and plate-normal velocity profiles along transects perpendicular to plate motion. Figures in the second row are duplicated from Figure 2.3 and are included here for completeness. Circle colors correspond to circle colors on Fig. S2. DV-FLVF – Death Valley-Fish Lake Valley Fault; EIF – Eastern Inyo Fault; LVC – Long Valley Caldera; SNFF – Sierra Nevada Frontal Fault; SPLM – Silver Peak-Lone Mountain extensional complex; WMF – White Mountains Fault.

Viewing the SPLM GPS velocities reprojected to 285°, the direction of extension perpendicular to the average strike of normal faults, illuminates the nearly linear velocity gradient increasing from SE to NW (Figure 2.6). This increase in velocity in the direction of extension suggests the SPLM is undergoing active diffuse extension.

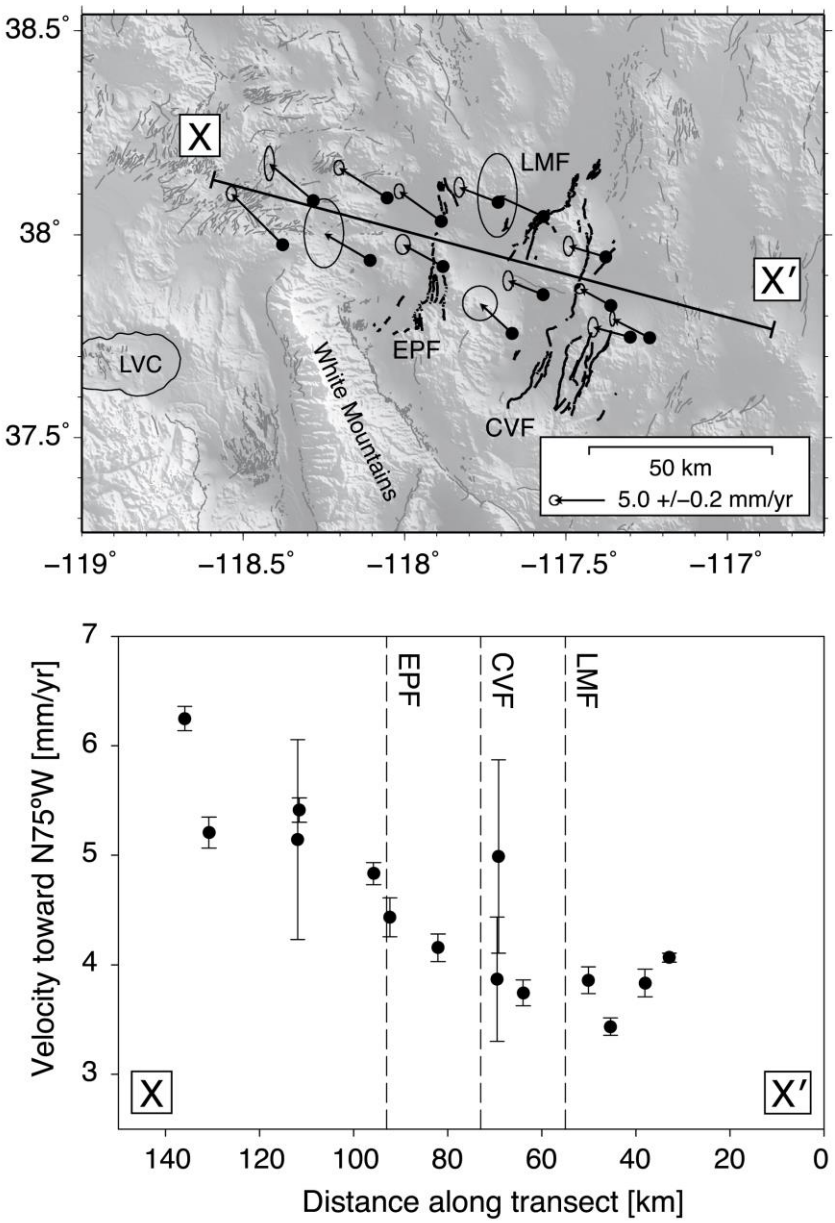

Figure 2.6. (top) Shaded relief map of the SPLM showing GPS velocities and location of transect perpendicular to the strike of SPLM normal faults (~15°). (bottom) SPLM extension-parallel velocity profile corresponding to transect line in top figure. Velocity profile shows extension-parallel velocity increasing toward N75°W, suggesting that there is active extensional deformation occurring across the SPLM. CVF – Clayton Valley Fault; EPF – Emigrant Peak Fault; LMF – Lone Mountain Fault.

2.5 DISCUSSION

Understanding geodetic rates of deformation at higher spatial resolution has implications for resolving the discrepancy between short- and long-term slip rates in the southern Walker Lane. By estimating deformation in smaller regions or across individual faults, we can see where geodetic rates are elevated and predict where geologic rates are likely underestimated. Geologic slip rates can underestimate the strain field in a number of ways. For example, deformation may be distributed off major faults, which leads to underestimated offsets. In addition, some deformation, whether distributed or concentrated on faults, may not be preserved in the geologic record when erosion or scarp degradation occurs. This is particularly problematic in large basins filled with unconsolidated alluvium, as in the Basin and Range.

Late Pleistocene geologic extension rates across the SPLM include 0.1-1.3 mm/yr on the Emigrant Peak Fault (Reheis and Sawyer, 1997), 0.1-0.4 mm/yr on the Lone Mountain Fault (*Hoeft and Frankel*, 2010), and 0.1-0.3 mm/yr on the Clayton Valley Fault (Foy et al., 2012), for a total sum of 0.3-2.0 mm/yr. This wide range of possible rates makes it difficult to constrain the discrepancy between long- and short-term rates, but the maximum is remarkably similar to the ~2 mm/yr of contemporary extensional deformation we observed (Figure 2.6). Thus, if we assume the maximum extension rates on these faults reflect the true slip rates, our data suggest that distributed extension in the SPLM is likely not causing the majority of the observed discrepancy in long- and short-term slip rates. Instead, we find the discrepancy exists across Owens Valley. The plate-parallel GPS velocity gradient across Owens Valley is ~2 mm/yr, while the sum of the late Pleistocene right-lateral slip rates is 0.3-0.4 mm/yr (Kirby et al., 2006). Lee et al.

(2001a) estimated right-lateral slip on the Owens Valley Fault (OVF) to be 1.8-3.6 mm/yr over the Holocene, and proposed that right-lateral slip from the OVF was transferred to the WMF further north. Kirby et al. (2008) estimated even faster late Pleistocene right-lateral slip rates on the OVF between 2.8 and 4.5 mm/yr. If OVF slip transfers north to the WMF, then the discrepancy may range from zero (fully reconciled) to as much as ~4.0 mm/yr of slip that is not accounted for at the latitude of the WMF. The discrepancy here between long- and short-term rates can be the result of several possible factors: 1) geologic slip rates are underestimated, 2) deformation in Owens Valley is distributed among many small structures and a complete record of slip is not preserved, 3) transfer of slip to the west or northwest (e.g. Nagorsen-Rinke et al. [2013]) or 4) Owens Valley is currently experiencing a transient increase in strain. Since long- and short-term slip rates agree in other parts of the Walker Lane, suggesting an absence of transient strain, we favor some combination of the first three factors rather than transient increases in strain rate as an explanation for the discrepancy in Owens Valley. "Missing" slip in the long-term record is more likely broadly distributed deformation on small or poorly preserved structures (e.g. Foy et al., 2012), or underestimated on known structures. The scarcity of quantitative slip rate estimates on the WMF makes it difficult to evaluate the accuracy of previous estimates there, but geomorphic evidence suggests that the west side of the White Mountains has experienced significant tectonic activity. Furthermore, the smooth GPS velocity gradient across the White Mountains block suggests slip is partitioned nearly equally on either side. Yet, right-lateral slip rate estimates at the same latitude on the FLV, which bounds the east side of the White Mountains, are considerably higher

(2.5-3 mm/yr [Frankel et al., 2011]) than the rate on the WMF (0.3-0.4 mm/yr [Kirby et al., 2006]). Thus, late Pleistocene slip rates on the WMF are likely underestimated.

Other factors may contribute to the discrepancy in long- and short-term slip rates. For example, postseismic effects of the 1872 Mw7.6 Owens Valley earthquake may increase the observed contemporary geodetic slip rates because strain accumulation is faster at the beginning of the earthquake cycle (e.g. Hammond et al., 2009; Dixon et al., 2003). However, while some layered viscoelastic dislocation models can account for postseismic relaxation and predict slip rates that agree with long-term geologic slip rates (e.g. Savage and Lisowski, 1998), we believe postseismic effects are not contributing much to the discrepancy because other regions of the Walker Lane-eastern California shear zone that should be similarly affected exhibit no discrepancy between long- and short-term slip rates. Furthermore, the long time series from continuous GPS stations in the region show a clear linear trend in displacement over at least the last ~10 years.

2.6 CONCLUSIONS

Using a dense GPS network across the southern Walker Lane, we investigate the previously observed discrepancy in long- and short-term slip rates. We find that the southern Walker Lane at ~37.5°N accommodates 10.6 ± 0.5 mm/yr of right-lateral slip along the local plate motion direction of 323°, the SPLM is currently undergoing ~2 mm/yr of extensional deformation toward 285°, and Owens Valley accommodates ~2 mm/yr of contemporary right-lateral deformation, compared to 0.4 mm/yr of slip during the late Pleistocene. We conclude that contemporary rates of extension across the SPLM are equivalent to maximum late Pleistocene rates of extension, and that the observed

discrepancy between contemporary geodetic and long-term geologic slip rates across the southern Walker Lane is occurring somewhere in Owens Valley. The discrepancy is likely a combination of underestimated geologic slip rates on the WMF and broadly distributed deformation in Owens Valley that is not well preserved in the geologic record.

CHAPTER 3

QUATERNARY SLIP RATES ON THE WHITE MOUNTAINS FAULT ZONE, EASTERN CALIFORNIA: IMPLICATIONS FOR COMPARING GEOLOGIC TO GEODETIC SLIP RATES ACROSS THE WALKER LANE

3.1 ABSTRACT

The White Mountains fault zone, California is one of the major right-lateral faults that accommodates right-lateral shear across the southern Walker Lane. We combine field geomorphologic mapping and high-resolution airborne LiDAR digital elevation models with $^{40}Ar/^{39}Ar$ geochronology and ^{10}Be cosmogenic nuclide exposure ages to calculate new middle Pleistocene, late Pleistocene, and Holocene right-lateral slip rates on the White Mountains fault zone. A shutter ridge containing 755 ± 7 ka Bishop tuff ash has been right-laterally offset 854 ± 20 m, constraining the middle Pleistocene slip rate to 1.1 ± 0.1 mm/yr. Alluvial fans with ages of 94.0 +18.3/-16.8 ka, 38.4 ± 9.0 ka, and 6.2 ± 3.8 ka have been right-laterally displaced 175 ± 20 m, 73 ± 3 m, and, 11 ± 1 m respectively, yielding slip rates of 1.9 +0.5/-0.4 mm/yr, 1.9 +0.5/-0.4 mm/yr, and 1.8 +2.8/-0.7 mm/yr. These new slip rates elucidate the slip history of the White Mountains fault zone at several time scales, and help resolve the kinematics of the complex Pacific-North American plate boundary. Our results suggest that slip on the White Mountains fault zone has remained remarkably constant from the mid-Pleistocene through the Holocene. These results also help reconcile a portion of the observed discrepancy

between geodetic strain rates and known late Pleistocene slip rates in the southern Walker Lane. In particular, the sum of late Pleistocene slip rates across faults at ~37.5°N latitude in the southern Walker Lane projected to the plate motion accounts for 7.5 +1.1/-0.6 mm/yr, approximately ~70% of the observed geodetic slip rate of 10.6 ± 0.5 mm/yr.

3.2 INTRODUCTION

Understanding spatial and temporal variations in strain accumulation and release along plate boundaries is a fundamental problem in tectonics. Short-term and long-term slip rates are expected to be equal if the regional stress field remains unchanged over time, yet discrepancies between modern geodetic (decadal time scale) slip rates and long-term geologic (10^3-10^6 ka) slip rates have been observed on several major fault systems, including parts of the Pacific-North America plate boundary system (e.g. Bennett et al., 2003; Dolan et al., 2007; Frankel et al., 2007a, 2011; Oskin et al., 2008). Slip rate discrepancies have important implications for the evolution of faults and plate boundaries. Discrepancies may imply that strain is transient and varies in time. For example, clarifying long- and short-term slip rates may lead to a better understanding of characteristic vs. clustered earthquake rupture behavior (e.g. Gold and Cowgill, 2011; Wallace, 1987; Schwartz and Coppersmith, 1984). Or, discrepancies may imply that strain is distributed non-uniformly within a region of uniform far field stress (e.g. Thatcher, 2009). However, it is not clear whether observed discrepancies are real or simply a manifestation of insufficient data. Calculating new slip rates (e.g. Frankel et al., 2011) and revisiting existing slip rates (e.g. Cowgill et al., 2009) have helped reconcile some slip rate discrepancies, however the slip rate discrepancy in the southern Walker

Lane at ~37.5°N remains unresolved (e.g. Kirby et al., 2006; Frankel et al., 2007; Nagorsen-Rinke et al., 2013).

The southern Walker Lane is a diffuse right-lateral shear zone comprising strike-slip faults and extensional step-over normal faults that is thought to accommodate ~20% of the relative motion between the North American and Pacific plates (Bennett et al., 2003; Wesnousky, 2005a; Hammond and Thatcher, 2007; Lee et al., 2009a) (Figures 3.1 and 3.2). However, within parts of the southern Walker Lane the contemporary geodetic deformation rate is twice as high as the geologic deformation rate averaged over the late Pleistocene. The two main right-lateral structures in the southern Walker Lane are the Fish Lake Valley fault (FLVF) and the White Mountains fault zone (WMFZ; Figure 3.2). The FLVF accommodates up to 3.3 +0.7/-0.1 mm/yr of right-lateral motion since ~70 ka (Ganev et al., 2010; Frankel et al., 2011), while the right-lateral slip rate on the WMFZ is ~0.3-0.4 mm/yr since ~22 ka (Kirby et al., 2006). To the east of Fish Lake Valley, faults in the Silver Peak-Lone Mountain extensional complex (SPLM) accommodate shear zone-parallel motion through extension, much like other step-over faults in the Walker Lane such as the Queen Valley fault (Lee et al., 2009a), Deep Springs fault (Lee et al., 2001b), and Tin Mountain fault (Figure 3.2). Within the SPLM, Emigrant Peak fault, Clayton Valley fault, and Lone Mountain fault accommodate 0.1-1.3 mm/yr (Reheis and Sawyer, 1997), 0.1-0.3 mm/yr (Foy et al., 2012), and 0.1-0.4 mm/yr (Hoeft and Frankel, 2010) of slip since the late Pleistocene, respectively. In order to compare geologic slip rates to geodetic slip rates, we reproject all geologic slip rates to the direction of plate motion, 323° (Bennett et al., 2003; Lifton et al., 2013) (Table 3.1). The total late Pleistocene right-lateral slip rate summed across the southern Walker Lane at ~37.5°N is

6.1 +1.0/-0.5 mm/yr, ~60% of the geodetic rate of 10.6 ± 0.5 mm/yr (Lifton et al., 2013) measured by GPS across the same area (Table 3.1).

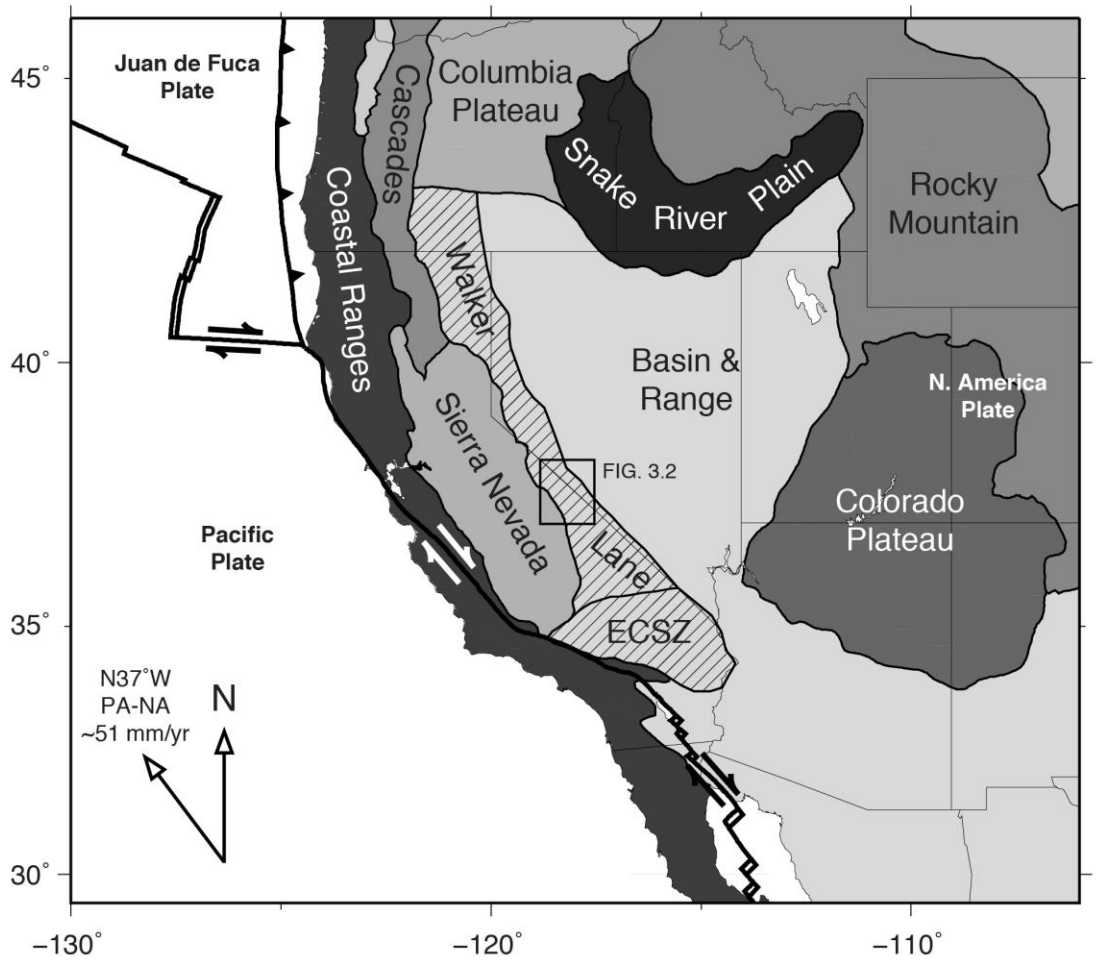

Figure 3.1. Regional tectonic map of the western United States showing physiographic provinces, plate boundaries, and relative plate motion between North American and Pacific plates. ECSZ – eastern California shear zone.

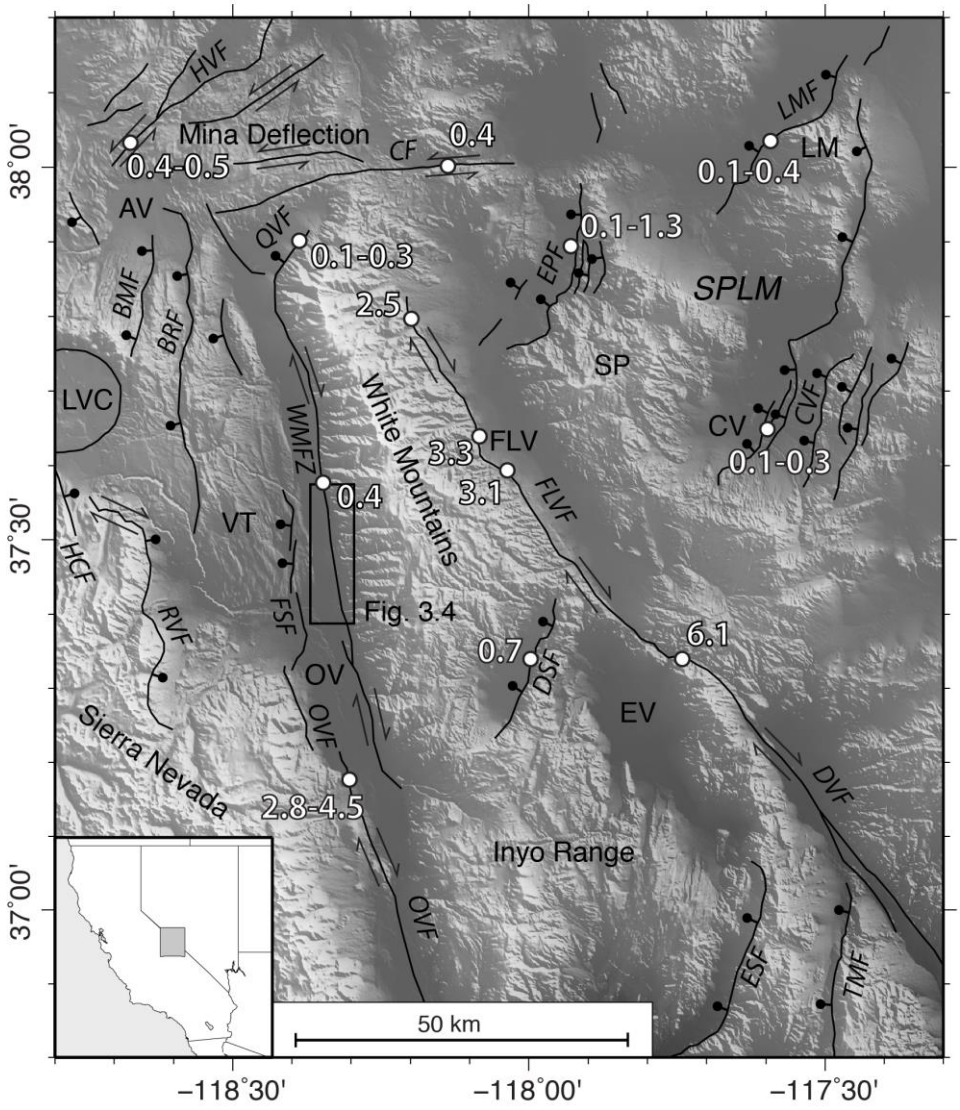

Figure 3.2. Shaded relief map of the southern Walker Lane showing major Quaternary faults. White filled circles are locations of slip rates (white text). Bar and ball is located on the hanging wall of normal faults; arrow pairs indicate relative motion across strike-slip faults. AV – Adobe Valley; BMF – Black Mountain fault; BRF – Benton Range fault; CF – Coaldale fault; CV – Clayton Valley; CVF – Clayton Valley fault; DSF – Deep Springs fault; DVF – Death Valley fault; EPF – Emigrant Peak fault; ESF – Eureka-Saline fault; EV – Eureka Valley; FSF – Fish Slough fault; FLV – Fish Lake Valley; FLVF – Fish Lake Valley fault; HCF – Hilton Creek fault; HVF – Huntoon Valley fault; LM – Lone Mountain; LMF – Lone Mountain fault; LVC – Long Valley Caldera; OV – Owens Valley; OVF – Owens Valley fault; QVF – Queen Valley fault; RVF – Round Valley fault; SP – Silver Peak Range; TMF – Tin Mountain fault; VT – Volcanic Tableland; WMFZ – White Mountains fault zone.

Table 3.1. Geologic slip rates across the southern Walker Lane at ~37.5°N latitude.

Fault	Reference	Reported Rate [mm/yr]	Time Scale [ka]	Direction of Slip [degrees]	Recalculated Slip Rate[b] [mm/yr]	Slip Rate Toward 323° [mm/yr]
WMFZ	Kirby et al., 2006	0.3-0.4	22	355	0.355 ±0.05	0.30 ± 0.04
FLVF	Frankel et al., 2011	3.3 +0.7/-0.1	71	338	3.3 +0.7/-0.1	3.19 +0.68/-0.10
SPLM						
EPF	Reheis and Sawyer, 1997	3.4 +1.8/-0.9[a]	6.5	315	2.0 +0.7/-0.5	1.98 +0.69/-0.50
LMF	Hoeft and Frankel, 2010	0.1-0.4	17	300	0.4 ±0.1	0.37 ± 0.9
CVF	Foy et al., 2012	0.1-0.3	17	320	0.3 ±0.1	0.30 ± 0.1
Sum						**6.1 +1.0/-0.5**
WMFZ	this study	1.9 +0.5/-0.4	38	350	-	1.69 +0.45/-0.36
FLVF	Frankel et al., 2011	3.3 +0.7/-0.1	71	338	3.3 +0.7/-0.1	3.19 +0.68/-0.10
SPLM						
EPF	Reheis and Sawyer, 1997	3.4 +1.8/-0.9[a]	6.5	315	2.0 +0.7/-0.5	1.98 +0.69/-0.50
LMF	Hoeft and Frankel, 2010	0.1-0.4	17	300	0.4 ±0.1	0.37 ± 0.9
CVF	Foy et al., 2012	0.1-0.3	17	320	0.3 ±0.1	0.30 ± 0.1
Sum including this study						**7.5 +1.1/-0.6**

[a] Vertical slip rate, recalculated assuming 60° fault dip

[b] In cases where published slip rates are reported as ranges or reported without uncertainties, we recalculated slip rates based on the original published data using the methods of Zechar and Frankel (2009).

While post-seismic relaxation and other earthquake cycle effects may skew the observed geodetic slip rate, these effects are likely not of high enough magnitude to explain the two-fold discrepancy between geologic and geodetic slip rates. We believe that the previously calculated late Pleistocene slip rate on the WMFZ (0.3-0.4 mm/yr; Kirby et al., 2006) is significantly underestimated given the high slip rates on the Owens Valley fault (up to 3.6 ± 0.2 mm/yr; Lee et al., 2001a; Kirby et al., 2008).

Slip rate estimates for the Owens Valley fault (OVF) vary from 1.8 ± 0.3 mm/yr to 3.6 ± 0.2 mm/yr during the Holocene (Lee et al., 2001a) to 2.8-4.5 mm/yr during the late Pleistocene (Kirby et al., 2008). Lee et al. (2001a) and Sheehan (2007) hypothesized that slip from the Owens Valley fault continues north onto the White Mountains fault zone. However, the estimated late Pleistocene slip rate on the White Mountains fault zone is 0.3-0.4 mm/yr (Kirby et al., 2006), ~10-20% of the right-lateral slip rate along the OVF. This discrepancy in fault slip rates suggests that the estimated slip rate along WMFZ is too low and/or transfer of right-lateral fault slip from the OVF is, at least in part, partitioned northward into the Volcanic Tableland (Nagorsen-Rinke et al., 2013). Reheis and Dixon (1996) hypothesized that the northward decrease in slip rate from the OVF to the WMFZ may be attributed to slip transfer to the FLVF via the Deep Springs normal fault. However, based on geodetic data, Lifton et al. (2013) suggested that most of the observed discrepancy between long- and short-term slip rates at latitude of ~37.5°N may be occurring across Owens Valley. Thus, the WMFZ is an excellent candidate for reevaluating geologic slip rates.

In this study we evaluate (1) the two-fold discrepancy in modern geodetic and late Pleistocene geologic slip rates, and (2) the discrepancy between the predicted transferred

from the OVF to the WMFZ. We calculate four new right-lateral slip rates on the WMFZ using detailed field geomorphologic mapping, high-resolution LiDAR digital elevation models, $^{40}Ar/^{39}Ar$ geochronology, and ^{10}Be terrestrial cosmogenic nuclide (TCN) exposure ages.

3.2.1 Tectonic and Geologic Setting

The White Mountains are a north-northwest striking crustal block within the western boundary of the Basin and Range physiographic province (Figure 3.2). The northern edge of the range is bound by the northeast striking Queen Valley normal fault and the southern edge of the range is adjacent to and continuous with the Inyo Range, but separated by the northeast striking Deep Springs normal fault. The range is bound on the east side by the north-northwest striking Fish Lake Valley right-lateral fault, and on the west by the right-lateral WMFZ. Exposed within the range are Precambrian and Paleozoic metasedimentary rocks and Mesozoic metasedimentary and metavolcanic rocks intruded by numerous Mesozoic plutons related to the arc magmatism that created the Sierra Nevada batholith (Stockli et al., 2003; McKee et al., 1982; Hanson et al., 1987; Crowder et al., 1973; Krauskopf, 1971). The location and trend of the WMFZ appears to be controlled to some extent by a pre-existing Mesozoic shear zone along the western margin of the northern White Mountains (Stockli et al., 2003).

Thermochronologic data from Stockli et al. (2003) suggest that normal faulting on the WMFZ began ~12 Ma with the inception of east-west extension, causing uplift and eastward tilting of the White Mountains block. At ~10-6 Ma, right-lateral strike-slip displacement began along the FLVF on east side of the White Mountains, accompanied by the formation of a shear-directed pull-apart basin in Fish Lake Valley (Stockli et al.,

2003; Reheis and Sawyer, 1997). Normal faults of the WMFZ were reactivated as right-lateral strike-slip faults beginning ~3 Ma, accompanied by extension on Queen Valley and Deep Springs faults step-over transfer zones (Stockli et al., 2003; Lee et al., 2009a; Lee et al., 2001b). Kirby et al. (2006) proposed that slip rates along the WMFZ decreased by a factor of 2-4 sometime between ~755 ka and ~70 ka. Historical activity on the WMFZ includes the July 1986 M6.2 Chalfant Valley earthquake sequence, which produced small right-lateral oblique surface fractures along the WMFZ and within the Volcanic Tableland (Lienkaemper et al., 1987; dePolo and Ramelli, 1987; and Smith and Priestley, 2000). Aftershocks in the sequence appear to trend northwesterly obliquely across Owens Valley, suggesting a possible kinematic link between the WMFZ and faults to the west.

Pliocene and Quaternary alluvial fan deposits along the western side of the White Mountains are cut by a complex array of faults comprising the WMFZ (Figure 3.3). Well-developed strike-slip geomorphic features, such as linear fault scarps, east- and west-facing fault scarps, offset alluvial fans, deflected drainages, closed depressions, ponded alluvium, and shutter ridges from Black Canyon to Piute Creek (Figure 3.3), indicate active right-lateral strike-slip along the WMFZ.

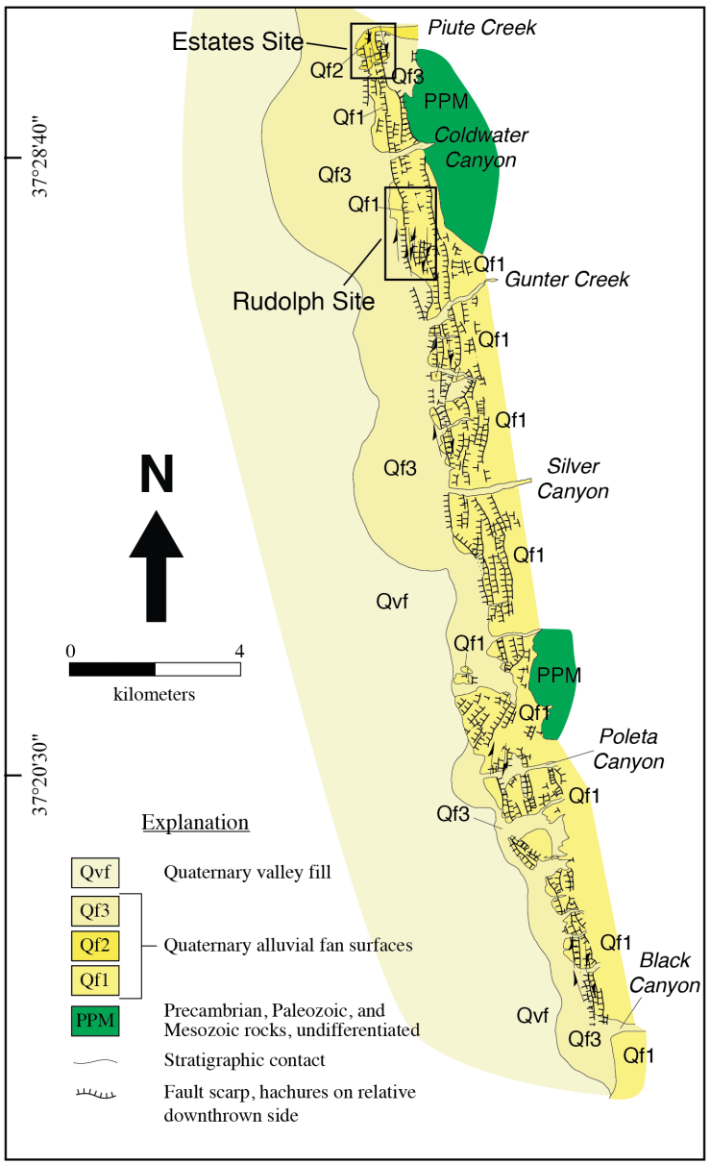

Figure 3.3. Simplified geologic map along the central WMFZ showing major fault scarps cutting alluvial fan surfaces, location of the Estates and Rudolph sites, and major canyons in the White Mountains. Alluvial fan stratigraphy is generalized.

3.3 GEOLOGICAL MAPPING

Based on our mapping along the length of the WMFZ, we identified two sites, the Rudolph site and the Estates site, near the mouths of Coldwater Canyon and Piute Creek, respectively (Figures 3.2 and 3.3), for detailed geologic and geomorphic mapping to document Pleistocene and Holocene slip rates. Mapping was done at 1:10,000 and 1:6,000 scales on low-sun-angle airphotos and LiDAR hillshade digital elevation model (DEM) basemaps, respectively, (Figures 3.4, 3.5 and 3.6). Alluvial fan units were differentiated and placed in a chronostratigraphic framework following the criteria of Bull (1991). These criteria include height above stream channels, degree of dissection, stratigraphy, soil profile development, degree of varnish, and pavement development.

Airborne laser swath mapping (ALSM) data were collected along a swath covering a portion of the White Mountains fault zone (Figure 3.4). Data were collected by the National Center for Airborne Laser Mapping (NCALM) on July 4, 2012 using an Optech Gemini Airborne Laser Terrain Mapper. The swath covered an area of ~40 km^2, with a point density of 9.6 points/$meter^2$. Data were processed to point cloud and 1-m resolution DEM by NCALM. Point cloud and DEM data are available through the OpenTopography data portal: http://www.opentopography.org.

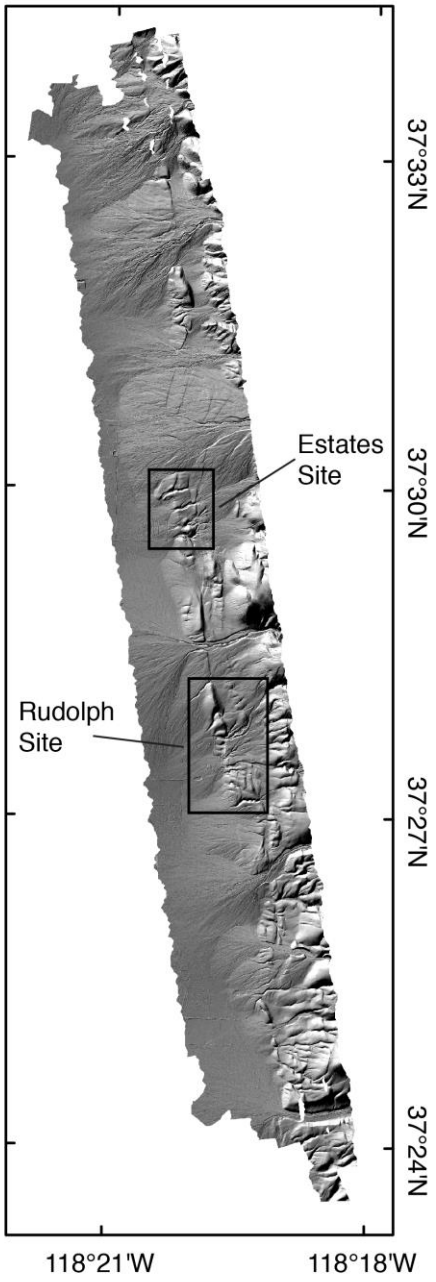

Figure 3.4. Hillshade map of airborne LiDAR swath, with the locations of the Estates and Rudolph sites outlined.

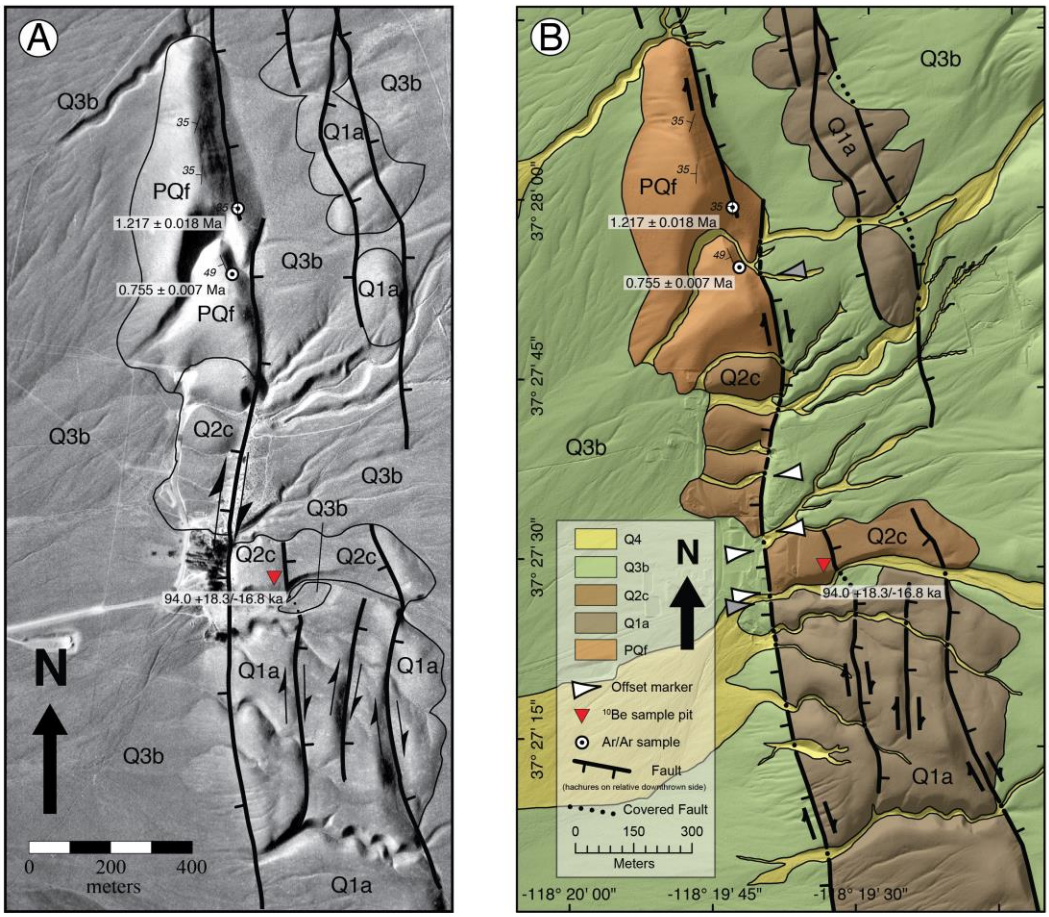

Figure 3.5. (a) Low sun angle aerial photograph (not orthorectified) of the Rudolph site with faults and fan unit contacts. Scale is approximate. (b) Geologic map of displaced alluvial fans at the Rudolph site. White arrows are offset markers for Q2c fan; gray arrows are offset markers for PQf fan.

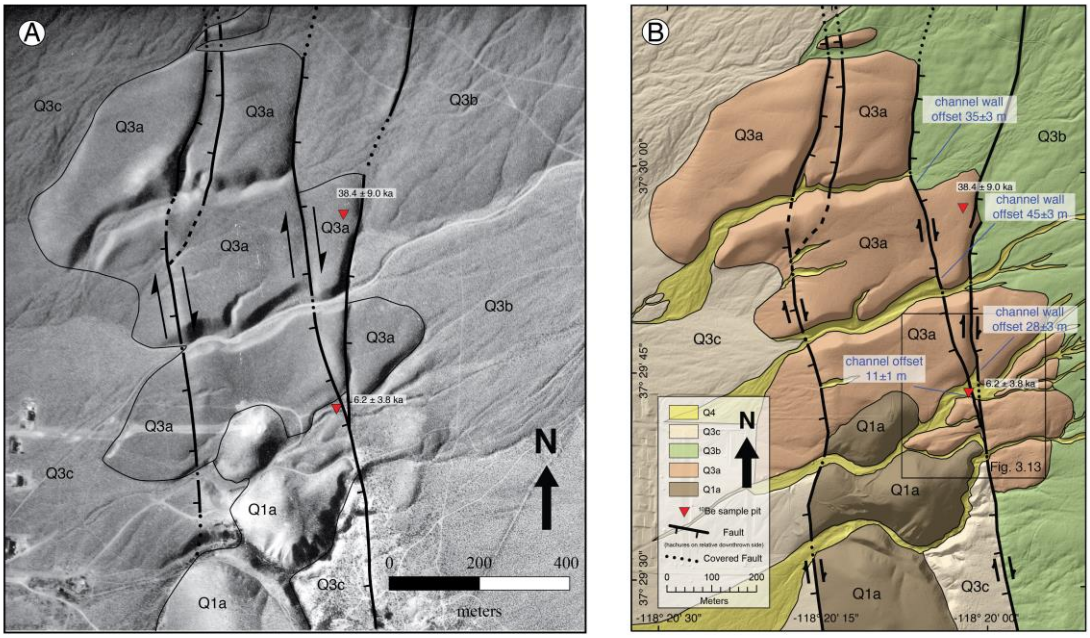

Figure 3.6. (a) Low sun angle aerial photographs (not orthorectified) of the Estates site with faults and fan unit contacts. Scale is approximate. (b) Geologic map of displaced alluvial fans at the Estates site.

3.3.1 Alluvial Fan Stratigraphy

3.3.1.1 PQf Alluvial Fan Unit

The PQf alluvial fan is composed of moderately west tilted Pliocene-Quaternary alluvial fan deposits (Figure 3.5). These deposits are composed of pebble to cobble-sized, angular clasts dominated by phyllite and are locally interbedded with 10s of cm thick tuffaceous sand composed of pumice fragments, feldspar, and quartz and tuffaceous sand supported alluvial fan deposits. Exposed in the lower part of the unit is a 30-60 thick horizon of reworked medium gray, fine-grained pumiceous lithified tephra with fine-grained metapelitic lithic (Paleozoic) fragments which grades upwards into the typical angular clast metapelite alluvial fan deposit. A layer of unconsolidated volcanic ash outcrops on a small stream terrace (location of sample WMFZ05.08 in Figure 3.5) developed into PQf and is therefore younger than the PQf deposits. The PQf surface is deeply dissected and has a ridge-and-ravine morphology typical of a mature fan surface. This surface sits up to 55 m above the active channel. Desert pavement is absent from the PQf surface.

3.3.1.2 Q1a Alluvial Fan Unit

Q1a surfaces are highly dissected into a ridge-and-ravine morphology. The degree of dissection ranges from meters to tens of meters. Q1a surfaces appear light in color in aerial photographs due to the lack of rock varnish. In some localities, desert pavement remnants exist on the apex of ridges, but diffusive processes have degraded them. Soils within Q1a units generally have a 4-5 cm thick Av horizon immediately below the

surface. Below the Av horizon, pebble- to cobble-sized grains have thick pedogenic carbonate coatings. Carbonate stringers appear throughout the soil profile.

3.3.1.3 Q2c Alluvial Fan Unit

The Q2c alluvial fan surface is planar with <10 cm of bar and swale topographic relief. The surface is from ~12 m to as much as ~30 m above the most recently active stream channel. Desert pavement is not well developed; instead, the surface is composed of a thin, non-interlocking veneer of angular to subangular gravel-sized clasts. Clast lithology is primarily fined-grained metasedimentary rock, limestone, and occasional vein quartz. Little to no varnish has developed on surface clasts. Abundant silt underlies, and fills in spaces between, surface clasts. Small shrubs, <1 m in height, are spaced ~3 m apart. While individual clasts in this deposit do not have pedogenic carbonate coatings, the deposit contains a thin layer of pedogenic carbonate at ~100 cm depth. The deposit also contained several cobble-sized clasts composed entirely of pedogenic carbonate that were transported to their current location from a source upstream.

3.3.1.4 Q3a Alluvial Fan Unit

The Q3a alluvial fan surface is planar, with no distinguishable bar and swale topographic relief. A moderately interlocking desert pavement of cobble- and gravel-sized clasts has developed on this surface. Clasts are moderately varnished and rubified, and are composed of fine-grained metasedimentary rock, limestone, and vein quartz. Vegetation on the surface consists of ~50-cm-tall shrubs, spaced ~2-4 m apart. The surface is ~10-15 m above the modern stream channel. Moderately developed pedogenic carbonate coatings occur on some clasts throughout the deposit, but are thickest between

60 cm and 120 cm depth. The deposit is moderately cemented between 60 cm and 120 cm depth.

3.3.1.5 Q4 Alluvial Fan Unit

The Q4 alluvial fan surface is relatively planar. Bar and swale is present, but very subdued and has ~10 cm of topographic relief. The surface is ~1-3 m above the most recently active stream channel. The surface has abundant silt and sand, with a thin veneer of non-interlocking gravel-sized clasts composed of fine-grained metasedimentary rock, vein quartz, and limestone. Desert pavement and desert varnish are absent. Large sage shrubs, ~1-2 m in height, are spaced ~3 apart across the surface. Some clasts have a thin pedogenic carbonate coating, however these may be relict coatings from previous residence of sediment in earlier fan deposits.

3.4 GEOCHRONOLOGY

3.4.1 $^{40}Ar/^{39}Ar$ Dating

We constrained the age of the PQf fan deposits with $^{40}Ar/^{39}Ar$ dates on sanidine crystals from two tephra horizons, one interbedded with the deposits (sample WMFZ05.06A) and another an unconsolitated ash deposit unconformable on top of the PQf deposits (sample WMFZ05.08) (see Figure 3.5 for sample locations and Table 3.2 for analytical data). Total fusion of sanidine grains from sample WMFZ05.06A yields a mean probability distribution $^{40}Ar/^{39}Ar$ age of 1.217 ± 0.018 Ma (1σ) (Figure 3.7) for the interbedded tephra horizon. Total fusion of sanidine grains from sample WMFZ05.08 yields a mean probability distribution $^{40}Ar/^{39}Ar$ age 0.755 ± 0.007 Ma (1σ) (Figure 3.7)

indicating this tephra deposit is Bishop ash (cf. Sarna-Wojcicki et al., 2000). Thus, the PQf fan surface has been offset sometime after 0.755 Ma.

Table 3.2. $^{40}Ar/^{39}Ar$ analytical data.

	ID	$^{40}Ar/^{39}Ar$	$^{37}Ar/^{39}Ar$	$^{36}Ar/^{39}Ar$ (x 10^{-3})	$^{39}Ar_K$ (x 10^{-15} mol)	K/Ca	$^{40}Ar^*$ (%)	Age (Ma)	±1σ (Ma)
	WMFZ05.06A, Sanidine multicrystal, J=0.0008205±0.06%, D=1.002±0.001, NM-213G, Lab#=57527								
#	16	0.9548	0.0078	0.8452	6.130	65.3	73.9	1.044	0.037
	17	0.9691	0.0191	0.5955	8.590	26.7	82.0	1.176	0.031
	20	1.003	0.0154	0.6857	2.715	33.1	79.9	1.186	0.091
	19	0.9396	0.0072	0.3582	6.091	71.1	88.8	1.235	0.042
	18	0.9860	0.0052	0.4991	9.598	98.7	85.1	1.242	0.026
	Mean age ± 1σ	n=4	MSWD=0.97		57.4 ±67.6			1.217	0.018
	WMFZ05.08, Sanidine multicrystal, J=0.000819±0.05%, D=1.002±0.001, NM-213G, Lab#=57528								
	24	1.033	0.0161	1.860	18.308	31.6	46.9	0.716	0.021
	26	0.6948	0.0069	0.6808	11.439	74.1	71.1	0.730	0.022
	21	0.6945	0.0074	0.6774	16.465	69.2	71.3	0.731	0.015
	17	0.7854	0.0071	0.9563	20.381	71.8	64.1	0.744	0.013
	16	0.6365	0.0065	0.4442	18.931	78.4	79.5	0.747	0.014
	23	0.7355	0.0068	0.7741	18.361	74.9	69.0	0.749	0.017
	18	0.6629	0.0063	0.5229	21.609	80.4	76.8	0.752	0.013
	19	0.6821	0.0073	0.5623	16.902	70.0	75.7	0.763	0.016
	27	0.6790	0.0080	0.4986	13.640	63.9	78.4	0.786	0.018
	22	0.6648	0.0076	0.4466	17.030	67.2	80.2	0.788	0.017
	20	0.7585	0.0076	0.7558	17.276	67.1	70.6	0.791	0.016
#	25	0.5264	-0.0028	-1.6025	1.328	-	189.9	1.48	0.17
	Mean age ± 1σ	n=11	MSWD=2.07		68.1 ±26.1			0.755	0.007

Notes:

Isotopic ratios corrected for blank, radioactive decay, and mass discrimination, not corrected for interfering reactions.
Errors quoted for individual analyses include analytical error only, without interfering reaction or J uncertainties.
Mean age is weighted mean age of Taylor (1982). Mean age error is weighted error
of the mean (Taylor, 1982), multiplied by the root of the MSWD where MSWD>1, and also
incorporates uncertainty in J factors and irradiation correction uncertainties.
Decay constants and isotopic abundances after Steiger and Jäger (1977).
symbol preceding sample ID denotes analyses excluded from mean age calculations.
Ages calculated relative to FC-2 Fish Canyon Tuff sanidine interlaboratory standard at 28.02 Ma
Decay Constant (LambdaK (total)) = 5.543e-10/a
Correction factors:
$(^{39}Ar/^{37}Ar)_{Ca}$ = 0.00068 ± 5e-05
$(^{36}Ar/^{37}Ar)_{Ca}$ = 0.00028 ± 2e-05
$(^{38}Ar/^{39}Ar)_{K}$ = 0.0125
$(^{40}Ar/^{39}Ar)_{K}$ = 0 ± 0.0004

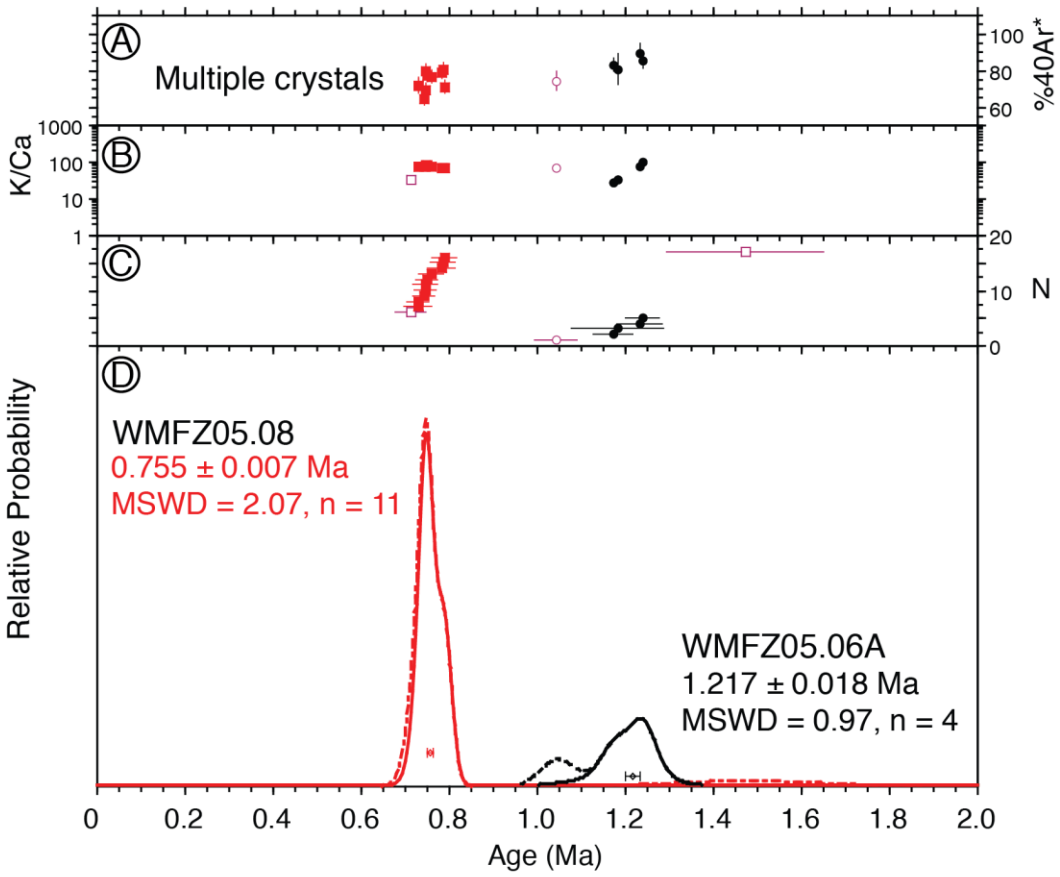

Figure 3.7. Plots of $\%^{40}Ar$ (a), K/Ca ratio (b), individual sanidine grain ages (c), and probability density plot of sandine $^{40}Ar/^{39}Ar$ ages (d) from two tephra layers, WMFZ05.06A and WMFZ05.08, interbedded in PQf fan unit. MSWD, mean square weighted deviation; n = number of sanidine grains analyzed.

3.4.2 TCN Exposure Dating

To determine exposure ages for Q2c, Q3a, and Q4 alluvial fan surfaces we completed depth profiling of ^{10}Be, a terrestrial cosmogenic nuclide (TCN). TCN exposure dating is based on the accumulation in the upper ~2 meters of the Earth's crust of cosmogenic nuclides, which are produced when cosmic rays interact with atomic nuclei in minerals (Lal, 1991; Gosse and Phillips, 2001). Exposure age is a function of several factors, including production rate (which varies with latitude and elevation), radioactive decay rate of the nuclide, and erosion of the surface. In depositional environments, such as alluvial fans, some TCNs may have accumulated in the sediment before it was deposited in the fan. This additional TCN concentration is referred to as inheritance and can be addressed through depth profiling (Anderson et al., 1996), in which TCN concentration is measured at increments below the surface. TCN production decreases quasi-exponentially with depth below the surface and is effectively zero at a depth of ~2-3 meters. Thus any TCN accumulation below the penetration depth of cosmic rays is inherited from previous exposure and can be treated appropriately when modeling ages.

3.4.3 TCN Sample Collection

We dug ~2 m deep soil pits to sample TCNs in three alluvial fan surfaces: Q2c, Q3a, and Q4 (Figures 3.5 and 3.6). Each pit was located on stable, near-horizontal surfaces away from risers and gullies that are affected by diffusive sediment transport processes. Five to seven samples of sediment were taken from 5-10-cm-thick surface-parallel horizons at different depths. Samples within a given pit were collected from a single massive debris flow deposit; we avoided sampling across unconformities.

In addition to subsurface samples, we also collected an amalgamated surface sample of quartz-rich clasts from each of the fan surfaces immediately surrounding the soil pits. The amalgamations consist of 34, 35, and 139 clasts for Q2c, Q3a, and Q4 surfaces, respectively. Surface clasts ranged in mass from 5 to 27 grams, with approximate dimensions of 3 cm by 3 cm by 3 cm.

3.4.4 TCN Sample Preparation

Samples were prepared at the Georgia Tech TCN Geochronology Lab following standard methods (e.g. Kohl and Nishiizumi, 1992). Depth profile samples were sieved to isolate the appropriate size fraction. The 250-500 μm size fraction is ideal for depth profile analysis, but in some cases we expanded the range of grain size in order to retain enough material for analysis. We used the 125-500 μm size fraction for the Q2c depth profile, the 250-710 μm size fraction for the Q3a depth profile, and the 125-710 μm size fraction for the Q4 depth profile. Surface clasts were crushed and mixed into a single amalgamation for each surface, and then sieved to isolate the 250-500 μm size fraction. Quartz was isolated and purified with a series of HF leaches in heated ultrasonic tanks. After dissolution, Be was extracted from the quartz by ion exchange chromatography, then precipitated as $Be(OH)_2$ and oxidized to BeO. The BeO was mixed with niobium powder and packed in a target. The $^{10}Be/^{9}Be$ ratio of each sample was measured by accelerator mass spectrometry at the Center for Accelerator Mass Spectrometry at Lawrence Livermore National Laboratory (CAMS-LLNL). Isotopic ratios were normalized to standard 07KNSTD3110 with a value of 2.85×10^{-12} (Nishiizumi et al., 2007). TCN sample data can be found in Table 3.3.

Table 3.3. ^{10}Be cosmogenic nuclide depth profile analytical data.

Sample	Lon. [°E]	Lat. [°N]	Elev. [m]	Depth [cm]	Size fraction [µm]	Shielding Factor[a]	Quartz [g]	Be carrier mass [g]	Be carrier concentration [ppm]	^{10}Be/^{9}Be[b,c] corrected for blank [x10^{-13}]	^{10}Be concentration[d] [atoms/g]	^{10}Be concentration error[c] [atoms/g]	AMS error[c] [%]	Total measured error[e] [%]
Q4	-118.33387	37.49553	1388											
WM-11-03a				183-193	125-710	1	33.8531	0.2929	1354	10.00 ± 0.19	780241	16571	2.12	3.28
WM-11-03b				145-155	125-710	1	38.0837	0.2926	1354	11.25 ± 0.21	779935	16520	2.12	3.28
WM-11-03c				105-115	125-710	1	56.6096	0.2985	1354	16.59 ± 0.51	790252	25409	3.22	4.07
WM-11-03d				75-85	125-710	1	45.1364	0.2969	1354	12.99 ± 0.24	771304	16330	2.12	3.28
WM-11-03e				55-65	125-710	1	44.5907	0.2928	1354	13.00 ± 0.24	770487	16296	2.11	3.27
WM-11-03f				38-44	125-710	1	71.4777	0.2925	1354	17.04 ± 0.55	629758	21316	3.38	4.21
WM-11-04				0		1	87.9044	0.3093	1354	27.02 ± 0.52	858583	18744	2.18	3.32
Q3a	-118.33408	37.49924	1408											
WM-11-08b				120-130	250-710	1	46.5856	0.3058	1354	18.47 ± 0.42	1094780	27032	2.47	3.51
WM-11-08c				80-87	250-710	1	46.7700	0.3057	1354	19.83 ± 0.37	1170734	24599	2.10	3.27
WM-11-08d				50-60	250-710	1	46.5875	0.3065	1354	22.87 ± 0.43	1359230	29057	2.14	3.29
WM-11-08e				30-37	250-710	1	39.7717	0.3063	1354	19.03 ± 0.36	1323124	28351	2.14	3.29
WM-11-06				0		1	105.1283	0.3103	1354	55.76 ± 0.22	1487481	60446	4.06	4.77
Q2c	-118.32609	37.45831	1381											
WM-11-13a				190-200	125-500	1	50.9229	0.3169	1354	16.96 ± 0.25	953252	16851	1.77	3.06
WM-11-13b				140-150	125-500	1	42.4453	0.3153	1354	16.77 ± 0.41	1125402	30041	2.67	3.66
WM-11-13c				100-110	125-500	1	40.0875	0.3157	1354	18.46 ± 0.23	1313547	20883	1.59	2.96
WM-11-13d				70-80	125-500	1	43.4145	0.3049	1354	16.99 ± 0.26	1077935	19713	1.83	3.10
WM-11-13e				45-55	125-500	1	30.6647	0.3119	1354	12.25 ± 0.33	1125025	32641	2.90	3.83
WM-11-13f				30-35	125-500	1	38.3344	0.3134	1354	14.60 ± 0.28	1078289	23583	2.19	3.32
WM-11-12				0		1	119.6931	0.3096	1354	82.69 ± 0.35	1933526	84744	4.38	5.05

[a] Horizon is <12° in all directions, thus no geometric correction is necessary.

[b] Isotopic ratios were normalized to standard 07KNSTD3110 with a value of 2.85 x 10^{-12} (*Nishiizumi et al.*, 2007).

[c] Uncertainties reported at 1σ confidence level.

[d] Samples were corrected for background using blank values of 125,455 ± 15,852 for WM-11-04, WM-11-06, and WM-11-12; 72,957 ± 9,365 for WM-11-03;
89,208 ± 11,621 for WM-11-08; and 61,353 ± 8,818 for WM-11-13.

[e] Total measured error includes a 2.5% 1σ error in sample preparation added in quadrature to the 1σ AMS error (e.g. *Hidy et al.*, 2010; *Gosse and Phillips*, 2001).

3.4.5 TCN Exposure Age Modeling

We followed the methods of Hidy et al. (2010) to model our depth profiles and calculate exposure ages. The Hidy et al. (2010) model is a Monte Carlo simulator that takes into account site-specific geological constraints to find the most probable age, erosion rate, and inheritance, while propagating uncertainty for each. For our age models we used a sea level, high latitude ^{10}Be production rate of 4.76 atoms g^{-1} a^{-1}, scaled for our locations (Lal, 1991; Stone 2000; Nishiizumi et al., 2007). Since the horizon was less than 12° in all directions, our samples did not require a topographic correction and we used a shielding factor of 1. We allowed sediment density in the model to vary within a reasonable range for alluvial sediment, from 1.8 g/cm^3 to 2.4 g/cm^3. Erosion rate varied between -3 and 3 cm/ka, while net erosion varied between -50 and 50 cm, with negative values representing aggradation. We allowed the inheritance values in the model to vary from a maximum equal to the concentration of the deepest sample, to a minimum equal to half of that value.

We excluded three samples (30 cm, 45 cm, and 70 cm depth) from our model of the Q2c depth profile because they appear to have undergone mixing and they do not follow the expected theoretical relationship between ^{10}Be concentration and depth. The remaining three depth profile samples and one surface sample from the Q2c fan did not pass the chi-square test at the 95% confidence interval window, and thus we could not rigorously constrain the exposure age of that fan. However, by increasing the size of the confidence interval window of the model fit to 99.73% (3σ), we were able to model an age of 94.0 +18.3/-16.8 ka (Figure 3.8). While this provides a reasonable estimate of the fan exposure age, we emphasize that this age and its associated uncertainty is not well

constrained. We used a second method, the CRONUS-Earth calculator (Balco et al., 2008), for estimating the exposure age of the Q2c fan. This method uses the surface amalgamation ^{10}Be concentration minus the ^{10}Be concentration of the deepest sample and yielded a model age of 83.1 ± 10.4 ka. This is the same, within uncertainty, as our estimate from depth profile modeling and provides support for a Q2c exposure age in the 70-115 ka range.

We modeled exposure ages that passed the chi-square test at the 95% (2-sigma) confidence interval window for the Q3a and Q4 fans. The Q3a depth profile consists of four subsurface samples and one surface sample. The modeled exposure age and 1σ uncertainty for the Q3a fan is 38.4 ± 9.0 ka (Figure 3.8). The Q4 depth profile consists of six subsurface samples and one surface sample. We excluded from our model the sample at 38 cm depth because it does not follow the theoretical relationship between ^{10}Be concentration and depth. The modeled exposure age and 1σ uncertainty for the Q4 fan is 6.2 ± 3.8 ka (Figure 3.8).

Our fan exposure ages overlap, within uncertainty, with several published fan exposure ages in the Walker Lane, eastern California shear zone, and Death Valley region lending confidence to the accuracy of our exposure ages (Figure 3.9).

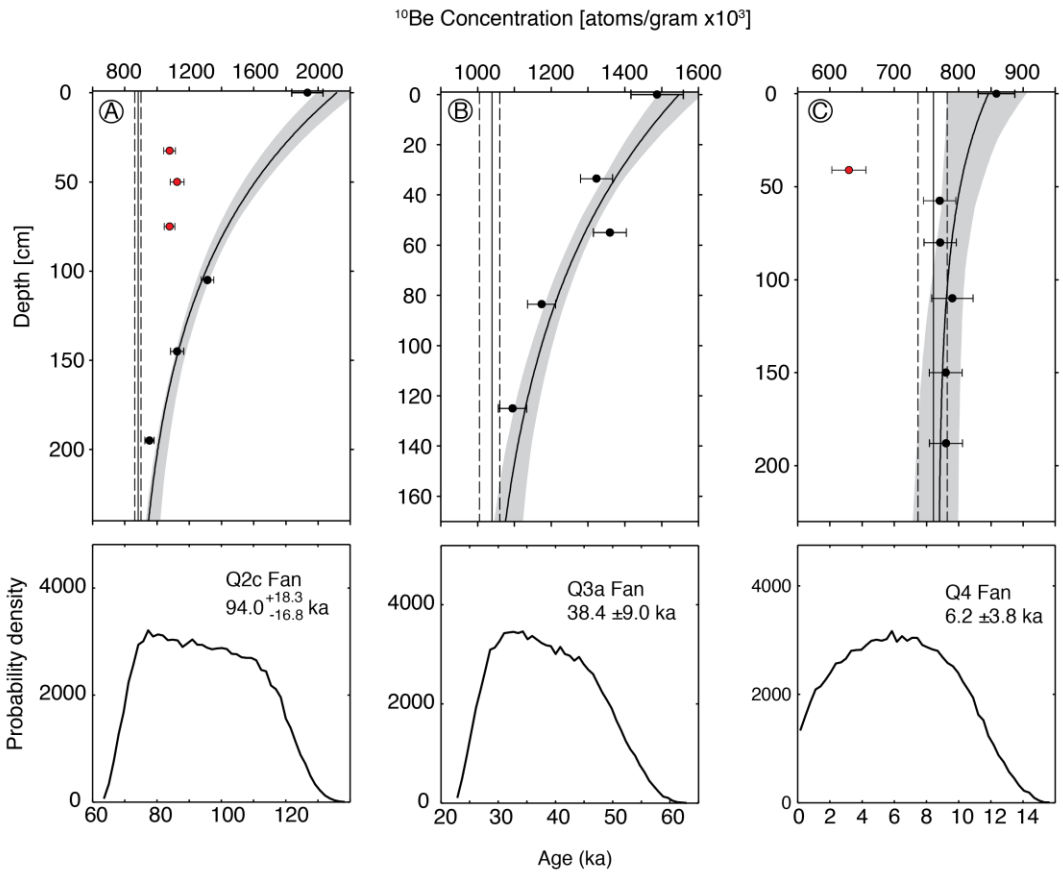

Figure 3.8. ^{10}Be depth profile models (top) and exposure age probability density functions (bottom) from three fan surfaces (a) Q2c, (b) Q3a, and (c) Q4. Circles are ^{10}Be concentrations measured by AMS; horizontal error bars are the total 1σ uncertainties accounting for errors in both preparation and measurement. Black circles were used in the model solutions; red circles were excluded from model solutions. Solid black curve is the best fit from the Hidy et al. (2010) Monte Carlo simulation; gray envelope is the range of model fits. Vertical solid line represents the best-fit inheritance value and dashed vertical lines are the 1σ uncertainty range for inheritance.

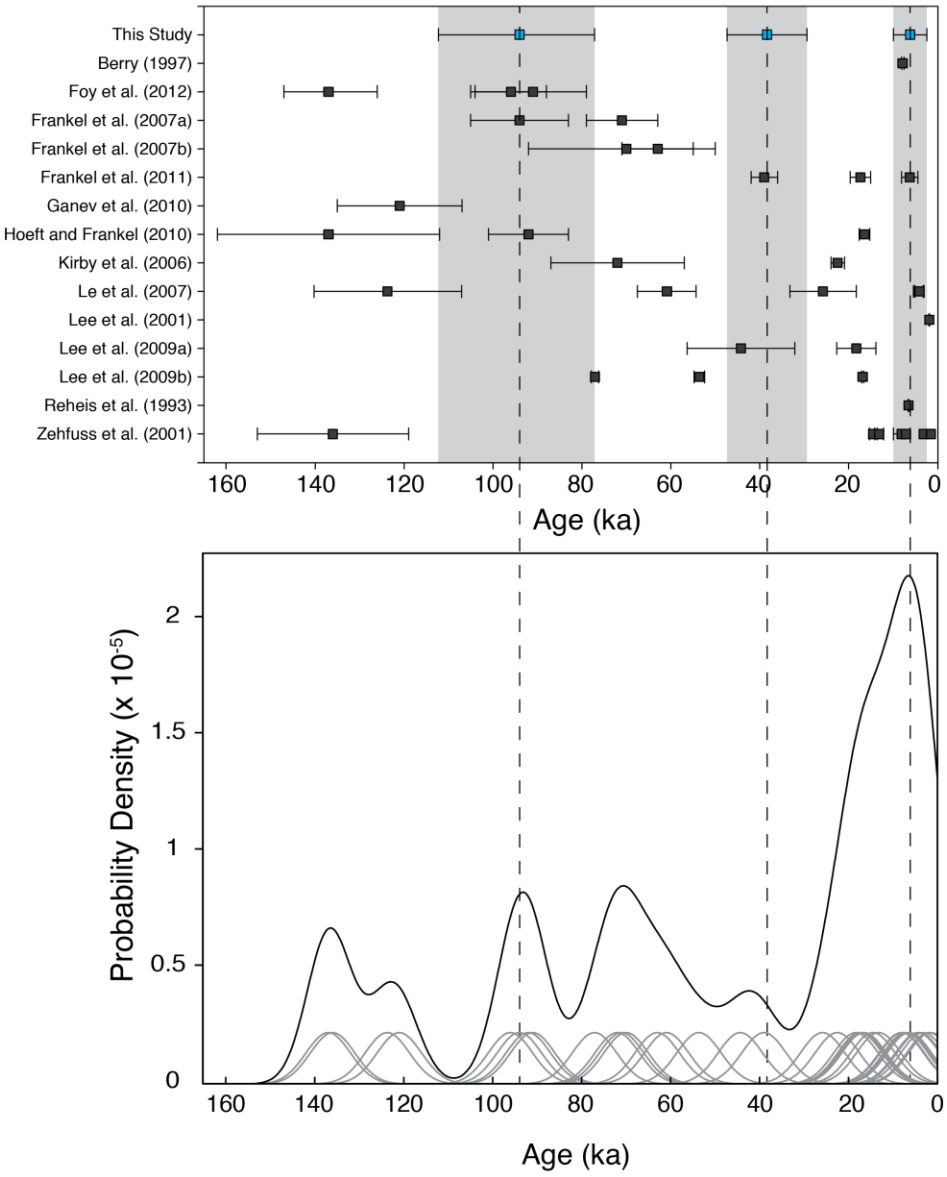

Figure 3.9. (a) Ages from this study (blue) compared to selected alluvial fan ages and uncertainties reported in the eastern California shear zone, Walker Lane, and Death Valley region. Dashed vertical lines correspond to our ages and the gray shaded regions correspond to the 1σ uncertainties associated with those ages. (b) Probability density function (PDF) of published ages (excluding ages from this study). Grey curves are individual age PDFs and black curve is total PDF. Note that the uncertainty for all ages is uniform when calculating the PDF to avoid biasing the total PDF toward ages with low uncertainties.

3.5 FAULT GEOMETRY, GEOMORPHOLOGY, SLIP MAGNITUDE, AND SLIP RATES

The WMFZ is approximately 500-1000 m wide and consists of up to four subparallel strands that cut through the alluvium along the western range front of the White Mountains. The average strike of fault zone is ~353°; the average strike at the Estates site is ~348° and the average strike at the Rudolph site is ~351°. WMFZ fault scarps are generally west facing, although in several places they face east. The alternation between west and east facing scarps along short section of the fault scarp suggests that apparent vertical offset is the result of lateral displacement of high topography juxtaposed against low topography. Scarps range in height from 1-4 m.

The WMFZ cuts and offsets PQf, Q2c, and Q3a, and Q4 alluvial fans surfaces at both field sites (Figures 3.5 and 3.6). Fault displacement measurements were made from the 1-m-resolution LiDAR DEM using the Lateral Displacement Calculator (LaDiCaoz) MATLAB software package (Zielke and Arrowsmith, 2012). LaDiCaoz treats the cross-sectional profiles of stream channels or fan risers as waveforms. The user defines a fault plane, a cross-sectional profile of the offset stream channel on each side of the fault, and the angle that the offset channel projects onto the fault. One channel profile is stretched, vertically shifted, and horizontally translated along the fault plane relative to the second profile in order to get the best fit between offset channels. We used channels, channel walls, and alluvial fan risers as offset markers when backslipping the fault (Figure 3.10). LaDiCaoz calculates a Goodness of Fit parameter when matching channel profiles, but it does not explicitly calculate uncertainties in displacement measurements. Therefore, we

estimate uncertainties in displacement measurements based on the range of values that provide a reasonably good reconstruction of offset markers.

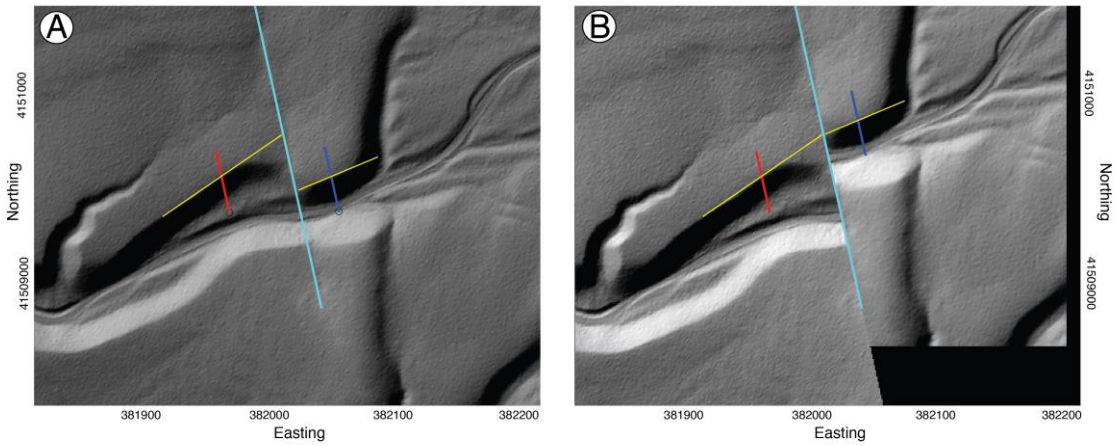

Figure 3.10. An example of application of the Lateral Displacement Calculator (LaDiCaoz). (a) 1-m resolution LiDAR hillshade model of the Q3a showing 45 ± 3 m right-lateral offset of channel wall and the Estates site. Cyan line is the fault plane; yellow lines define the trend of the channel wall projected onto the fault; red and blue lines are channel wall profiles. (b) 1-m resolution LiDAR hillshade model backslipped 45 m to restore the channel wall.

At the Rudolph site, we document displacement of the PQf and Q2c alluvial fans. The PQf fan at the Rudolph site consists of a prominent, high shutter ridge that has been dissected and rounded by diffusive processes. We use a large channel that has been deeply incised through the shutter ridge as an offset marker for the PQf fan. Matching this channel on the west side of the fault to the only stream channel on the east side of the fault large enough to cut through the shutter ridge results in right lateral displacement of 854 ± 20 m (see gray offset marker arrows in Figures 3.5 and 3.11). Our estimate of uncertainty for this measurement is based on the obliquity of the channel projection onto the fault plane. Variations in our reconstruction of the channel and its trend result in a range of offset values that vary by ± 20 m. We measure displacement of the Q2c fan by restoring the northern and southern edges of two small exposures of the fan on either side of the fault (see white offset marker arrows in Figures 3.5 and 3.11). The Q2c fan is right-laterally displaced 175 ± 20 m. The uncertainty of this measurement is due to anthropogenic disruption of the original fan surface on the west side of the fault that obscures the edge of the fan.

At the Estates site the WMFZ displaces Q3a and Q4 alluvial fans. The Q3a surface is deeply incised by three SW-flowing channels, and offset of these channel walls provide robust markers for measuring offset. At least four strands of the fault cut the Q3a fan, however offset markers are only preserved along two strands. We measured three channels incised into the Q3a fan of that are right-laterally displaced 35 ± 3, 45 ± 3 m, and 28 ± 3 m (Figures 3.6 and 3.12). The 35 ± 3 m offset occurs where a previously continuous northwest-facing channel wall has been right-laterally offset and the fan on the eastern side of the fault has been partially buried by younger Q3b fan deposits. The

eastern channel wall remains exposed above the Q3b deposits and can be restored back to its original position. The 45 ± 3 m offset occurs where a southeast-facing channel wall has been displaced, leaving a downstream-facing scarp that has been shielded from erosion (Figures 3.6, 3.10, and 3.12). Diffusive processes have deposited some material in the shielded corner behind the scarp, but the scarp is clearly expressed and the projection of the unaltered channel wall into the scarp is also clear. The 28 ± 3 m offset also occurs where an offset southeast-facing channel wall has created a downstream-facing shielded scarp. The maximum displacement on the two fault strands is additive and thus our estimate of the minimum displacement of the Q3a fan is 45 ± 3 m plus 28 ± 3 m, or a total of 73 ± 3 m. Our estimate of uncertainty for this measurement is dictated by our ability to locate the channel walls. This displacement measurement is a minimum because additional unmeasured displacement has occurred on the adjacent fault strands. An incised ephemeral stream channel records right-lateral displacement of the Q4 fan (Figures 3.6 and 3.13). The offset occurs near the bifurcation of the fault into two subparallel strands. The fault is expressed as a small (~1 m) west-facing scarp in the Q4 alluvial fan. We use the thalweg of the deflected stream channel to determine total Q4 fan displacement of 11 ± 1 m. Because this channel is small, the uncertainty of this measurement is dictated by our ability to estimate the location of the channel on the 1-m resolution LiDAR DEM.

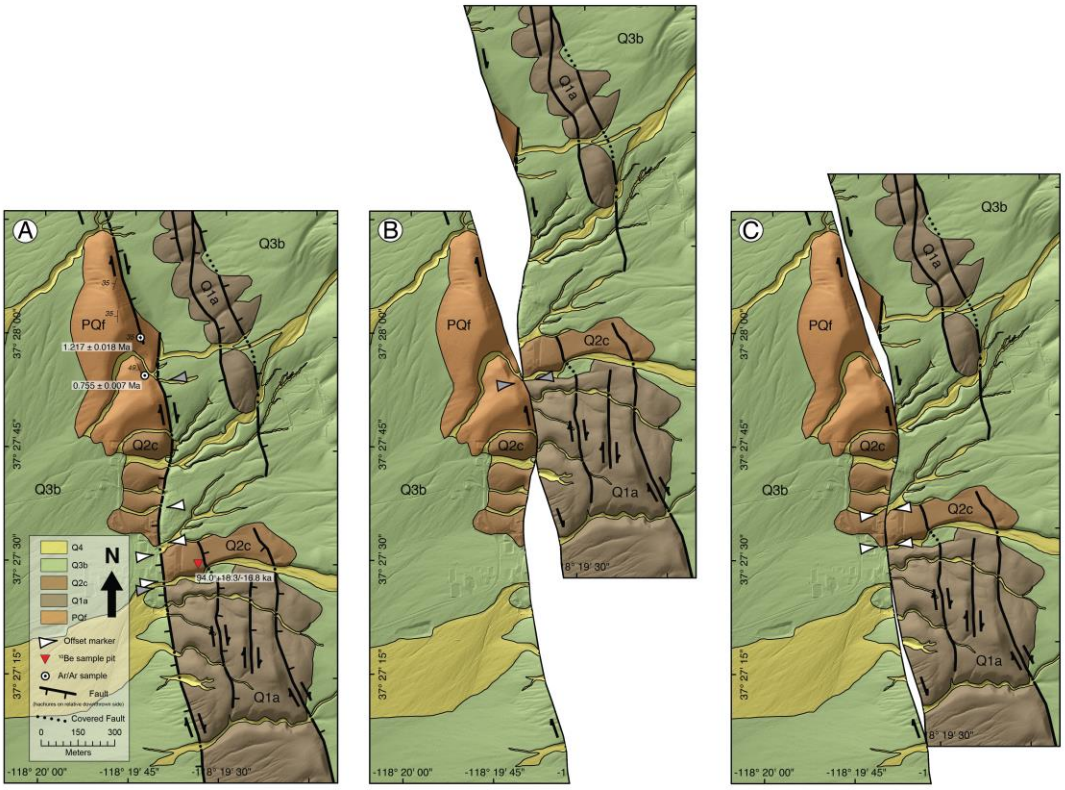

Figure 3.11. (a) Geologic map of displaced alluvial fans at the Rudolph site. White arrows are offset markers for Q2c fan; gray arrows are offset markers for PQf fan. (b) Backslipped geologic map showing 854 ± 20 m restoration of a channel that incises the PQf surface. (c) Backslipped geologic map showing 175 ± 20 m restoration of offset Q2c fan surface.

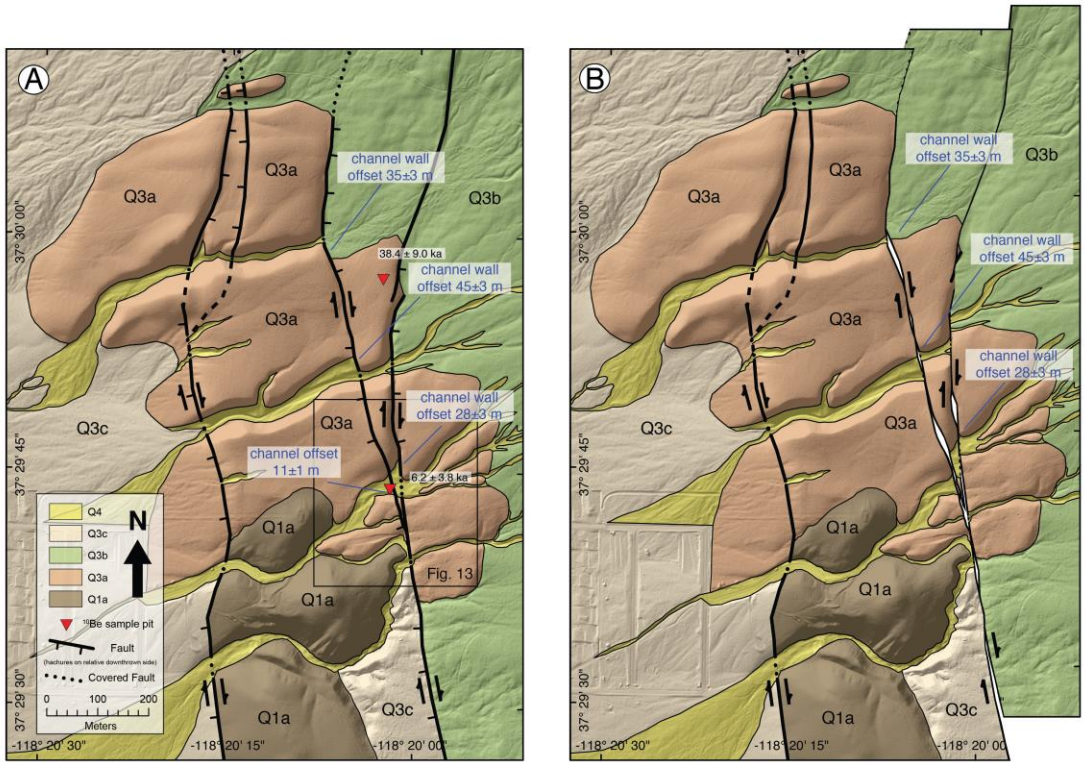

Figure 3.12. (a) Geologic map of displaced alluvial fans at the Estates site. (b) Backslipped geologic map showing restored Q3a alluvial fan surface. The Q3a alluvial fan surface is displaced a total of 73 ± 3 m by two strands of the WMFZ (see Figure 3.10 for an example of Q3a offset). A small abandoned channel in the Q4 fan surface is offset 11 ± 1 m (see Figure 3.13 for details of Q4 offset).

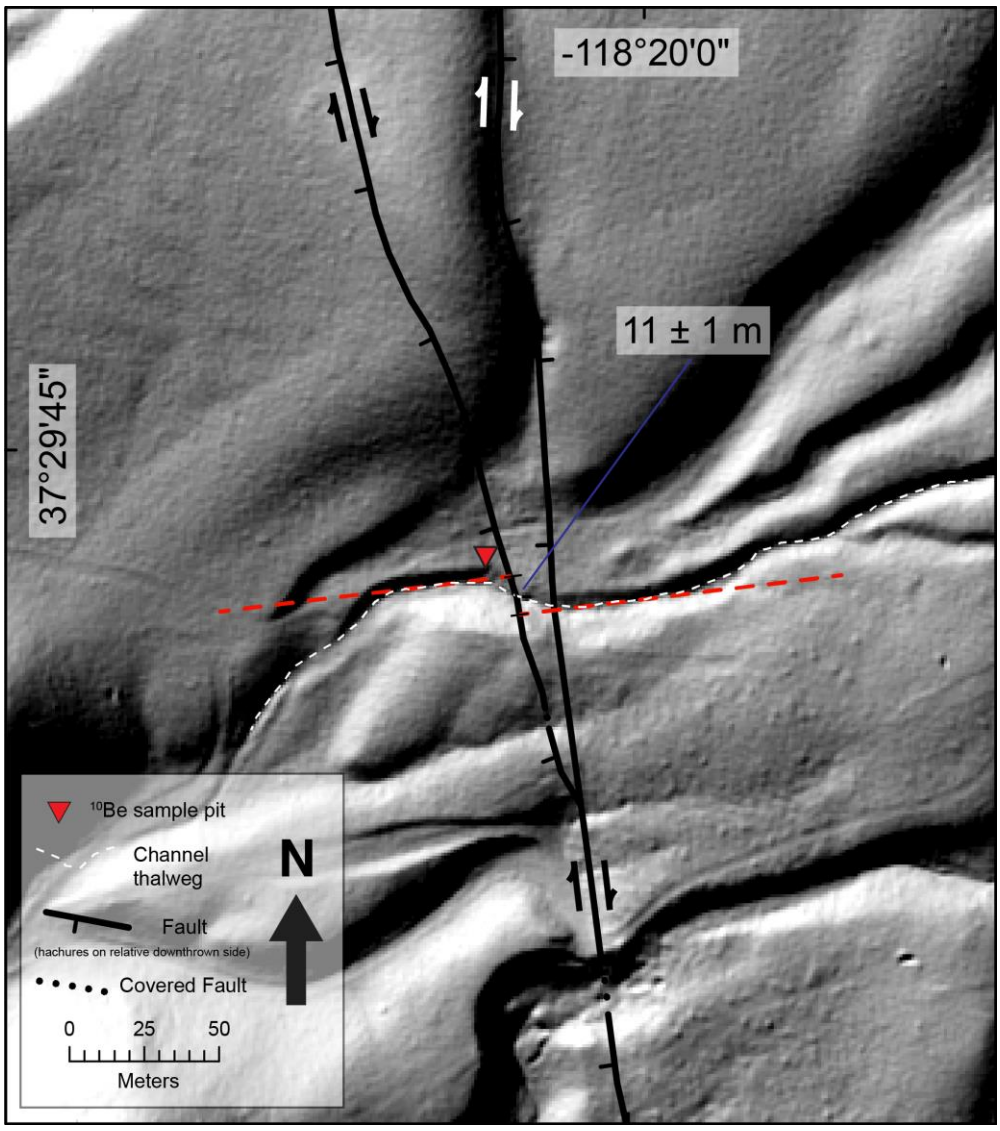

Figure 3.13. Hillshade topographic map derived from 1-m resolution LiDAR data showing fault scarp and 11 ± 1 m offset of ephemeral stream channel. White dashed line is the channel thalweg; red dashed lines define the trend of the thalweg projected onto the fault.

We calculated right-lateral fault slip rates using the methods of Zechar and Frankel (2009), in which ages and displacements are treated as probability density functions (PDF). This probabilistic approach explicitly propagates the uncertainty of each measurement through the slip rate calculation. We treat the displacement measurements as Gaussian PDFs because we assume symmetric uncertainty for those measurements. However, the age PDFs produced by the Hidy et al. (2010) model are asymmetric, so we treat those as arbitrary PDFs in the Zechar and Frankel (2009) model.

Given the displacements and ages described above, we calculate right-lateral slip rates of 1.1 ± 0.1 mm/yr, 1.9 +0.5/-0.4 mm/yr, 1.9 +0.5/-0.4 mm/yr, and, 1.8 +2.8/-0.7 mm/yr along the WMFZ for the PQf, Q2c, Q3a, and Q4 fan surfaces, respectively (Figure 3.14 and Table 3.4). When estimating slip rates on faults cutting alluvial fans, we make three important assumptions: (1) the alluvial fan was deposited in one event that occurred instantaneously; (2) accumulation of TCNs began as soon as the alluvial fan was deposited; and (3) the fault displaced the alluvial fan soon after it was deposited, isolating the fan surface from further deposition and allowing it to be preserved. In other words, the exposure age of the fan is a maximum age for fault offset since it is possible the fault offset the fan long after the fan was abandoned. As a result of these assumptions, and the fact that all but the Q4 displacement measurements are minima, the slip rates we estimate are minima.

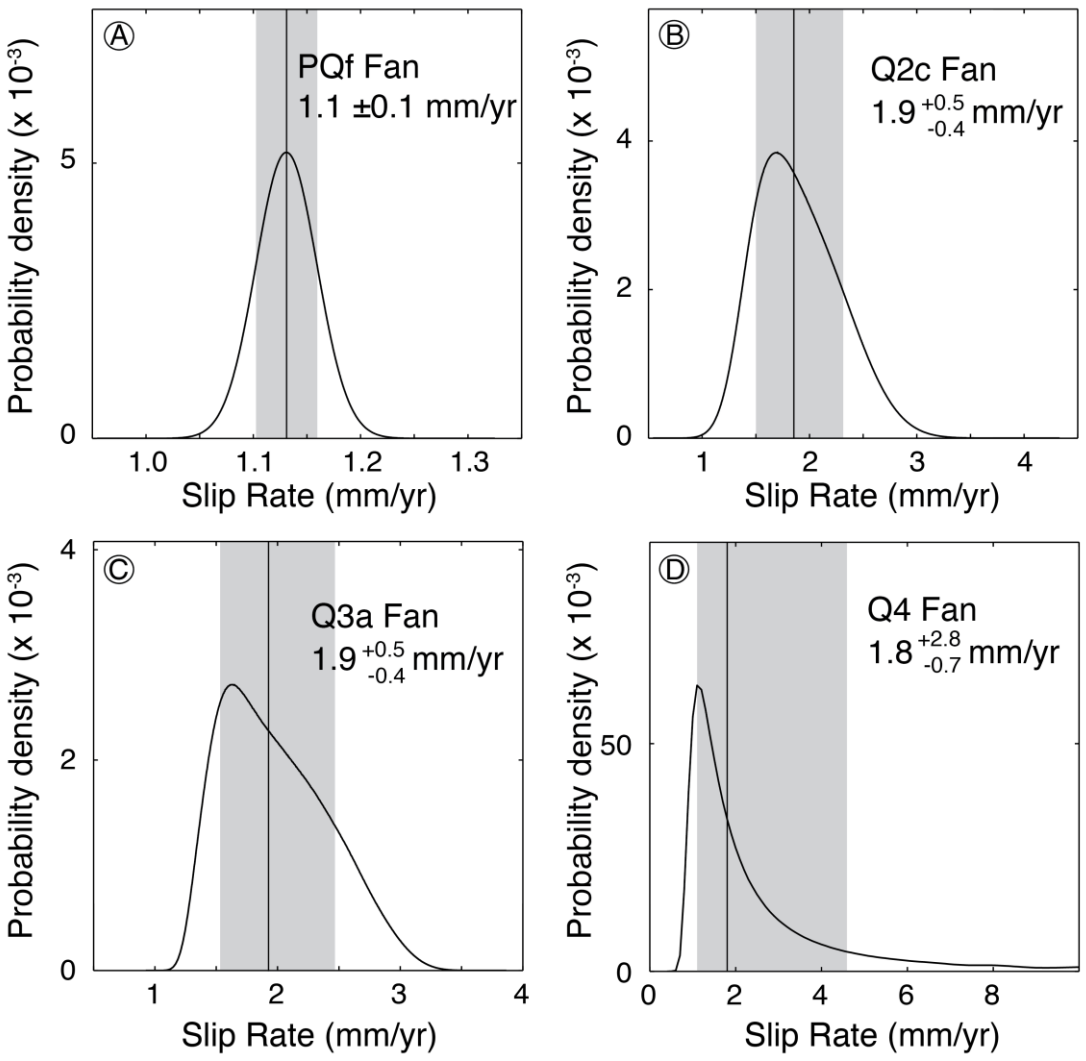

Figure 3.14. Slip rate probability density functions for offset PQf (a), Q2c (b), Q3a (c), and Q4 (d) alluvial fans. Uncertainties are reported at the 1σ level. Vertical line represents the median age and gray box represents the 1σ uncertainty interval.

Table 3.4. Offset, age, and slip rate for displaced alluvial fans.

Alluvial Fan Deposit	Magnitude of Offset [m]	Direction of Slip [degrees]	Age [ka]	Calculated Minimum Slip Rate [mm/yr]	Slip Rate Toward 323° [mm/yr][#]
PQf	854 ±20*	350	755 ±7	1.1 ±0.1	1.0 ±0.1
Q2c	175 ±20*	350	70-115	1.9 +0.5/-0.4	1.7 +0.4/-0.3
Q3a	73.3 ±3.0*	350	38.4 ±9.0	1.9 +0.5/-0.4	1.7 +0.4/-0.3
Q4	11.3 ±1.0	350	6.2 ±3.8	1.8 +2.8/-0.7	1.6 +2.5/-0.6

* Minimum offset magnitude due to lack of offset markers on all mapped fault strands.

[#] Slip rate calculated parallel to Pacific-North America plate motion (Dixon et al., 2000).

3.6 DISCUSSION

We document four right-lateral slip rates spanning the middle Pleistocene through the Holocene that suggest remarkably constant strain release on the WMFZ. The slip rates presented here are minima for two primary reasons: (1) displacement measurements are minima because offset markers were not observed on all strands of the fault, and therefore we cannot account for all the displacement across the WMFZ; and (2) fan exposure ages are maxima because we assume displacement of alluvial fans occurred shortly after deposition, but the duration of displacement may have been shorter. In some cases our slip rates are minima for a third reason: lateral fluvial erosion of channel walls erases the markers of true offset and the resulting displacement measurements are minima.

Our results have implications for long- vs. short-term slip rates across the Walker Lane. At ~36.5°N latitude, the sum of long-term geologic slip rates is the same, within error, to the short-term geodetic slip rates (cf. Bennett et al., 2003; Lee et al., 2009a). In contrast, there has been a significant discrepancy observed in the southern Walker Lane at ~37.5°N latitude between long-term geologic slip rates and short-term geodetic slip rates. The sum of published late Pleistocene slip rates, projected toward the plate motion direction of 323°, across this part of the Walker Lane is 6.1 +1.0/-0.5 mm/yr (Figure 3.15, Table 3.1) (Kirby et al., 2006; Frankel et al., 2011; Reheis and Sawyer, 1997; Foy et al., 2012; Hoeft and Frankel, 2010). However, dislocation models constrained by GPS data predict a long-term slip rate at ~37.5°N latitude of 10.6 ± 0.5 mm/yr (Lifton et al., 2013). Many hypotheses have been invoked to explain this discrepancy, including transient strain (Frankel et al., 2011), postseismic relaxation following the 1872 M_w7.6 Owens

Valley earthquake (Hammond et al., 2009; Dixon et al., 2003), or distributed strain across the region (Frankel et al., 2011; Foy et al., 2012; Nagorsen-Rinke, 2013). Including our new ~38 ka slip rate estimate for the WMFZ in a summation of plate motion-parallel slip (toward 323°) across this part of the Walker Lane yields a total of 7.5 +1.1/-0.6 mm/yr (Figure 3.15, Table 3.1).

We consider several hypotheses to account for the remaining difference between long- and short-term slip rates. First, some proportion of strain may be accommodated off of primary faults in a distributed fashion. This may result in deformation that is unrecognized because it is too small to rupture the surface or because small surface ruptures that occur in unconsolidated basin fill are not preserved in the landscape. Distributed deformation has been proposed as a possible source of uncertainty in geologic slip rates (e.g. Foy et al., 2012), and has potential to account for significant strain. We observed evidence of displacement on other fault strands in the WMFZ that we were unable to quantify due to a lack of offset markers. Since our slip rates, and those published by others, are minima, the long- and short-term discrepancy could potentially be resolved by accounting for strain that we are currently unable to quantify. Distributed deformation is extremely difficult to quantify, but future applications of high resolution LiDAR data may provide a means to estimate the proportion of strain occurring off faults.

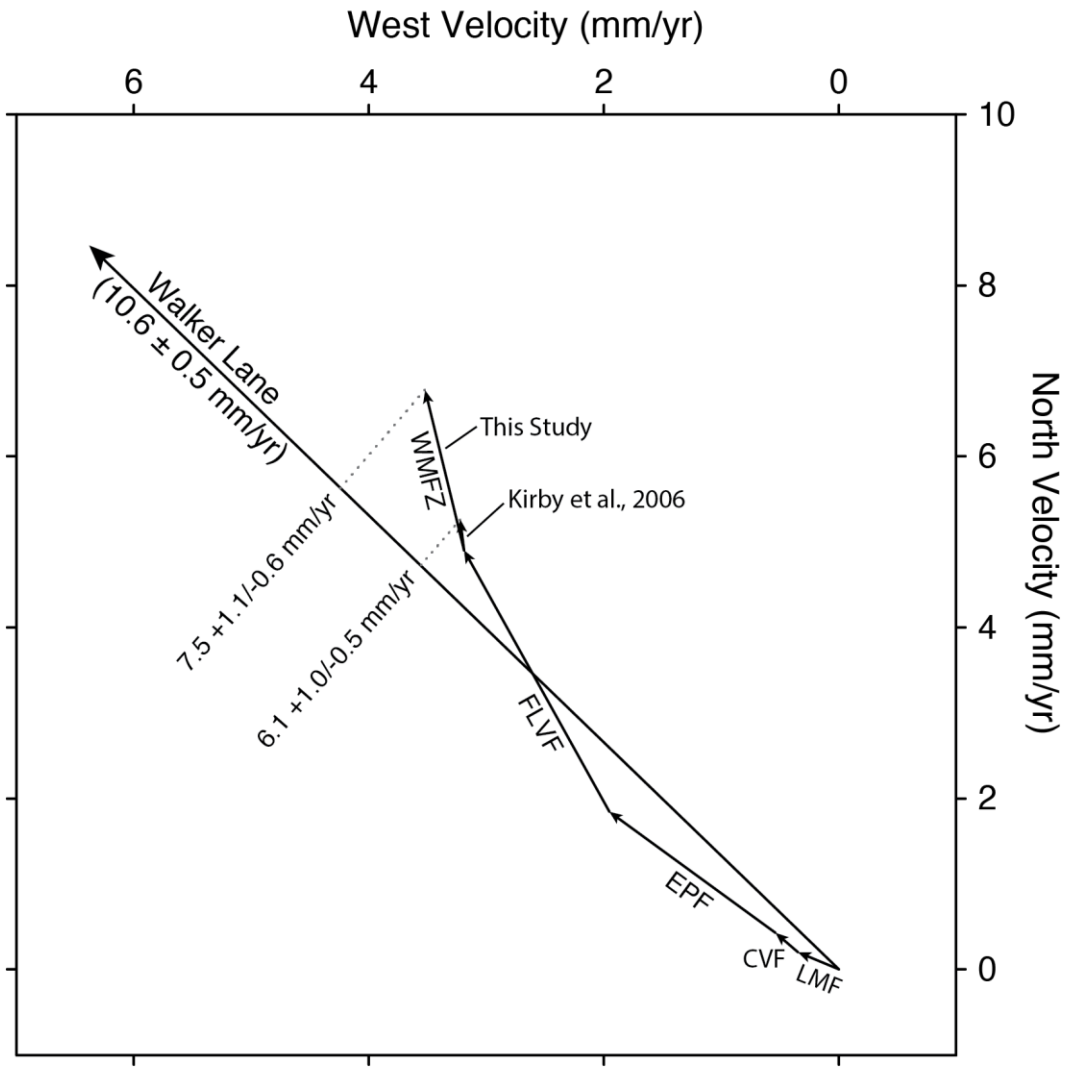

Figure 3.15. Velocity diagram of the Walker Lane at ~37.5°N. The long line (10.6 ± 0.5 mm/yr) is the short-term, far-field velocity determined by GPS toward 323° (Lifton et al., 2013). Individual long-term fault contributions are summed and compared to the short-term rate. See Table 3.1 for additional information.

Second, slip may be accommodated within Owens Valley and further west across the Fish Slough fault, the Volcanic Tableland, and Round Valley fault (e.g. Nagorsen-Rinke et al., 2013). This westward routing would allow for transfer of slip from the Owens Valley fault into the Adobe Hills, located in the southwestern part of the Mina Deflection (Nagorsen-Rinke et al., 2013). While right-lateral slip rates are not well documented on these faults, there is evidence to suggest they may be accommodating right-lateral displacement. The 1986 M6.2 Chalfant earthquake and 1986 M5.2 White Mountains earthquake caused minor right-lateral surface fractures, and the seismicity and fault plane surface projection trend NNW from the White Mountains range front toward the Volcanic Tableland (Lienkaemper et al., 1987; dePolo, 1989; Stockli et al., 2003). Bateman (1965) suggested that the en echelon geometry of faults across the Volcanic Tableland and adjacent broad folds were the result of right-lateral shear. In addition, Nagorsen-Rinke et al. (2013) made two important observations: (a) most of the normal faults across the Volcanic Tableland strike clockwise with respect to the relative motion between the Sierra Nevada and North America, thus defining releasing steps in a right-lateral slip system, and (b) some of the normal faults curve into parallelism with Sierra Nevada and North America relative motion implying they record a right-lateral component of slip. Phillips and Majkowski (2011) documented right-lateral displacement along the Round Valley fault, which was previously considered to accommodate only normal dip-slip displacement. Geodetic measurements suggest that several mm/yr of right-lateral deformation is being accommodated between the White Mountains and the

Sierra Nevada range (Dixon et al., 2000; Phillips and Majkowski, 2011; Lifton et al., 2013)

A third hypothesis to explain the slip discrepancy is that slip is transferred to the NE of the White Mountains into the SPLM (e.g. Frankel et al., 2011). Extension on the SPLM normal faults is approximately parallel to the direction of shear in the Walker Lane. The SPLM may act as an extensional step-over (e.g. Oldow et al., 1994; Dixon et al., 1995; Reheis and Dixon, 1996), in much the same way as Queen Valley fault (Lee et al., 2009a), Deep Springs fault (Lee et al., 2001b), and Tin Mountain fault. The SPLM provides a potential route for strain to transfer from the southern Walker Lane to the central Walker Lane while bypassing the Mina Deflection. Evidence of distributed deformation across the SPLM (e.g. Foy et al., 2012) suggests that the extensional zone might be accommodating more strain than is documented. Furthermore, there is evidence for accelerating extension across the SPLM (Reheis and Sawyer, 1997; Hoeft and Frankel, 2010; Lifton et al., in prep.), implying that this region may be an important region for accommodating strain in the southern Walker Lane.

Our results also suggest that slip rates on the WMFZ have remained nearly constant since at least the late Pleistocene, and perhaps since the middle Pleistocene. The Q4, Q3a, and Q2c fan surface slip rates are the same within uncertainty, suggesting that the slip rate on the WMFZ has not changed over the last 100 ky. The PQf fan surface slip rate is slower, but is constrained by a reworked layer of Bishop tephra. The fact that the tephra has been reworked from its original deposit allows for the possibility that PQf fan displacement could be younger than 755 ka and thus the slip rate could be faster than 1.1 ± 0.1 mm/yr. Regardless of the slip rate since deposition of the Bishop tephra, the WMFZ

shows remarkably constant slip rates since ~100 ka, in contrast to previous hypotheses that slip rates have been variable on the WMFZ during the Pleistocene (e.g. Kirby et al., 2006). Kirby et al. (2006) used the Bishop tephra to constrain a middle Pleistocene right-lateral slip rate of 0.7-0.8 mm/yr, but found that the late Pleistocene (from 22.5 ± 1.5 ka) right-lateral slip rate was significantly slower at 0.3-0.4 mm/yr. That study suggested that a major change in the local stress field sometime before ~70 ka caused slip rates on the WMFZ to slow dramatically. Our results contradict those of Kirby et al. (2006) and suggest that either slip rates on the WMFZ have remained constant since the middle Pleistocene, or that slip rates have varied on time scales shorter than the ~70 k.y. hypothesized by Kirby et al. (2006). Given the strikingly constant slip rates over the last ~755 k.y., we believe that slip at these locations on the WMFZ has indeed remained constant.

3.7 CONCLUSIONS

We present new geologic mapping, high-resolution LiDAR data, $^{40}Ar/^{39}Ar$ dates, and ^{10}Be TCN exposure dates to estimate four right-lateral slip rates on the WMFZ over a wide range of time scales spanning middle Pleistocene to Holocene. Alluvial fans with ages of >755 ± 7 ka, ~70-115 ka, 38.4 ± 9.0 ka, and 6.2 ± 3.8 ka have been right-laterally displaced by a minimum of 854 ± 20 m, 175 ± 20 m, 73 ± 3 m, 11 ± 1 m, respectively, yielding minimum geologic slip rates of 1.1 ± 0.1 mm/yr, 1.9 +0.5/-0.4 mm/yr, 1.9 + 0.5/-0.4 mm/yr, and 1.8 +2.8/-0.7 mm/yr. These results have implications for the constancy of slip and long- vs. short-term strain accommodation. Our results suggest that slip rates on the WMFZ have remained nearly constant from the middle Pleistocene

through the Holocene. These new slip rates, when added to previously published rates across the southern Walker Lane, sum to 7.5 +1.1/-0.6 mm/yr of slip directed toward 323°. This accounts for 70-80% of the observed geodetic slip rate of 10.6 ± 0.5 mm/yr (Lifton et al., 2013). We hypothesize that the remaining "missing" slip may be accommodated: (1) in a distributed fashion along the major right-lateral faults in this part of the Walker Lane; (2) to the west of the WMFZ in the Volcanic Tableland and Sierra Nevada frontal faults; and/or (3) to the east of the FLVF via accelerating extension of the SPLM.

CHAPTER 4

LATEST PLEISTOCENE AND HOLOCENE EXTENSION RATES ON THE LONE MOUNTAIN FAULT: EVIDENCE FOR ACCELERATING SLIP IN THE SILVER PEAK-LONE MOUNTAIN EXTENSIONAL COMPLEX

4.1 ABSTRACT

The Silver Peak-Lone Mountain extensional complex (SPLM) is a zone dominated by down-to-the-northwest normal faults, including the Emigrant Peak, Clayton Valley, and Lone Mountain faults, that accommodates strain within the southern Walker Lane. We combine detailed field geomorphologic mapping, topographic surveying, and ^{10}Be cosmogenic nuclide exposure ages to calculate new late Pleistocene and Holocene extension rates on the Lone Mountain fault. Alluvial fans with ages of 14.6 ± 1.0 ka and 8.0 ± 0.5 ka were horizontally displaced 12.2 m and 5.6 m, respectively, yielding slip rates of 0.8 ± 0.1 mm/yr and 0.7 ± 0.1 mm/yr. These slip rates are significantly faster than rates from earlier in the Pleistocene, defining a pattern of accelerating slip on the Lone Mountain fault. We hypothesize that the modern SPLM is a kinematic link between the southern and central Walker Lane, transferring slip between the Fish Lake Valley fault and the Benton Springs and Petrified Springs faults. The possibility of accelerating extension rates across the SPLM helps reconcile the observed discrepancy between long- and short-term slip rates in this region.

4.2 INTRODUCTION

The Pacific-North American plate boundary accommodates ~51 mm/yr of relative motion across a wide zone along the southwestern margin of North America (DeMets et al., 2010). Approximately 20% of that motion is accommodated in the Walker Lane, a diffuse, ~50-100-km-wide right lateral shear zone (Fig. 4.1; Dixon et al., 2000; Wesnousky, 2005; Lifton et al., 2013). Strain is transferred through the Walker Lane primarily through north-northwest striking right-lateral strike-slip faults, such as the Death Valley fault, Fish Lake Valley fault, Owens Valley fault, and White Mountains fault zone. Strain is transferred between these subparallel strike-slip faults by northeast striking extensional step-overs faults, such as Tin Mountain fault, Deep Springs fault (Fig. 4.1; Lee et al., 2001) Queen Valley fault (Lee et al., 2009) (Oldow et al., 1994; Dixon et al., 1995; Reheis and Dixon, 1996).

Oldow et al. (1994, 2009) proposed that the Silver Peak-Lone Mountain extensional complex (SPLM) is one such extensional step-over, transferring strain from the Fish Lake Valley Fault to the Benton Springs and Petrified Springs fault zones in the central Walker Lane to the northeast (Fig. 4.1). Similarly, Frankel et al. (2007) and Frankel et al. (2011) proposed that the northward decrease in slip rate on the Fish Lake Valley fault is the result of distributed strain across the SPLM. The SPLM consists of a series of northeast trending normal faults, including Emigrant Peak, Clayton Valley, and Lone Mountain faults, which all have Quaternary displacements (Fig. 4.1). Reheis and Sawyer (1997) report the vertical slip rate on the Emigrant Peak fault since ~6.5 ka to be 3.4 +1.8/-0.9 mm/yr, which we convert to a horizontal rate of 2.0 +0.7/-0.5 mm/yr toward 315°, assuming a fault dip of 60°. Foy et al. (2012) report a horizontal extension rate on

the Clayton Valley since ~17 ka to be 0.1-0.3 mm/yr toward 320°. Hoeft and Frankel (2010) report horizontal extension rates across the Lone Mountain fault to be 0.1-0.4 mm/yr toward 300° since ~17 ka. We evaluate these extension rates along the SPLM relative to the local plate motion direction (323°**)**, to understand their contribution to the overall plate boundary strain field. The sum of extension directed toward 323° across the SPLM is 2.6 +0.7/-0.5 mm/yr.

Using geologic and geomorphologic mapping and terrestrial cosmogenic nuclide (TCN) geochronology Hoeft and Frankel (2010) were able to suggest that extension rates on the Lone Mountain fault had increased between 92 ka and 17 ka. We test the hypothesis that extension rates on the Lone Mountain fault continued to increase from latest Pleistocene through the Holocene, and that the SPLM may be accommodating a larger portion of plate boundary deformation than previously known. We calculated extension rates by combining measurements of extension with ^{10}Be TCN exposure ages from two displaced alluvial fan surfaces.

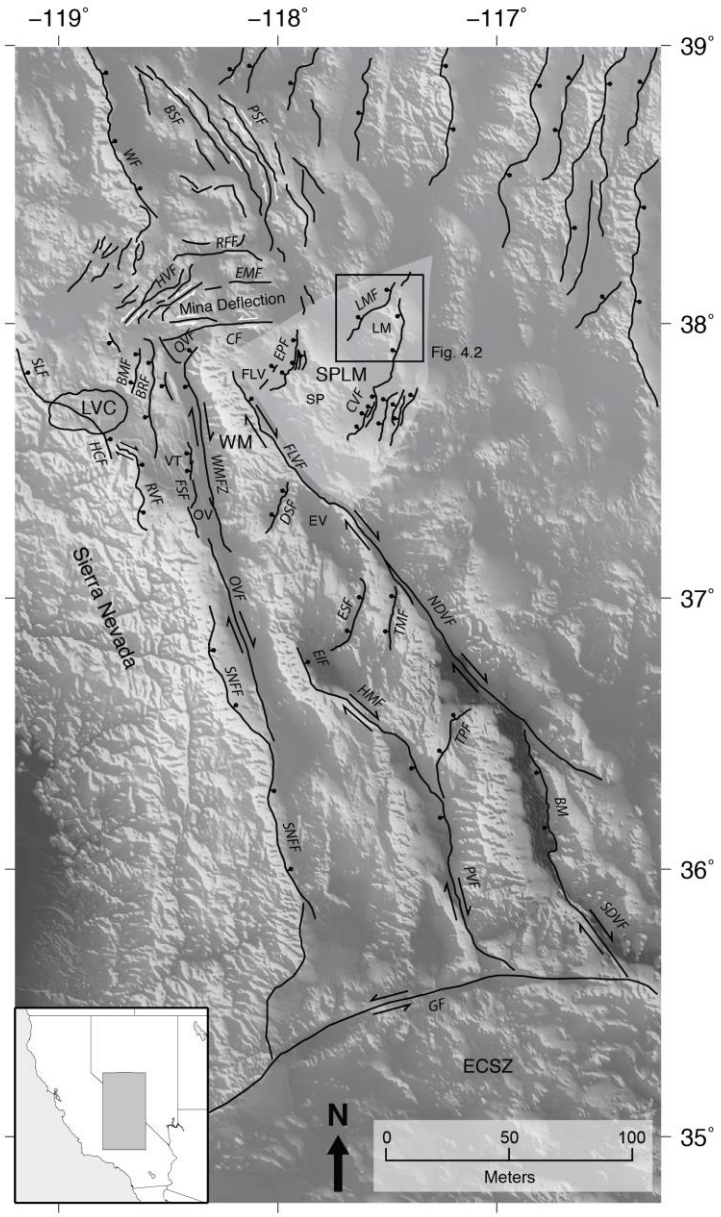

Figure 4.1. Shaded relief map of the southern Walker Lane showing simplified major faults. Light gray shaded region is the Silver Peak-Lone Mountain extensional complex. BMF – Black Mountain fault; BM – Black Mountain fault (Death Valley); BRF – Benton Range fault; BSF – Benton Springs fault; CF – Coaldale fault; CVF – Clayton Valley fault; DSF – Deep Springs fault; ECSZ – Eastern California Shear Zone; EIF – Eastern Inyo fault; EMF – Excelsior Mountains fault; EPF – Emigrant Peak fault; ESF – Eureka-Saline fault; EV – Eureka Valley; FSF – Fish Slough fault; FLV – Fish Lake Valley; FLVF – Fish Lake Valley fault; GF – Garlock fault; HCF – Hilton Creek fault; HMF – Hunter Mountain fault; HVF – Huntoon Valley fault; LM – Lone Mountain; LMF – Lone Mountain fault; LVC – Long Valley Caldera; NDVF – Northern Death Valley fault; OV – Owens Valley; OVF – Owens Valley fault; PSF – Petrified Springs fault; PVF – Panamint Valley fault; QVF – Queen Valley fault; RFF – Rattlesnake Flat fault; RVF – Round Valley fault; SDVF – Southern Death Valley fault; SLF – Silver Lake fault; SNFF – Sierra Nevada frontal fault; SP – Silver Peak Range; SPLM – Silver Peak-Lone Mountain extensional complex; TMF – Tin Mountain fault; TPF – Towne Pass fault; VT – Volcanic Tableland; WM – White Mountains; WMFZ – White Mountains fault zone; WF – Wassuk Range fault.

4.2.1 Tectonic and Geologic Setting

The SPLM is bounded on the west by the Fish Lake Valley fault, on the south by the Sylvania Mountains and the Montezuma Range, and on the north by the Candelaria Hills and Monte Cristo Range. The eastern boundary is not well defined, but lies east of Lone Mountain (Oldow et al., 2008).

Extension in the SPLM initiated at ~12-8 Ma as a northwest-dipping detachment and was active until ~3 Ma, when 20°-30° of clockwise vertical-axis rotation created long-wavelength (20-30 km), high amplitude (1-2 km) folds in the detachment, which eventually locked motion on the fault (Oldow, et al., 2008). The detachment is now exposed in the Silver Peak Range and at Lone Mountain, where it separates deformed amphibolite facies rocks in the lower plate from Cenozoic volcanics and Mesozoic intrusive rocks in the upper plate (Oldow et al., 2008). As the SPLM detachment shut down, the Mina deflection became the active slip transfer system connecting the southern and central Walker Lane (Oldow, et al., 2008).

Prominent Quaternary scarps are exposed on Emigrant Peak, Clayton Valley, and Lone Mountain faults. Reheis and Sawyer (1997) estimated vertical slip rates on the Emigrant Peak fault of 0.1-0.5 mm/yr during the late Pleistocene to 2.2-4.0 mm/yr during the Holocene. We convert their vertical rates to horizontal rates by assuming a fault dip of 60°, yielding 0.4 ± 0.1 mm/yr since 50-70 ka and 2.0 +0.7/-0.5 mm/yr since 6.5 ± 1.5 ka. The late Pleistocene horizontal extension rates on the Clayton Valley and Long Mountain faults were recently determined to be 0.1-0.3 mm/yr (Foy et al., 2012), and 0.1-0.4 mm/yr (Hoeft and Frankel, 2010), respectively.

The Lone Mountain fault is a northeast striking down-to-the-northwest normal fault that bounds the northwest side of Lone Mountain and the Weepah Hills (Fig. 4.2). Along its southwestern portion, the Lone Mountain fault cuts the low hills and broad alluvial piedmont of the Weepah Hills. The fault is expressed as scarps that progressively increase in height with age, ranging from ~1 m to ~17 m in height. Along its northeastern portion the fault delineates the bedrock-alluvium interface, offsetting young, steep alluvial fans and in some cases offsetting bedrock. To the northeast, the Lone Mountain fault diverges from the range front, offsetting alluvial fans and its surface expression dies out. Hoeft and Frankel (2010), Hoeft (2010), and Hoeft and Frankel (2012) mapped the southwest portion of Lone Mountain fault through the alluvial piedmont of the Weepah Hills and Lone Mountain range front, and estimated cosmogenic nuclide exposure ages for three alluvial fans displaced by the fault. We expand upon the work of Hoeft and Frankel (2010) by mapping part of the northeast portion of the Lone Mountain fault and estimating cosmogenic nuclide exposure ages on two alluvial fans displaced by the fault. This work not only expands the spatial extent of mapping of the Lone Mountain fault, but also extends the temporal range of fault slip rate estimates.

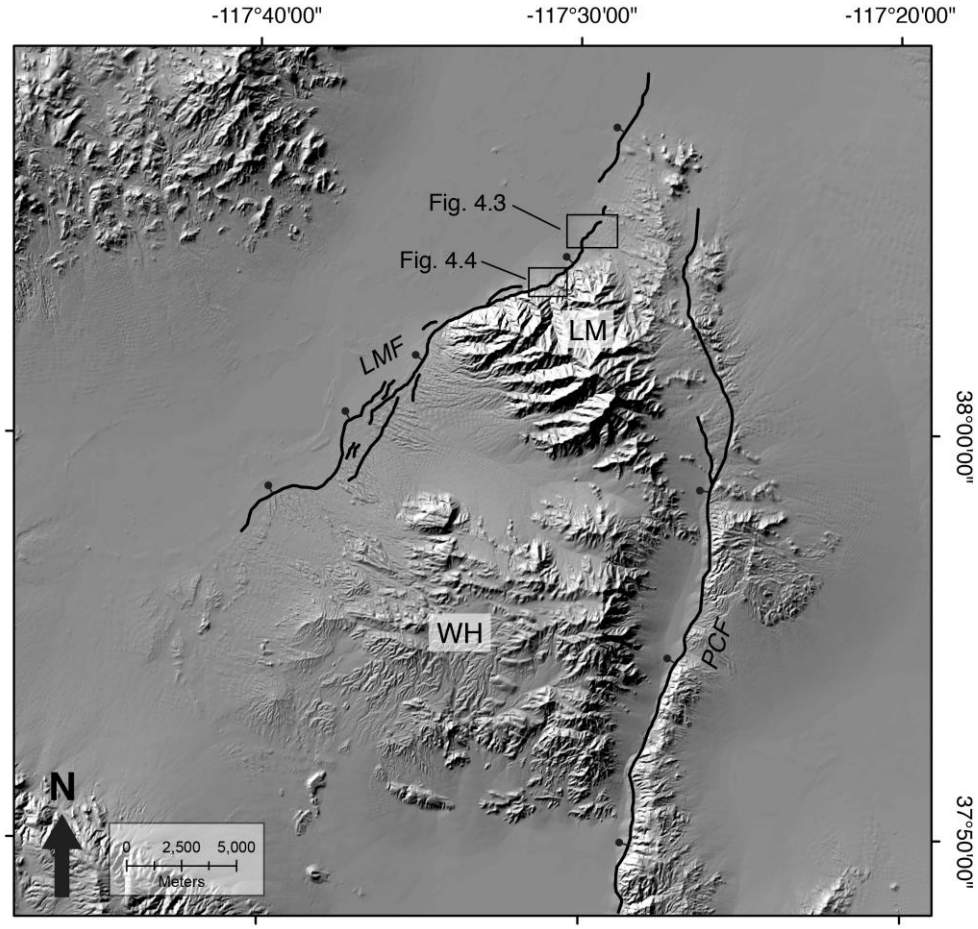

Figure 4.2. Shaded relief map of Lone Mountain (LM) and Weepah Hills (WH) showing the Lone Mountain fault (LMF) and locations of detailed alluvial fan maps. PCF – Paymaster Canyon fault.

4.3 ALLUVIAL FAN MAPPING

We mapped alluvial fan units and fault scarps at two sites along the Lone Mountain fault (Figs. 4.2, 4.3, and 4.4). Mapping was done on U.S. Department of Agriculture 1-m-resolution color orthorectified aerial photograph basemaps at scales of 1:5000 and 1:8000. Alluvial fan units were organized into the chronostratigraphic framework of Bull (1991), in which fan units are differentiated by criteria such as elevation above the active channel, extent of pavement and varnish development, bar and swale morphology, and degree of surface dissection. Below we describe the individual displaced alluvial fan units we mapped.

4.3.1 Descriptions of Alluvial Fan Units

4.3.1.1 Q3a Alluvial Fan

The Q3a alluvial fan is preserved in only a few locations in our mapping area, and we were not able to quantify its displacement. This fan has a subdued bar and swale morphology with vertical relief of the surface of less than 1 m. The surface is undissected and relatively planar. Desert pavement and desert varnish are moderately developed, giving the surface a darker color than the Q3b fan surface. The Q3a fan surface elevation is ~2-3 m above the active channel.

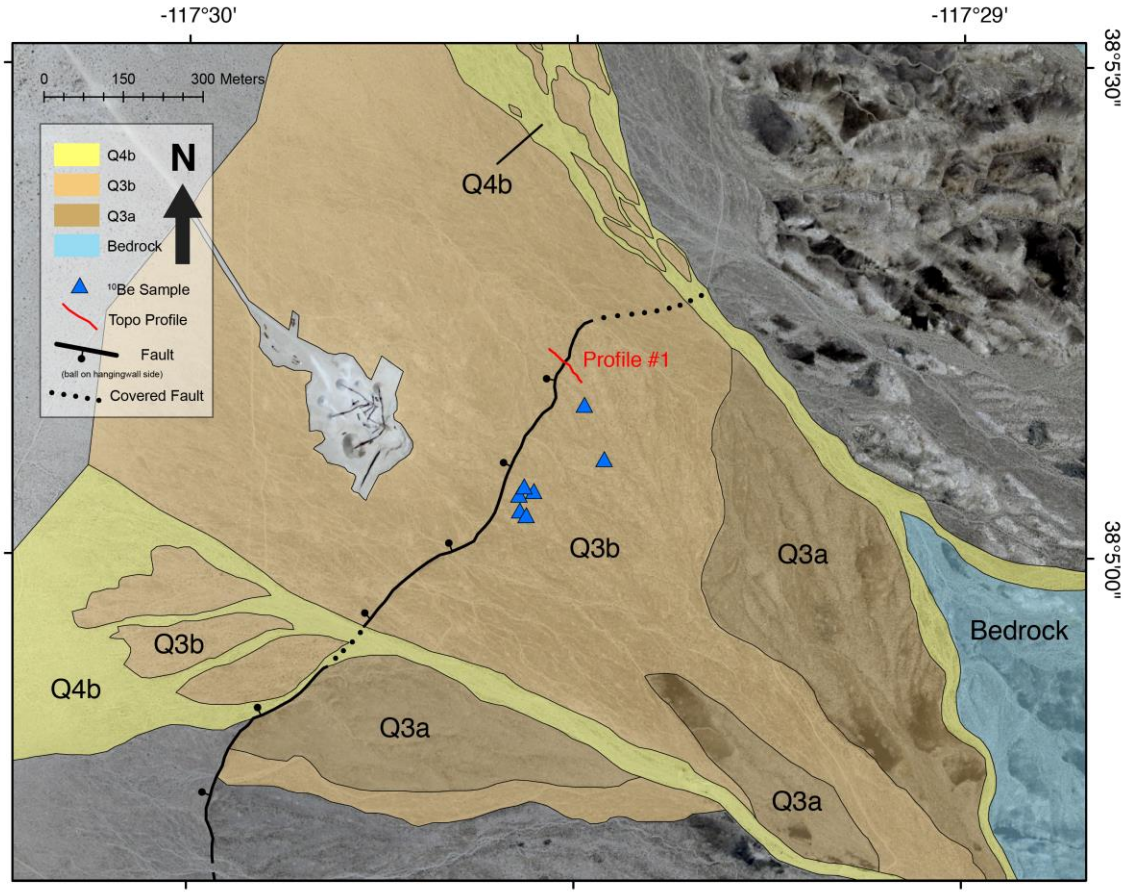

Figure 4.3. Surficial geologic map showing location of Q3b alluvial fan offset by Lone Mountain fault and sample locations (blue triangles). Red line is location of topographic profile across the fault scarp (Fig. 4.8a).

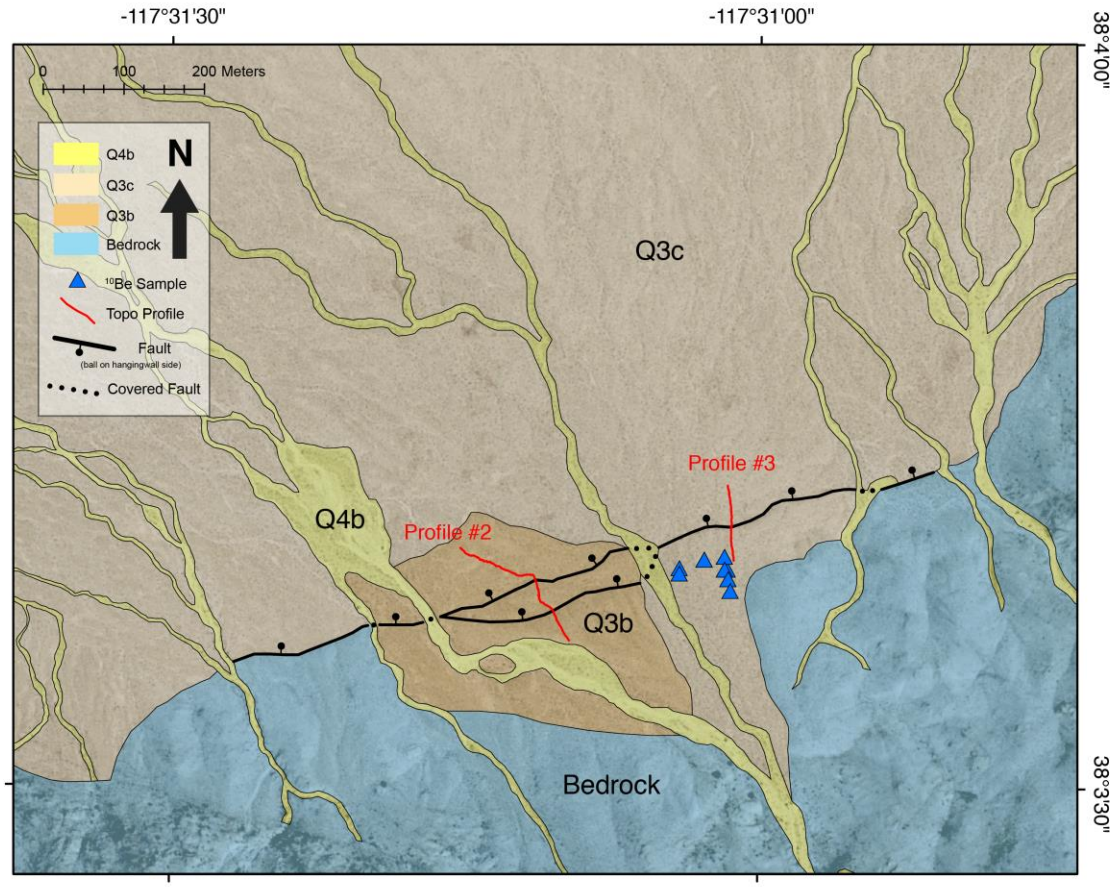

Figure 4.4. Surficial geologic map showing location of Q3b and Q3c alluvial fans offset by Lone Mountain fault and sample locations (blue triangles). Red lines are locations of topographic profiles across the fault scarp (Fig. 4.8b and 4.8c).

4.3.1.2 Q3b Alluvial Fan

The Q3b alluvial fan has subdued bar and swale morphology with vertical relief of less than 1 m. The surface has moderately developed pavement, with swale areas composed of a loosely interlocking pavement of gravel- and cobble-sized clasts with some sand and minor silt, and bar areas composed of cobble-sized clasts and rare boulder-sized clasts. The lithology of sediment is primarily granitic intrusive rock, which weathers to grus. Some clasts are moderately weathered. Boulders and cobbles have moderately developed varnish and rubification, and clasts on this surface and generally lightly weathered. The Q3b has a ~10-cm-thick Av horizon with some vesicles. The elevation of the Q3b surface is ~2 m above the active channel. Sparse vegetation is present on the surface, consisting of ~75 cm tall shrubs spaced ~2-3 m apart.

4.3.1.3 Q3c Alluvial Fan

The Q3c alluvial fan has prominent bouldery bar and swale morphology that is beginning to diffuse. The bar and swale morphology has a wavelength of ~3 m and amplitude of ~1-2 m. Desert pavement is poorly developed, and varnish and rubification is absent to moderately developed on boulders and cobbles. Sediment is primarily granitic intrusive rock. Some clasts are lightly to moderately weathered. The Q3c fan is more bouldery than the Q3b surface, which we attribute to it being closer to the source area. This fan has a poorly developed, non-vesicular Av horizon that is ~5 cm thick. Some portions of the fan have a well-developed biotic crust that appears darker than the rest of the fan surface. The elevation of the Q3c surface is ~1-2 m above the active channel.

4.3.1.4 Q4b Alluvial Fan

The Q4b alluvial fan unit is the most recently active stream channel. It is composed of boulders, cobbles, and gravel within channels incised into surrounding fans. Bar and swale morphology is prominent. Desert pavement and varnish are absent, and clasts are generally fresh and unweathered. Q4b deposits are lighter colored than older deposits.

4.4 COSMOGENIC NUCLIDE EXPOSURE AGES

We estimated fan surface exposure ages with ^{10}Be TCN dating. Boulders embedded in the alluvial fan surface are exposed to cosmic rays, which interact with Si and O atoms in minerals and produce ^{10}Be nuclides. The concentration of ^{10}Be nuclides is a function of exposure time, rock density, radioactive decay, erosion, and inheritance from previous exposure (Lal, 1991; Gosse and Phillips, 2001).

We sampled 7 boulders from the Q3b surface and 7 boulders from the Q3c surface (see Figs. 4.3 and 4.4 and Table 4.1 for locations). Samples were collected from the upper ≤5 cm of the top of each boulder. We sampled boulders that showed evidence of being in place and exposed at the surface since deposition. In particular, we chose boulders that were located on flat surfaces, away from the fan surface edges where diffusive processes can move sediment. We also chose boulders that were not weathered, that had desert varnish on the top of the boulder only, and that did not appear to be exhumed (Fig. 4.5). Since the fans are at the range front and the tributaries delivering sediment are very steep, boulders had short transport times and previous exposure and TCN production (inheritance) is minimized.

Each surface sample was prepared and measured separately following the methods of Kohl and Nishiizumi (1992). Samples were crushed, pulverized, and sieved to isolate the 250-500 μm size fraction. Quartz was isolated and purified with a series of HF leaches in heated ultrasonic tanks. After dissolution, Be was extracted from the quartz by ion exchange chromatography, then precipitated as $Be(OH)_2$ and oxidized to BeO. The BeO was mixed with niobium powder and packed in a target. The $^{10}Be/^{9}Be$ ratio of each sample was measured by accelerator mass spectrometry (AMS) at the Purdue Rare Isotope Measurement Lab (PRIME). Isotopic ratios were normalized to standard 07KNSTD3110 with a value of 2.85×10^{-12} (Nishiizumi et al., 2007). Results are reported in Table 4.1.

Exposure ages for each sample are modeled using the CRONUS-Earth age calculator (Balco et al., 2008), using a time-invariant sea level, high latitude ^{10}Be production rate of 4.76 atoms g^{-1} a^{-1}, scaled for our locations (Lal, 1991; Stone 2000; Nishiizumi et al., 2007). Ages and their associated uncertainties are combined in a probability density function (PDF) to determine the weighted mean exposure age and 1σ uncertainty for each fan.

The exposure ages of individual boulders fall into several distinct clusters. On the Q3b fan, two boulders are ~14 ka, one boulder is ~31 ka, and the remaining four boulders are ~45 ka. On the Q3c fan, three boulders are ~8 ka, three boulders are ~15 ka, and one boulder is ~45 ka (Fig. 4.6). The older exposure ages of some boulders reflect a more complex history of deposition and exposure in an older fan, remobilization and transport, and finally deposition and exposure in the current fan deposit. Because boulders can contain inherited ^{10}Be from previous exposure prior to deposition in their present

locations, we assume that the youngest clusters of ages are the best representation of the exposure age of the current alluvial fans. We calculated the weighted mean average of each cluster of ages (Fig. 4.6). The ^{10}Be exposure age of the Q3b fan is 14.6 ± 1.0 ka, and the ^{10}Be exposure age the Q3c fan is 8.0 ± 0.5 ka (Table 4.2). The Q3b fan age is the same, within uncertainty, as a nearby Q3b fan dated to 16.5 ± 1.2 ka by Hoeft and Frankel (2010). Our fan exposure ages also overlap with many other reported fan ages in the Walker Lane, eastern California shear zone, and Death Valley region (Fig. 4.7).

Figure 4.5. Photograph of a boulder sampled for ^{10}Be exposure dating. Criteria for selecting boulders include development of desert varnish and rubification, presence of interlocking desert pavement, and location away from channels or fan edges.

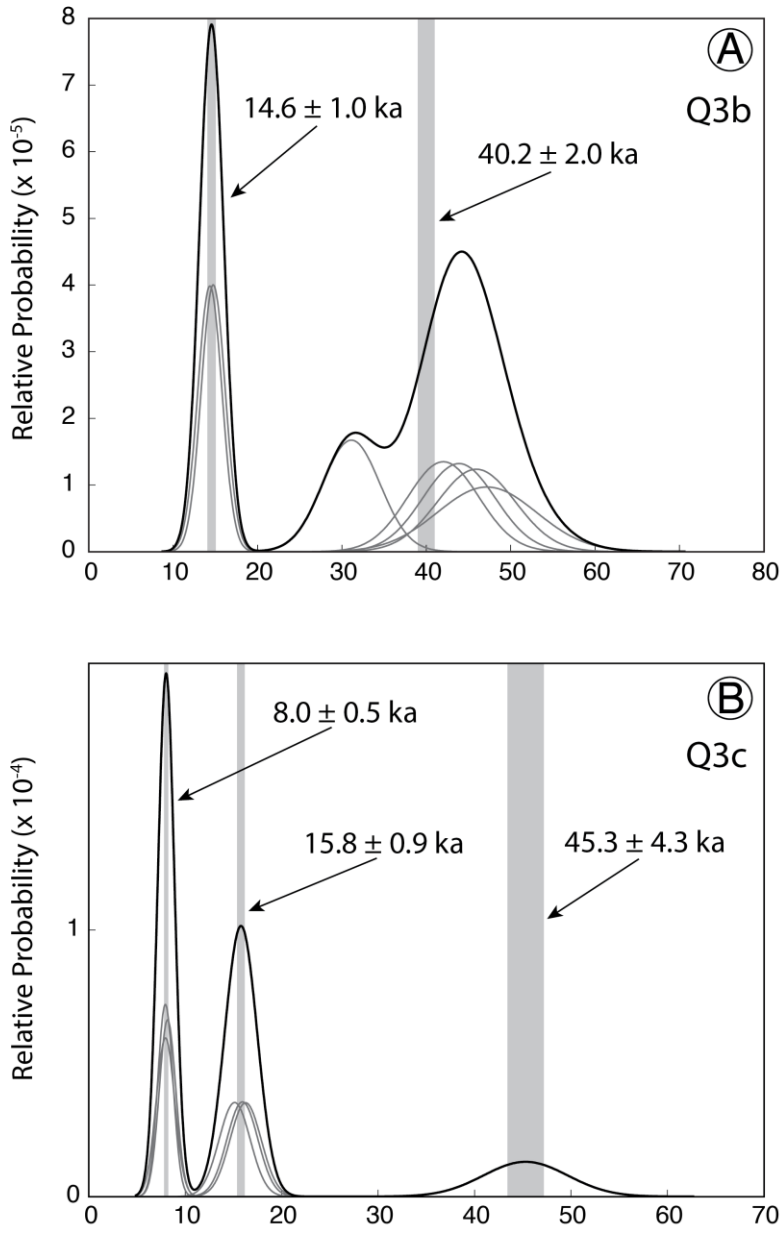

Figure 4.6. Probability density function (PDF) of ^{10}Be exposure ages from (a) 7 boulder samples on the Q3b fan surface, and (b) 7 boulder samples on the Q3c fan surface. Gray curves are individual PDFs for each boulder; black curve is the combined PDF for all ages. Vertical gray bands represent the 1σ uncertainty interval for the weighted mean ages of each peak. Note the consistency of age clusters between the two fans.

Table 4.1. ^{10}Be cosmogenic nuclide surface sample analytical data.

Sample	Lat. [°N]	Lon. [°E]	Elev. [m]	Thickness [cm]	Surface Orientation [strike/dip]	Shielding Factor	Quartz [g]	Be carrier mass [g]	Be carrier concentration [ppm]	^{10}Be concentration[a,d] [atoms/g]	^{10}Be concentration error[b] [atoms/g]	1σ total measured error[c] [%]	Exposure Age [years]
(Q3b)													
LM-11-01	38.08444	-117.49255	1506	5	FLAT	1	99.4925	0.2939	1354	188109.1838	5848.76673	0.039896586	14360 ± 1403
LM-11-02	38.08438	-117.49287	1500	5	FLAT	1	98.3538	0.3025	1354	404238.7087	18648.49673	0.052470917	31123 ± 3407
LM-11-03	38.08411	-117.49285	1503	4	FLAT	1	96.5584	0.3042	1354	616816.0755	38064.9145	0.066583505	47189 ± 5880
LM-11-04	38.08403	-117.49271	1503	5	FLAT	1	98.4600	0.3049	1354	569308.9521	17621.11109	0.039787072	43877 ± 4315
LM-11-05	38.08452	-117.49276	1502	5	FLAT	1	98.9399	0.3046	1354	595268.6695	20199.64261	0.042148464	45934 ± 4611
LM-11-06	38.08499	-117.49104	1507	1	055°/28°SE	0.981741998	80.8498	0.3065	1354	555259.6215	19091.22379	0.042510675	42018 ± 4227
LM-11-07	38.08591	-117.49147	1501	5	FLAT	1	90.8915	0.3060	1354	192614.5093	5603.800818	0.03835913	14758 ± 1424
GT-13-07	--	--	--	--	--	--	BLANK	0.3068	1354	82423.4125	27538.06897	--	--
(Q3c)													
LM-11-08	38.06078	-117.51710	1586	5	FLAT	0.995525174	81.9866	0.3063	1354	219865.0538	7798.731051	0.043395378	15939 ± 1605
LM-11-09	38.06092	-117.51714	1586	5	FLAT	0.995525174	66.6993	0.3069	1354	208798.1616	9064.140876	0.050095075	15133 ± 1616
LM-11-10	38.06078	-117.51714	1586	6	FLAT	0.995525174	75.4351	0.3072	1354	615220.7778	17182.685	0.03748394	45295 ± 4372
LM-11-11	38.06067	-117.51709	1584	3	FLAT	0.995525174	84.0206	0.3028	1354	111694.0427	6552.010359	0.063765471	7961 ± 958
LM-11-12	38.06054	-117.51706	1587	5	FLAT	0.995525174	79.2563	0.3016	1354	224548.1402	7569.727704	0.041969359	16268 ±1619
LM-11-13	38.06089	-117.51743	1580	5	FLAT	0.995525174	69.3445	0.3036	1354	112579.8274	4683.592858	0.048536183	8180 ± 860
LM-11-14	38.06089	-117.51743	1580	5	FLAT	0.995525174	72.2514	0.3046	1354	109414.468	3716.982471	0.042179003	7950 ± 791
GT13-08	--	--	--	--	--	--	BLANK	0.3034	1354	0	16479.79531	--	--

[a] Isotopic ratios were normalized to standard 07KNSTD3110 with a value of 2.85 x 10^{-12} (*Nishiizumi et al.*, 2007).

[b] Uncertainties reported at 1σ confidence level.

[c] Total measured error includes a 2.5% 1σ error in sample preparation added in quadrature to the 1σ AMS error (e.g. *Hidy et al.*, 2010; *Gosse and Phillips*, 2001).

[d] Corrected for background

4.5 HORIZONTAL DISPLACEMENT

We measured topographic profiles across fault scarps using a Trimble GeoXH handheld Global Positioning System (GPS) unit. Differential corrections were made in post processing with data from nearby Continuously Operating Reference Station (CORS) sites. Profiles are orthogonal to the fault where they cross the scarp and follow the fan surfaces along the apex-to-toe fall line. All of our profiles were measured where the original fan surface is preserved in both the footwall and hangingwall. Topographic profiles across the fault scarp are presented in Fig. 4.8. We fit linear regressions to the footwall and hangingwall surfaces and projected them to the scarp, then measured the vertical offset between the surfaces at the center of the scarp. We calculated extension with a range of possible fault dips, from 40° to 60° (Table 4.2). However, our preferred extension is calculated with a 40° dip because we observed a cross-sectional exposure of the main Lone Mountain fault dipping 40° (see also Hoeft and Frankel, 2010). The extension magnitudes and rates discussed below assume a dip of 40°. We measured vertical offset of the Q3b fan surface in two locations (Figs. 4.3, 4.4, and 4.8). The location at which we sampled the Q3b surface is vertically offset 2.4 ± 0.3 m, which corresponds to 2.9 ± 0.3 m of horizontal displacement (Figs. 4.3 and 4.8a). However, we measured a combined vertical offset of 10.2 ± 0.3 m across two closely spaced faults offsetting the Q3b fan, which corresponds to 12.2 ± 0.3 m of horizontal displacement, preserved in a correlative Q3b fan nearby (Figs. 4.4 and 4.8b). We are confident the two Q3b surfaces are the same and we use the maximum displacement to calculate the extension rate. The Q3c surface is vertically offset 4.7 ± 0.3 m, which corresponds to 5.6 ± 0.3 m of horizontal displacement (Figs. 4.4 and 4.8c). Uncertainties in vertical

displacement measurements are estimated from the precision of the differential corrected GPS positions in our topographic profiles.

The relatively small displacement of the Q3c fan raises the possibility that it records only a single fault rupture event. If that is the case, then any slip rate we calculate will be meaningless because the duration of time for our slip rate will not include a full earthquake cycle and the true long term slip rate is not known. However, based on historical data from similar normal faults in the Basin and Range and empirical scaling relationships, we believe the Q3c scarp may represent two or more rupture events. The 1983 M_s 7.3 Borah Peak earthquake produced a 34-km-long surface rupture, with a maximum vertical displacement of 2.7 m (Crone and Machette, 1984). This observation may represent a typical maximum vertical displacement on a Basin and Range normal fault of approximately the same length as the Lone Mountain fault. There is evidence for larger local maximum displacements, for example the largest historic vertical offset in the Basin and Range occurred during the 1915 M_s 7.6 Pleasant Valley earthquake, which produced a 60-km-long surface rupture with a maximum vertical displacement of 5.8 m (dePolo et al., 1991). However, this appears to be exceptional and the scaling relationship developed for normal faults by Wells and Coppersmith (1994) predicts a maximum displacement of <2 m for 30-km-long fault rupture.

Table 4.2. Offset, age, and extension rate for displaced alluvial fans.

Alluvial Fan Deposit	Vertical Offset [m]	Magnitude of Extension 40° Dip [m]	Magnitude of Extension 60° Dip [m]	Direction of Extension [degrees]	Age [ka]	Minimum Slip Rate 40° Dip [mm/yr]	Slip Rate Toward 323° [mm/yr][#]
Q3b	10.2 ± 0.3	12.2 ± 0.4	5.9 ± 0.2	340	14.6 ± 1.0	0.8 ± 0.1	0.8 ± 0.1
Q3c	4.7 ± 0.3	5.6 ± 0.4	2.7 ± 0.2	340	8.0 ± 0.5	0.7 ± 0.1	0.7 ± 0.1

[#] Slip rate calculated parallel to Pacific-North America plate motion (Dixon et al., 2000).

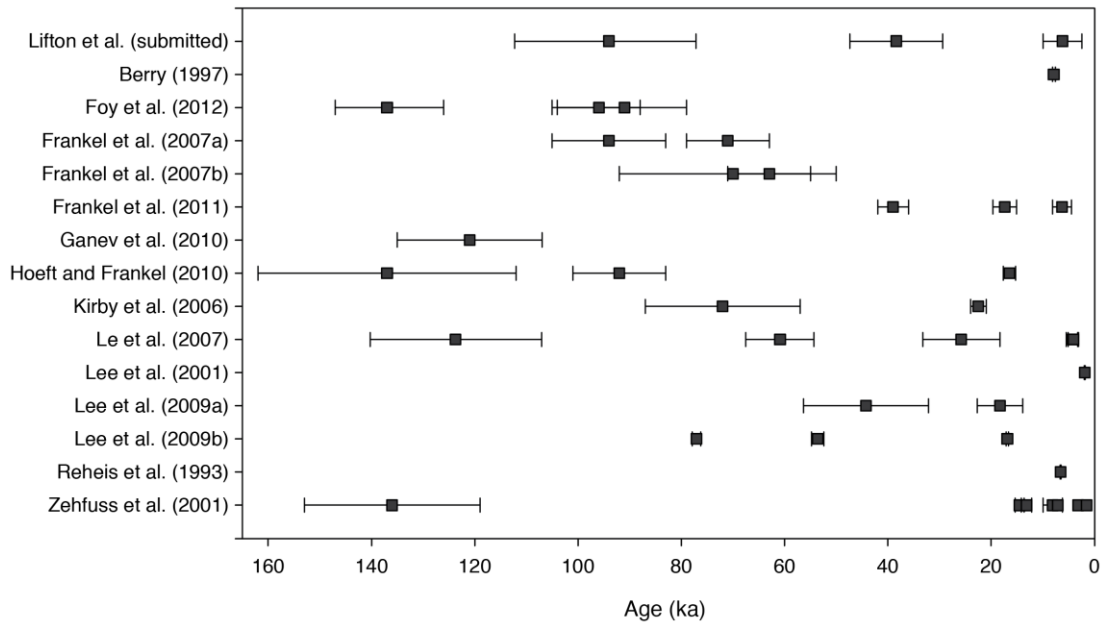

Figure 4.7. Compilation of published alluvial fan ages in the Walker Lane, eastern California shear zone, and Death Valley.

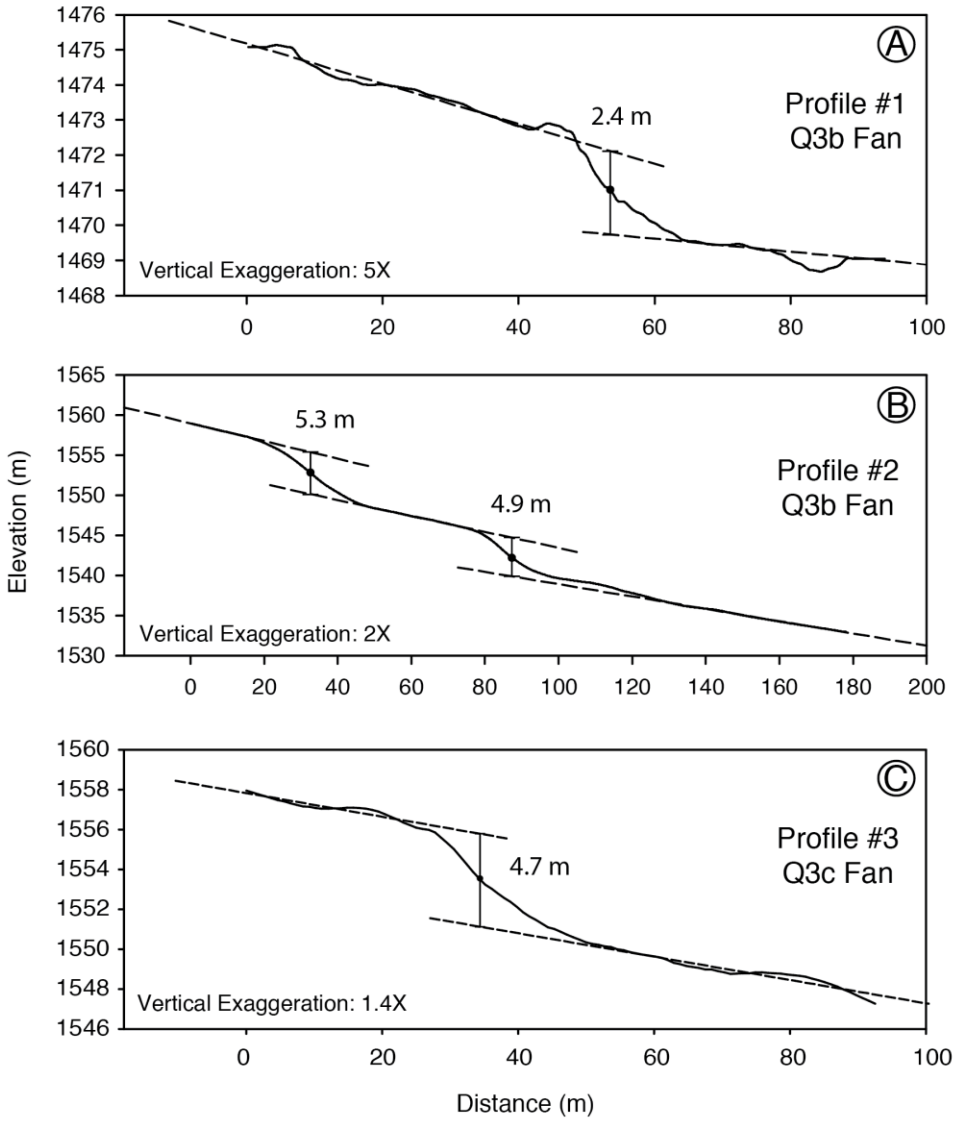

Figure 4.8. Topographic profiles across the Lone Mountain fault scarp in the (a) Q3b alluvial fan, (b) Q3b alluvial fan (double scarp), and (c) Q3c alluvial fan.

4.6 HORIZONTAL EXTENSION RATES

We used the methods of Zechar and Frankel (2009) to calculate extension rates. This probabilistic approach treats the displacement, age, and extension rate as probability density functions and propagates uncertainties of each measurement through the calculation of slip rate. All slip rates are reported with 1σ uncertainties. Combining the horizontal displacement of 12.2 ± 0.3 m with the exposure age of 14.6 ± 1.0 ka yields a horizontal extension rate of 0.8 ± 0.1 mm/yr for the the Q3b fan. Combining the horizontal displacement of 5.6 ± 0.3 m with the exposure age of 8.0 ± 0.5 ka yields a horizontal extension rate of 0.7 ± 0.1 mm/yr for the the Q3c fan (Fig. 4.9). These rates are minima because the fan exposure ages we use represent the earliest possible time that the fan was displaced, allowing for the possibility that the fans were displaced more recently.

4.7 DISCUSSION

Our results suggest that extension rates on the Lone Mountain fault were significantly faster during the latest Pleistocene and Holocene than during the period prior to ~17 ka. The extension rate since 14.6 ± 1.0 ka is 0.8 ± 0.1 mm/yr, and the extension rate since 8.0 ± 0.5 ka is 0.7 ± 0.1 mm/yr. These rates are significantly faster than the late Pleistocene slip rates on the Lone Mountain fault estimated by Hoeft and Frankel (2010) (0.1-0.4 mm/yr), but complement their conclusion that slip on the Lone Mountain fault is increasing (Fig. 4.10). The accelerating slip rates that we observe on the Lone Mountain fault also agree with the pattern of increasing slip rates observed elsewhere in the SPLM, in particular on the Emigrant Peak fault (Reheis and Sawyer, 1997). Reheis and Sawyer (1997) presented data that suggest the Emigrant Peak fault

horizontal extension rate was 0.4 ± 0.1 mm/yr since 50-70 ka, and then increased to 2.0 +0.7/-0.5 mm/yr since 6.5 ± 1.5 ka (extension rate estimates are our calculations from the original vertical slip rate data assuming a fault dip of 60°).

The possibility of accelerating extension across the SPLM has implications for the evolution of the Walker Lane. In particular, it is important for understanding how the Walker Lane accommodates strain, and for comparing long- and short-term slip rates across the Walker Lane. The SPLM transferred slip between the southern and central Walker Lane via a down-to-the-northwest detachment system from the Miocene to early Pliocene (Oldow et al., 2008). At ~3 Ma, this slip transfer configuration shut down and the Mina deflection began accommodating slip transfer between the southern and central Walker Lane via left-lateral slip and vertical-axis block rotation (Oldow et al., 2008; Wesnousky, 2005). Reactivation of this structural pathway suggests that extension in the SPLM is a fundamental mechanism for slip transfer between the southern and central Walker Lane.

Accelerating slip rates also have important implications for comparing long- and short-term slip rates across the Walker Lane. A discrepancy between long-term geologic slip rates and short-term geodetic slip rates has been observed across the Walker Lane at ~37°N latitude (Bennett et al., 2003; Kirby et al., 2006, 2008; Frankel et al 2007, 2011; Lifton et al., 2013). The sum of published late Pleistocene slip rates, projected toward the plate motion direction of 323°, across this part of the Walker Lane is 7.5 +1.1/-0.6 mm/yr (Lifton et al., in prep.). However, dislocation models constrained by GPS data predict a regionally averaged short-term right-lateral displacement rate at ~37.5N° latitude of 10.6 ± 0.5 mm/yr (Lifton et al., 2013). The possibility that the SPLM is accommodating an

increasing portion of shear zone-directed slip might help reconcile the discrepancy. If our new Holocene extension rate of 0.7 ± 0.1 mm/yr represents the Lone Mountain fault, the new sum of slip across the Walker Lane toward the plate motion direction of 323° is 7.8 +1.1/-0.6 mm/yr. This is still ~2.5 mm/yr slower than the geodetic slip rate of 10.6 ± 0.5 mm/yr (Lifton et al., 2013), however the results of Foy et al., (2012) suggest that significant strain is broadly distributed and that extension rates in the SPLM might be significantly faster than documented. Furthermore, the Holocene extension rate on the Clayton Valley fault is not known, but if it has experienced similar accelerated slip to the Emigrant Peak and Lone Mountain faults then its more recent extension rate may be significantly faster.

Our results, in combination with observations of slip occurring both east of the Fish Lake Valley fault (e.g. Reheis and Sawyer, 1997; Ganev et al., 2010; Foy et al., 2012; Hoeft and Frankel, 2010) and west of the White Mountains fault (Lienkaemper et al., 1987; dePolo and Ramelli, 1987; Phillips and Majkowski, 2011; Nagorsen-Rinke et al., 2013), support the hypothesis of Frankel et al. (2011) that the Walker Lane south of the Mina deflection is accommodating strain in a broader region than previously suspected. In other words, rather than strain being restricted to a narrow zone of right-lateral slip on the White Mountains and Fish Lake Valley faults (Reheis and Dixon, 1996), slip is diffused across a broader region as it moves northward toward the Mina deflection.

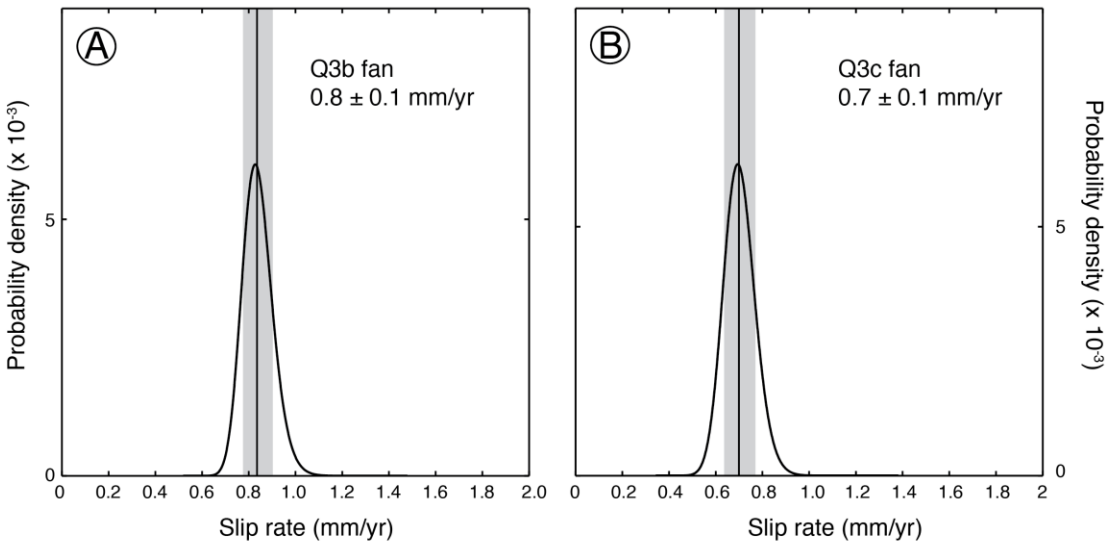

Figure 4.9. Extension rate probability density functions for offset Q3b (a) and Q3c (b) alluvial fans. Vertical line represents the median age and gray box represents the 1σ uncertainty interval.

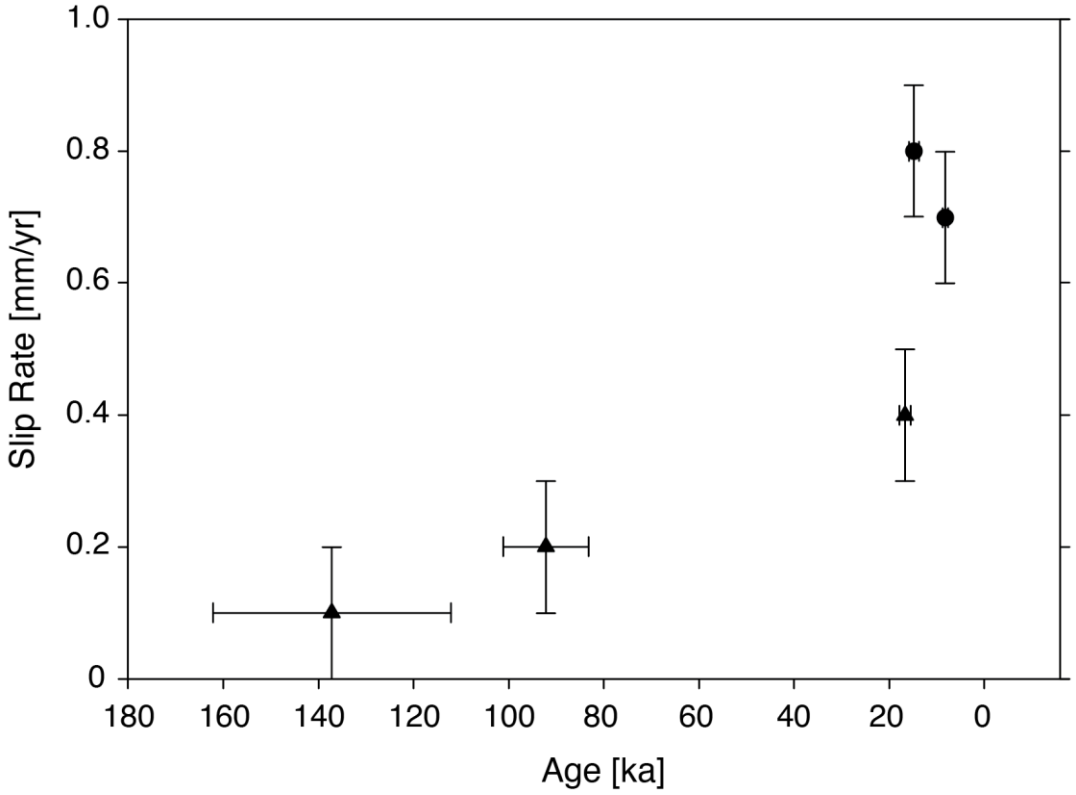

Figure 4.10. Compilation of extension rates on the Lone Mountain fault over time. Horizontal error bars represent reported age uncertainties; vertical error bars represent reported extension rate uncertainties. Circles are data from this study; triangles are data from Hoeft and Frankel (2010).

4.8 CONCLUSIONS

We estimate extension rates during the latest Pleistocene and Holocene on the Lone Mountain fault, which is a down-to-the-northwest normal fault in the Silver Peak-Lone Mountain extensional complex. Geologic mapping and topographic surveying yield horizontal displacements of 12.2 m and 5.6 m for the Q3b and Q3c fans, respectively. The extension rate since 14.6 ± 1.0 ka is 0.8 ± 0.1 mm/yr, and the extension rate since 8.0 ± 0.5 ka is 0.7 ± 0.1 mm/yr. These rates, in combination with previously published data (Hoeft and Frankel, 2010), suggest that extension on the Lone Mountain fault has accelerated during the late Pleistocene and Holocene (Fig. 4.10). We hypothesize that the modern SPLM is transferring slip to the central Walker Lane via normal faulting in a style similar to the pre-Mina deflection SPLM detachment system. Our results support Frankel et al.'s (2011) hypothesis that strain in the southern Walker Lane is distributed across a wider region than previously suspected as it moves northward toward the Mina deflection. The possibility of accelerating extension rates across the SPLM helps reconcile the observed discrepancy between long- and short-term slip rates in this region, especially if distributed deformation has resulted in undocumented displacement.

CHAPTER 5

CONCLUSIONS

In this work, I use GPS geodesy, geologic and geomorphologic mapping, high-resolution LiDAR geodetic imaging, and geochronology to estimate fault slip rates across the Walker Lane over a range of time scales. I present results that help elucidate the temporal and spatial distribution of strain accumulation and release across a diffuse, evolving plate boundary. I use these results to address the observed discrepancy between long- and short-term slip rates in the southern Walker Lane.

GPS results suggest: (1) that the southern Walker Lane at ~37.5°N accommodates 10.6 ± 0.5 mm/yr of right-lateral slip along the local plate motion direction of 323°, (2) the SPLM is currently undergoing ~2 mm/yr of extensional deformation toward 285°, and (3) Owens Valley accommodates ~2 mm/yr of contemporary right-lateral deformation, compared to the reported late Pleistocene slip rate of 0.4 mm/yr. I conclude that the observed discrepancy between contemporary geodetic and long-term geologic slip rates across the southern Walker Lane is occurring somewhere in Owens Valley. The discrepancy is likely a combination of underestimated geologic slip rates on the WMF and broadly distributed deformation in Owens Valley that is not well preserved in the geologic record.

Along the White Mountains fault zone alluvial fans with ages of >755 ± 7 ka, ~70-115 ka, 38.4 ± 9.0 ka, and 6.2 ± 3.8 ka have been right-laterally displaced by a minimum of 854 ± 20 m, 175 ± 20 m, 73 ± 3 m, 11 ± 1 m, respectively, yielding minimum geologic slip rates of 1.1 ± 0.1 mm/yr, 1.9 +0.5/-0.4 mm/yr, 1.9 + 0.5/-0.4

mm/yr, and 1.8 +2.8/-0.7 mm/yr. These results suggest that slip rates on the WMFZ have remained nearly constant from the middle Pleistocene through the Holocene. These new slip rates, when added to previously published rates across the southern Walker Lane, sum to 7.5 +1.1/-0.6 mm/yr of slip directed toward 323°. This accounts for 70-80% of the observed geodetic slip rate of 10.6 ± 0.5 mm/yr (Lifton et al., 2013). The remaining "missing" slip may be accommodated: (1) in a distributed fashion along the major right-lateral faults in this part of the Walker Lane; (2) to the west of the WMFZ in the Volcanic Tableland and Sierra Nevada frontal faults; and/or (3) to the east of the Fish Lake Valley fault via accelerating extension of the SPLM.

Finally, I estimate extension rates during the latest Pleistocene and Holocene on the Lone Mountain fault, which is a down-to-the-northwest normal fault in the Silver Peak-Lone Mountain extensional complex. Geologic mapping and topographic surveying yield horizontal displacements of 12.2 m and 5.6 m for the Q3b and Q3c fans, respectively. The extension rate since 14.6 ± 1.0 ka is 0.8 ± 0.1 mm/yr, and the extension rate since 8.0 ± 0.5 ka is 0.7 ± 0.1 mm/yr. These extension rates, in combination with previously published extension rates (Hoeft and Frankel, 2010), suggest that extension on the Lone Mountain fault has accelerated during the late Pleistocene and Holocene (Figure 4.8). I hypothesize that the modern SPLM may be transferring slip to the central Walker Lane via normal faulting in a style similar to the pre-Mina deflection SPLM detachment system. My results support Frankel et al.'s (2011) hypothesis that strain in the southern Walker Lane is distributed across a wider region than previously suspected as it moves northward toward the Mina deflection. Faster extension rates across the SPLM helps to

reconcile the observed discrepancy between long- and short-term slip rates in this region, especially if distributed deformation has resulted in undocumented displacement.

Taken together, my results suggest that at ~37.5°N the Walker Lane accommodates strain across a wide zone that extends well outside of the swath defined by the White Mountains and Fish Lake Valley faults. I hypothesize that strain is accommodated to the east of Fish Lake Valley fault in the SPLM and to the west of the White Mountains fault in Owens Valley, the Volcanic Tableland, and the Sierra Nevada frontal faults.

CHAPTER 6

FUTURE WORK

Based on the results of my research, I propose several avenues for future work. First, measurement of the present day deformation field could be improved. The campaign monuments in the GPS network we have established should be resurvey periodically in the future. Extending the time series that we developed from these stations will reduce uncertainties in velocity and provide a more accurate measure of crustal velocity. Several monuments in the network were surveyed as early as 1994, so they provide a valuable opportunity to create very long time series. Similarly, the new monuments that we installed in 2010, which have only been surveyed 3 times, will become important foundations when researchers survey this network in the future. In order to better resolve the extent and pattern of distributed deformation, I propose establishing a transect of closely spaced monuments across Owens Valley, from the interior of the White Mountains block to the interior of the Sierra Nevada. In addition to GPS geodesy, it would be worthwhile to explore the application of interferometric synthetic aperture radar (InSAR) to horizontal crustal deformation in the Walker Lane.

Second, more work could be done on the White Mountains fault zone. In particular, geologic field mapping could be extended eastward into foothills in order to constrain the offset of older (e.g. 1.2 Ma and 2.1 Ma) tephra layers. Documenting offset of these layers would provide constraints on slip rates at an older time scale. Slip rates during the ~2 Ma time scale are not well characterized, but are important for understanding the early phase of right-lateral slip on the WMFZ. I also propose more

geochronologic work on the WMFZ. Our ^{10}Be depth profile samples showed significant disturbance in the upper ~75 cm of the fan surfaces, which made age modeling difficult. Different geochronologic methods, such as U-Th dating of pedogenic carbonate or optically stimulated luminescence dating, would improve the ages of alluvial fans in Owens Valley. These methods have the advantage of being unaffected by inheritance, which we showed to be a significant issue in Owens Valley.

Third, extension rates on the other faults in the SPLM (e.g. the Emigrant Peak and Clayton Valley faults) need to be quantified over the same range of time scales as the Lone Mountain fault. In order to test the hypothesis that slip is accelerating across the SPLM, it is critical to have slip rate estimates over a wide range of time scales. The Holocene extension rate on the Clayton Valley fault is not known. The extension rates on the Emigrant Peak fault have been estimated broadly, but they could be improved with cosmogenic, OSL, or U-Th dating techniques.

Fourth, it is important to identify and quantify slip rates on faults that might be routing strain to or around the Mina deflection. I hypothesized that strain may be accommodated east of the Fish Lake Valley fault from the SPLM to the Bettles Well and Petrified Springs faults, and to the west of the White Mountains fault in the Volcanic Tableland and on the Sierra Nevada frontal fault. These faults not only represent a much wider zone of deformation than the faults bounding the White Mountains, but also provide potential routes for strain to transfer from the southern Walker Lane to the central Walker Lane.

APPENDIX A

WHITE MOUNTAIN FAULT ZONE TERRESTRIAL LIDAR

In this appendix, I document supplemental terrestrial LiDAR data collected along the White Mountains fault zone at the Estates site. These data were collected with a tripod-mounted Reigl VZ-400 scanner between 01 July and 08 July, 2012. The data set consists of 13 scans tied together with 24 unique reflector tie points. The resulting point cloud covers ~560,000 km^2. These data were not used in the final mapping and channel offset measurements used in this dissertation, however because they were collected at the same time as the airborne LiDAR data they present a unique opportunity to compare airborne and terrestrial data. I plan on pursuing this work in the future.

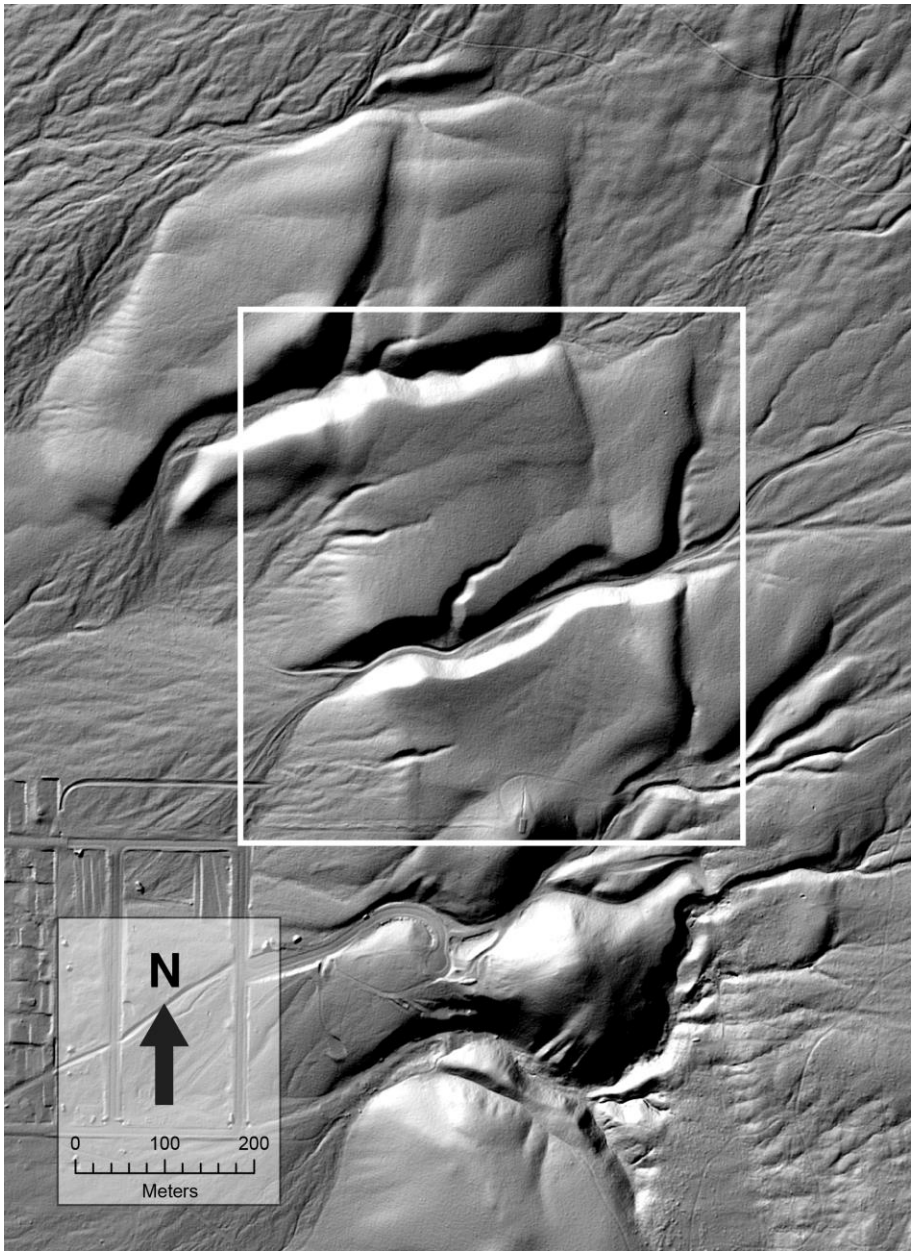

Figure A1.1. Hillshade map of the Estates site showing approximate extent (white rectangle) of the terrestrial LiDAR coverage.

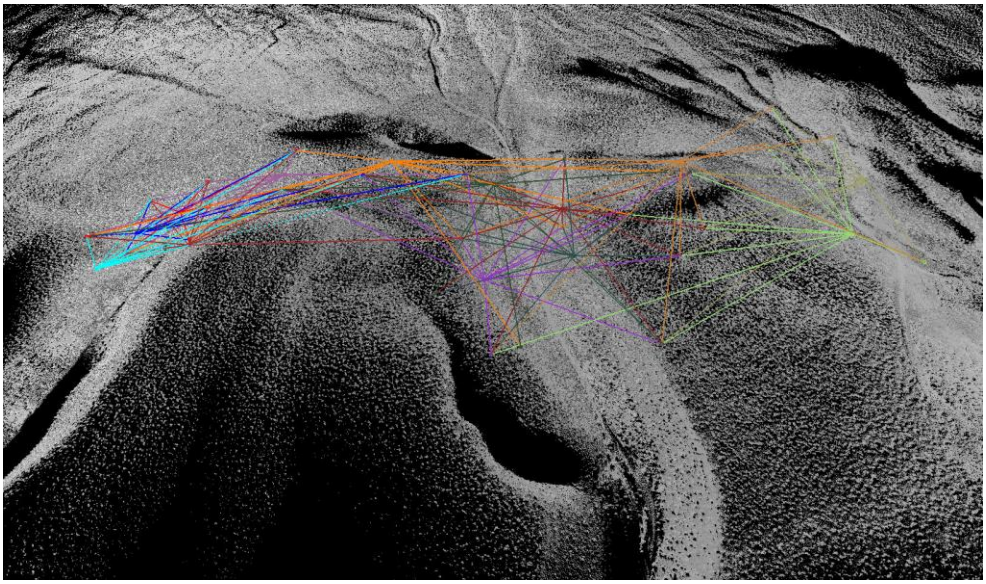

Figure A1.2. Oblique eastward view of part of the White Mountain fault zone terrestrial LiDAR point cloud. Individual points are colored by return intensity. Colored lines represent line-of-sight view from the scanner to reflectors.

REFERENCES

Anderson, R.S., Repka, J.L., and Dick, G.S., 1996, Explicit treatment of inheritance in dating depositional surfaces using in situ ^{10}Be and ^{26}Al: Geology, v. 24, p. 47–51.

Argus, D. F., R. G. Gordon, M. B. Heflin, C. Ma, R. J. Eanes, P. Willis, W. R. Peltier, and S. E Owen. (2010). The angular velocities of the plates and the velocity of Earth's centre from space geodesy. Geophysical Journal International, 180(3), 913–960. doi:10.1111/j.1365-246X.2009.04463.x.

Balco, G., Stone, J.O., Lifton, N.A., and Dunai, T.J., 2008, A complete and easily accessible means of calculating surface exposure ages or erosion rates from ^{10}Be and ^{26}Al measurements: Quaternary Geochronology, v. 3, p. 174–195, doi: 10.1016/j.quageo.2007.12.001.

Bateman, P.C., 1965, Geology and tungsten mineralization of the Bishop district, California: U.S. Geological Survey Professional Paper 470, 208 p.

Bennett, R., B. Wernicke, N. Niemi, A. Friedrich, and J. Davis, 2003, Contemporary strain rates in the northern Basin and Range province from GPS data, Tectonics, 22(2), 1008, doi:10.1029/2001TC001355.

Berry, M.E., 1997, Geomorphic analysis of late Quaternary faulting on Hilton Creek, Round Valley and Coyote warp faults, east-central Sierra Nevada, California, USA: Geomorphology, v. 20, p. 177–195.

Bull, W.B., 1991, Geomorphic responses to climatic change: New York, NY (United States); Oxford University Press, New York.

Cowgill, E., Gold, R.D., Xuanhua, C., Xiao-Feng, W., Arrowsmith, J.R., and Southon, J., 2009, Low Quaternary slip rate reconciles geodetic and geologic rates along the Altyn Tagh fault, northwestern Tibet: Geology, v. 37, p. 647–650, doi: 10.1130/G25623A.1.

Crone, A.J., and Machette, M.N., 1984, Surface faulting accompanying the Borah Peak earthquake, central Idaho: Geology, v. 12, p. 664, doi: 10.1130/0091-7613(1984)12<664:SFATBP>2.0.CO;2.

Crowder, D.F., McKee, E.H., Ross, D.C., and Krauskopf, K.B., 1973, Granitic rocks of the White Mountains area, California–Nevada: Age and regional significance: Geological Society of America Bulletin, v. 84, p. 285–296.

DeMets, C., R. G. Gordon, and D. F. Argus, 2010, Geologically current plate motions, Geophysical Journal International, 181(1), 1–80, doi:10.1111/j.1365-246X.2009.04491.x.

dePolo, C.M., 1989, Seismotectonics of the White Mountains fault system, east-central California and west- central Nevada [M.S. thesis]: Reno, University of Nevada, 354 p.

dePolo, C.M., and Ramelli, A.R., 1987, Preliminary report on surface fractures along the White Mountains fault zone associated with the July 1986 Chalfant Valley earthquake sequence: Bulletin of the Seismological Society of America, v. 77, p. 290–296.

dePolo, C.M., Clark, D.G., Slemmons, D.B., and Ramelli, A.R., 1991, Historical surface faulting in the Basin and Range province, western North America: implications for fault segmentation: Journal of Structural Geology, v. 13, p. 123–136.

Dixon, T.H., Robaudo, S., Lee, J., and Reheis, M.C., 1995, Constraints on present-day Basin and Range deformation from space geodesy: Tectonics, v. 14, p. 755–772.

Dixon, T.H., Miller, M., Farina, F., Wang, H., and Johnson, D., 2000, Present-day motion of the Sierra Nevada block and some tectonic implications for the Basin and Range province, North America: Tectonics, v. 19, p. 1–24.

Dixon, T.H., Norabuena, E., and Hotaling, L., 2003, Paleoseismology and Global Positioning System: Earthquake-cycle effects and geodetic versus geologic fault slip rates in the eastern California shear zone: Geology, v. 31, p. 55–58.

Dokka, R. K., and C. J. Travis, 1990, Late Cenozoic strike-slip faulting in the Mojave Desert, California, Tectonics, 9(2), 311–340.

Dolan, J.F., Bowman, D.D., and Sammis, C.G., 2007, Long-range and long-term fault interactions in Southern California: Geology, v. 35, p. 855, doi: 10.1130/G23789A.1.

Foy, T.A., Frankel, K.L., Lifton, Z.M., Johnson, C.W., and Caffee, M.W., 2012, Distributed extensional deformation in a zone of right-lateral shear: Implications for geodetic versus geologic rates of deformation in the eastern California shear zone-Walker Lane: Tectonics, v. 31, p. TC4008, doi: 10.1029/2011TC002930.

Frankel, K.L., Brantley, K.S., Dolan, J.F., Finkel, R.C., Klinger, R.E., Knott, J.R., Machette, M.N., Owen, L.A., Phillips, F.M., Slate, J.L., and Wernicke, B.P., 2007a, Cosmogenic ^{10}Be and ^{36}Cl geochronology of offset alluvial fans along the northern Death Valley fault zone: Implications for transient strain in the eastern California shear zone: Journal of Geophysical Research, v. 112, doi: 10.1029/2006JB004350.

Frankel, K.L., Dolan, J.F., Finkel, R.C., Owen, L.A., and Hoeft, J.S., 2007b, Spatial variations in slip rate along the Death Valley-Fish Lake Valley fault system determined from LiDAR topographic data and cosmogenic ^{10}Be geochronology: Geophysical Research Letters, v. 34, doi: 10.1029/2007GL030549.

Frankel, K.L., Dolan, J.F., Owen, L.A., Ganev, P., and Finkel, R.C., 2011, Spatial and temporal constancy of seismic strain release along an evolving segment of the Pacific–North America plate boundary: Earth and Planetary Science Letters, v. 304, p. 565–576, doi: 10.1016/j.epsl.2011.02.034.

Gan, W., Svarc, J., Savage, J., and Prescott, W., 2000, Strain accumulation across the Eastern California Shear Zone at latitude 36°30'N: Journal of Geophysical Research, v. 105, p. 16.

Ganev, P.N., Dolan, J.F., Frankel, K.L., and Finkel, R.C., 2010, Rates of extension along the Fish Lake Valley fault and transtensional deformation in the Eastern California shear zone–Walker Lane belt: Lithosphere, v. 2, p. 33–49, doi: 10.1130/L51.1.

Gold, R.D., and Cowgill, E., 2011, Deriving fault-slip histories to test for secular variation in slip, with examples from the Kunlun and Awatere faults: Earth and Planetary Science Letters, v. 301, p. 52–64, doi: 10.1016/j.epsl.2010.10.011.

Gosse, J.C., and Phillips, F.M., 2001, Terrestrial in situ cosmogenic nuclides: theory and application: Quaternary Science Reviews, v. 20, p. 1475–1560.

Hammond, W.C., and Thatcher, W., 2007, Crustal deformation across the Sierra Nevada, northern Walker Lane, Basin and Range transition, western United States

measured with GPS, 2000–2004: Journal of Geophysical Research, v. 112, doi: 10.1029/2006JB004625.

Hammond, W.C., Kreemer, C., and Blewitt, G., 2009, Geodetic constraints on contemporary deformation in the northern Walker Lane: 3. Central Nevada seismic belt postseismic relaxation: Late Cenozoic Structure and Evolution of the Great Basin–Sierra Nevada Transition: Geological Society of America Special Paper, v. 447, p. 33–54, doi: 10.1130/2009.2447(03).

Hanson, R.B., Saleeby, J.B., and Fates, D.G., 1987, Age and tectonic setting of Mesozoic metavolcanic and metasedimentary rocks, northern White Mountains, California: Geology, v. 15, p. 1074–1078.

Hearn, E. H., and E. D. Humphreys, 1998, Kinematics of the southern Walker Lane Belt and motion of the Sierra Nevada block, California. Journal of Geophysical Research, 103(B11), 27033–27049.

Hidy, A.J., Gosse, J.C., Pederson, J.L., Mattern, J.P., and Finkel, R.C., 2010, A geologically constrained Monte Carlo approach to modeling exposure ages from profiles of cosmogenic nuclides: An example from Lees Ferry, Arizona: Geochemistry Geophysics Geosystems, v. 11, doi: 10.1029/2010GC003084.

Hoeft, J.S., 2010, Temporal variations in slip-rate along the Lone Mountain fault, western Nevada [M.S. thesis]: Atlanta, Georgia Institute of Technology, 102 p.

Hoeft, J.S., and Frankel, K.L., 2010, Temporal variations in extension rate on the Lone Mountain fault and strain distribution in the eastern California shear zone-Walker Lane: Geosphere, v. 6, p. 917–936, doi: 10.1130/GES00603.S2.

Hoeft, J.S., and Frankel, K.L., 2012, Preliminary surficial geologic map along the northwest Lone Mountain and Weepah Hills piedmonts, Esmeralda county, Nevada: Nevada Bureau of Mines and Geology Open-File Report, Reno, Nevada.

Kirby, E., Burbank, D.W., Reheis, M., and Phillips, F., 2006, Temporal variations in slip rate of the White Mountain Fault Zone, Eastern California: Earth and Planetary Science Letters, v. 248, p. 168–185, doi: 10.1016/j.epsl.2006.05.026.

Kirby, E., Anandakrishnan, S., Phillips, F., and Marrero, S., 2008, Late Pleistocene slip rate along the Owens Valley fault, eastern California: Geophysical Research Letters, v. 35, p. L01304, doi: 10.1029/http://dx.doi.org/10.1029.

Kohl, C.P., and Nishiizumi, K., 1992, Chemical isolation of quartz for measurement of in-situ-produced cosmogenic nuclides: Geochimica et Cosmochimica Acta, v. 56, p. 3583–3587.

Krauskopf, K.B., 1971, Geologic map of the Mount Bar- croft Quadrangle, California-Nevada: U.S. Geological Survey Geologic Quadrangle Map GQ-960, scale 1: 62,500.

Lal, D., 1991, Cosmic ray labeling of erosion surfaces: in situ nuclide production rates and erosion models: Earth and Planetary Science Letters, v. 104, p. 424–439.

Le, K., Lee, J., Owen, L.A., and Finkel, R., 2007, Late Quaternary slip rates along the Sierra Nevada frontal fault zone, California: Slip partitioning across the western margin of the Eastern California Shear Zone-Basin and Range Province: Geological Society of America Bulletin, v. 119, p. 240–256, doi: 10.1130/B25960.1.

Lee, J., Spencer, J., and Owen, L., 2001a, Holocene slip rates along the Owens Valley fault, California: Implications for the recent evolution of the Eastern California Shear Zone: Geology, v. 29, p. 819.

Lee, J., Rubin, C.M., and Calvert, A., 2001b, Quaternary faulting history along the Deep Springs fault, California: Geological Society of America Bulletin, v. 113, p. 855–869.

Lee, J., Stockli, D., Schroeder, J., Tincher, C., Bradley, D., Owen, L., Gosse, J., Finkel, R., and Garwood, J., 2006, Fault slip transfer in the Eastern California Shear Zone–Walker Lane Belt: Geological Society of America Penrose Conference Field Trip Guide (Kinematics and Geodynamics of Intraplate Dextral Shear in Eastern California and Western Nevada, Mammoth Lakes, California, 21–26 April 2005), 26 p., doi: 10.1130/2006.FSTITE.PFG.

Lee, J., Garwood, J., Stockli, D.F., and Gosse, J., 2009a, Quaternary faulting in Queen Valley, California-Nevada: Implications for kinematics of fault-slip transfer in the eastern California shear zone-Walker Lane belt: Geological Society of America Bulletin, v. 121, p. 599–614, doi: 10.1130/B26352.1.

Lee, J., Stockli, D.F., Owen, L.A., Finkel, R.C., and Kislitsyn, R., 2009b, Exhumation of the Inyo Mountains, California: Implications for the timing of extension along the western boundary of the Basin and Range Province and distribution of dextral

fault slip rates across the eastern California shear zone: Tectonics, v. 28, doi: 10.1029/2008TC002295.

Lienkaemper, J.J., Pezzopane, S.K., Clark, M.M., and Rymer, M.J., 1987, Fault fractures formed in association with the 1986 Chalfant Valley, California, earthquake sequence: preliminary report: Bull. Seism. Soc. Am, v. 77, p. 297–305.

Lifton, Z.M., Newman, A.V., Frankel, K.L., Johnson, C.W., and Dixon, T.H., 2013, Insights into distributed plate rates across the Walker Lane from GPS Geodesy: Geophysical Research Letters, 40(17), 4620-4624, doi: 10.1002/grl.50804.

Lifton, Z.M., Lee, J., Frankel, K.L., Newman, A.V., Schroeder, J.M., Heizler, M.T., in preparation, Quaternary slip rates on the White Mountains Fault Zone, Eastern California: Implications for comparing geologic to geodetic slip rates across the Walker Lane: Geological Society of America Bulletin.

Lifton, Z.M., Newman, A.V., Frankel, K.L., in preparation, Latest Pleistocene and Holocene slip rates on the Lone Mountain fault: evidence for accelerating extension in the Silver Peak-Lone Mountain extensional complex: Lithosphere.

McCaffrey, R., 2005, Block kinematics of the Pacific–North America plate boundary in the southwestern United States from inversion of GPS, seismological, and geologic data. Journal of Geophysical Research, 110(B7). doi:10.1029/2004JB003307

McKee, E.H., Diggles, M.F., Donahoe, J.L., and Elliot, G.S., 1982, Geologic map of the White Mountains Wilderness and Roadless Areas, California, and Nevada: U.S. Geological Survey Miscellaneous Field Studies Map MF-1361-A, scale 1:62,500.

Nagorsen-Rinke, S., Lee, J., and Calvert, A., 2013, Pliocene sinistral slip across the Adobe Hills, eastern California–western Nevada: Kinematics of fault slip transfer across the Mina deflection: Geosphere, v. 9, p. 37–53, doi: 10.1130/GES00825.S3.

Nishiizumi, K., Imamura, M., Caffee, M.W., Southon, J.R., Finkel, R.C., and McAninch, J., 2007, Absolute calibration of ^{10}Be AMS standards: Nuclear Instruments and Methods in Physics Research Section B: Beam Interactions with Materials and Atoms, v. 258, p. 403–413, doi: 10.1016/j.nimb.2007.01.297.

Oldow, J.S., Elias, E.A., Ferranti, L., McClelland, W.C., and McIntosh, W.C., 2009, Late Miocene to Pliocene synextensional deposition in fault-bounded basins within the upper plate of the western Silver Peak–Lone Mountain extensional complex, west-central Nevada: Late Cenozoic Structure and Evolution of the Great Basin–Sierra Nevada Transition: Geological Society of America Special Paper, v. 447, p. 275–312, doi: 10.1130/2009.2447(14).

Oldow, J.S., Geissman, J.W., and Stockli, D.F., 2008, Evolution and Strain Reorganization within Late Neogene Structural Stepovers Linking the Central Walker Lane and Northern Eastern California Shear Zone, Western Great Basin: International Geology Review, v. 50, p. 270–290, doi: 10.2747/0020-6814.50.3.270.

Oldow, J.S., Kohler, G., and Donelick, R.A., 1994, Late Cenozoic extensional transfer in the Walker Lane strike-slip belt, Nevada: Geology, v. 22, p. 637, doi: 10.1130/0091-7613(1994)022<0637:LCETIT>2.3.CO;2.

Oskin, M., Perg, L., Shelef, E., Strane, M., Gurney, E., Singer, B., and Zhang, X., 2008, Elevated shear zone loading rate during an earthquake cluster in eastern California: Geology, v. 36, p. 507, doi: 10.1130/G24814A.1.

Phillips, F.M., and Majkowski, L., 2011, The role of low-angle normal faulting in active tectonics of the northern Owens Valley, California: Lithosphere, v. 3, p. 22–36, doi: 10.1130/L73.1.

Reheis, M.C., and Dixon, T.H., 1996, Kinematics of the Eastern California shear zone: Evidence for slip transfer from Owens and Saline Valley fault zones to Fish Lake Valley fault zone: Geology, v. 24, p. 339.

Reheis, M.C., and Sawyer, T.L., 1997, Late Cenozoic history and slip rates of the Fish Lake Valley, Emigrant Peak, and Deep Springs fault zones, Nevada and California: Geological Society of America Bulletin, v. 109, p. 280–299, doi: 10.1130/0016-7606(1997)109<0280:LCHASR>2.3.CO;2.

Reheis, M.C., Sawyer, T.L., Slate, J.L., Gillispie, A.R., 1993. Geologic map of late Cenozoic deposits and faults in the southern part of the Davis Mountain 15′ quadrangle, Esmeralda County, Nevada. U.S. Geol. Surv. Map I-2342. scale 1:24,000.

Sarna-Wojcicki, A.M., Pringle, M.S., Jr., and Wijbrans, J., 2000, New $^{40}Ar/^{39}Ar$ age of the Bishop tuff from multiple sites and sediment rate calibration for the

Matuyama-Brunhes boundary: Journal Geophysical Research, v. 105, p. 21431-21443.

Savage, J. C., and M. Lisowski, 1998, Viscoeleastic coupling model of the San Andreas Fault along the big bend, southern California, J. Geophys. Res., 103(B4), 7281–7292.

Savage, J. C., and R. O. Burford, 1973, Geodetic determination of relative plate motion in central California. J. Geophys. Res., 78(5), 832–845.

Schroeder, J., 2003, Pleistocene dextral fault slip along the White Mountains fault zone, California [M.S. thesis]: Ellensburg, Central Washington University, 62 p.

Schwartz, D.P., and Coppersmith, K.J., 1984, Fault behavior and characteristic earthquakes: Examples from the Wasatch and San Andreas fault zones: Journal of Geophysical Research: Solid Earth (1978–2012), v. 89, p. 5681–5698.

Sheehan, T.P., 2007, Evolution of Neogene fault populations in northern Owens Valley, California and implications for the Eastern California shear zone [Ph.D. thesis]: New Orleans, Louisiana, Tulane University, 203 p.

Smith, K.D., and Priestley, K.F., 2000, Faulting in the 1986 Chalfant, California, sequence: Local tectonics and earthquake source parameters: Bulletin of the Seismological Society of America, v. 90, p. 813–831.

Stockli, D.F., Dumitru, T.A., McWilliams, M.O., and Farley, K.A., 2003, Cenozoic tectonic evolution of the White Mountains, California and Nevada: Geological Society of America Bulletin, v. 115, p. 788–816, doi: 10.1130/0016-7606(2003)115<0788:CTEOTW>2.0.CO;2.

Stone, J.O., 2000, Air pressure and cosmogenic isotope production: Journal of Geophysical Research, v. 105, p. 23753–23–759.

Thatcher, W., 2009, How the Continents Deform: The Evidence From Tectonic Geodesy: Annual Review of Earth and Planetary Sciences, v. 37, p. 237–262, doi: 10.1146/annurev.earth.031208.100035.

Wallace, R.E., 1987, Grouping and migration of surface faulting and variations in slip rates on faults in the Great Basin province: Bulletin of the Seismological Society of America, v. 77, p. 868–876.

Wells, D.L., and Coppersmith, K.J., 1994, New empirical relationships among magnitude, rupture length, rupture width, rupture area, and surface displacement: Bulletin of the Seismological Society of America, v. 84, p. 974–1002.

Wesnousky, S.G., 2005a, Active faulting in the Walker Lane: Tectonics, v. 24, doi: 10.1029/2004TC001645.

Wesnousky, S.G., 2005b, The San Andreas and Walker Lane fault systems, western North America: transpression, transtension, cumulative slip and the structural evolution of a major transform plate boundary: Journal of Structural Geology, v. 27, p. 1505–1512, doi: 10.1016/j.jsg.2005.01.015.

Wesnousky, S.G., Bormann, J.M., Kreemer, C., Hammond, W.C., and Brune, J.N., 2012, Neotectonics, geodesy, and seismic hazard in the Northern Walker Lane of Western North America: Thirty kilometers of crustal shear and no strike-slip?: Earth and Planetary Science Letters, v. 329, p. 133–140, doi: 10.1016/j.epsl.2012.02.018.

Zechar, J.D., and Frankel, K.L., 2009, Incorporating and reporting uncertainties in fault slip rates: Journal of Geophysical Research, v. 114, doi: 10.1029/2009JB006325.

Zehfuss, P.H., Bierman, P.R., Gillespie, A.R., Burke, R.M., and Caffee, M.W., 2001, Slip rates on the Fish Springs fault, Owens Valley, California, deduced from cosmogenic ^{10}Be and ^{26}Al and soil development on fan surfaces: Geological Society of America Bulletin, v. 113, p. 241–255, doi: 10.1130/0016-7606(2001)113<0241:SROTFS>2.0.CO;2.

Zielke, O., and Arrowsmith, J.R., 2012, LaDiCaoz and LiDARimager—MATLAB GUIs for LiDAR data handling and lateral displacement measurement: Geosphere, v. 8, p. 206–221, doi: 10.1130/GES00686.S1.

Zumberge, J., Heflin, M., Jefferson, D., Watkins, M., & Webb, F., 1997, Precise point positioning for the efficient and robust analysis of GPS data from large networks. Journal of Geophysical Research, 102, 5005–5018.